

SIMULATION OF YTTERBIUM DOPED FIBER AMPLIFICATION

by

JONATHAN WAISMAN, B.A.Sc.

A thesis

Submitted to the School of Graduate Studies

in Partial Fulfillment of the Requirements

for the Degree

Master of Applied Science

McMaster University

©Copyright by Jonathan Waisman, September 2007

MASTER OF APPLIED SCIENCE (2007)
(Engineering Physics)

McMaster University
Hamilton, Ontario

TITLE: Simulation of ytterbium doped fiber amplification
AUTHOR: Jonathan Waisman, BSc. (University of Toronto)
SUPERVISOR: Dr. Harold K. Haugen

ABSTRACT

This report summarizes in detail a software tool that has been developed and for modeling doped fiber amplification accounting for gain, amplified spontaneous emission, group velocity dispersion and self-phase modulation. The innovative algorithms perform calculations for these active and passive effects simultaneously and this accounts for the complex-valued electric field of chirped picosecond pulses.

A comprehensive verification procedure is carried out for a selection of doped double-clad fiber amplifiers with Ytterbium and Thulium as the selected fiber core dopants under operating conditions and geometries defined in the journal articles being verified. These tests consider both continuous wave, nanosecond and picosecond pulsed amplification.

Numerical modeling results are presented for a Ytterbium-doped double-clad fiber amplifier (YDFA) component in our hybrid master oscillator power amplifier (MOPA) system. Initial conditions include 7.7 ps pulses at a repetition-rate of 577 MHz and at a peak wavelength of 1075 nm and input linear and nonlinear chirps.

ACKNOWLEDGMENTS

I would like to express how grateful I am to so many who have contributed so much to my research and development over that past couple of years. My experience has been most rewarding from the very first day shaking the hand of my supervisor Prof. Dr. Harold Haugen. He brought me into the wonderful world of optical physics, and I will always be thankful for this. His attention to detail, as well as his stimulating intuition has been a monumental help in my work.

Some things one can not learn from a book. Luckily, I had someone like Andrew Budz, whose vast understanding of photonics has helped me solve my theoretical problems along the way. I could not have asked for a better colleague and friend. Also, I would like to thank Dr. Henry Tiedje, Travis Crawford and Eugene Hsu for their valuable hints during my experiments and for their helpful comments on my simulator and presentations. I would like to express my gratitude to Dr. Marc Eichhorn who's key guidance in my initial algorithm development helped me bridge the gap in understanding state of the art simulation of specialty fibers. Also I'd like to thank Bertrand Morasse for his multiple contributions including cw simulation results used in benchmarking of my work and Bernhard Bayer for his user interface software development.

Thank you to my mother, father, and siblings for your love and support. Also I'd like to thank my father for his push on my childhood mathematical development and in general his attention to my academic interests. I'd also like to thank Gregory Kvint for our interesting conversations on cosmology, extraterrestrials and the sort during my childhood. This I feel sparked much of my scientific imagination in the years to come.

Finally, I would like to thank someone very special in my life, my dear wife Yana. She has always supported me in all my endeavors. Without her, I wouldn't be where I am today.

TABLE OF CONTENTS

ABSTRACT	iii
ACKNOWLEDGMENTS	iv
LIST OF TABLES	ix
LIST OF FIGURES	x
1 Introduction	1
1.1 Optical Fiber Amplifiers.....	2
1.2 Master Oscillator Power Amplifier Systems	3
1.3 Experimental Setup.....	5
1.4 Numerical Modeling Overview	7
2 Optical Fibers	11
2.1 Non-Linear Schrödinger Equation.....	11
2.1.1 The Retarded Reference Frame.....	12
2.1.2 Amplitude Normalization	13
2.2 Step-Index Fibers.....	15
2.2.1 Mode-Field Distributions.....	16
2.2.2 Input Pulse Distributions.....	17
2.2.3 Numerical Aperture	20
2.3 Chromatic Dispersion	20
2.3.1 Group Velocity Dispersion	22
2.4 Self Phase Modulation.....	23

2.5	Polishing Angle and Fresnel Loss	26
2.6	Split-Step Fourier Method	27
3	Optical Amplification in Doped Fibers	33
3.1	Double-Clad Fiber Amplifiers	33
3.1.1	Overlap Function	35
3.1.2	Propagation Geometries.....	38
3.2	Stimulated Emission and Absorption	39
3.3	Rare-Earth Dopants and Their Lifetimes.....	39
3.3.1	Radiative Lifetimes	40
3.3.2	Non-Radiative Lifetimes.....	41
3.3.3	Excited State Absorption	41
3.3.4	Cross-Relaxation Tensors	42
3.3.5	Thulium Manifold.....	43
3.3.6	Ytterbium Manifold	45
3.4	Amplified Spontaneous Emission.....	46
3.5	Absorption and Emission Cross-Sections.....	48
3.6	Rate Equations	49
3.7	Parabolic Pulse Amplification	52
3.8	Standard Pulsed Simulation Algorithm	53
4	Simulator Innovation.....	57
4.1	Passive Transform Block.....	58
4.2	Transforming Pulse Power to Complex Amplitude.....	59
4.3	Inside the Black Box.....	62
5	Theoretical Unknowns and Limitations.....	67
5.1	Input Chirp.....	67

5.2	Pulse Shape.....	69
5.3	High Frequency Errors.....	69
5.4	Unsaturation Pump Absorption.....	71
5.5	Pump Spectrum.....	73
5.6	Wavelength Bin Resolution.....	74
5.7	Non-uniform Spatial Resolution in the SSFM.....	76
5.8	Round off Errors.....	77
5.9	Higher Order Dispersion.....	78
5.10	Stimulated Raman Scattering.....	79
5.11	Stimulated Brillouin Scattering.....	81
5.12	Polarization Effects.....	81
5.13	Numerical Inaccuracies of the SPM Model.....	82
5.14	Amplified Spontaneous Emission Equation.....	83
6	Results and Verification.....	85
6.1	GVD and Input Chirp Verification.....	86
6.2	SPM and Input Chirp Verification.....	89
6.3	GVD and SPM Verification.....	94
6.4	Gain and ASE Simulation Results and Verification.....	96
6.4.1	MCP Output Data Types.....	97
6.4.2	CW Results.....	97
6.4.3	Pulsed Simulation Results.....	113
6.5	Verification of Power to Amplitude Algorithm.....	127
6.6	Pulsed Simulation Results Accounting gain, ASE, GVD and SPM.....	130
6.6.1	Active Simulations on SHARCNET.....	131
6.6.2	Active and Passive Simulation of Unchirped Input Gaussian Pulses.....	134

6.6.3	Active and Passive Simulation of Chirped Input Gaussian Pulses	137
7	Future Work.....	145
	References.....	147
Appendix A.	Calculation of FWHM and RMS.....	157
Appendix B.	SSFM Dispersion Operator.....	161
Appendix C.	Generalized Overlap Functions	163
Appendix D.	Simulation Input Tables.....	171

LIST OF TABLES

Table 2-1	Properties of Gaussian and sech^2 functions commonly used as input pulse power distributions in simulation runs. FWHM is the full-width at half maximum pulse peak power, and RMS is the root-mean-square.....	19
Table 5-1	Parameters for lifetime quenching of ytterbium [22]......	72
Table 6-1	RMS widths for an SPM-only MCP simulation compared to analytical results from Equation 6-6. Results are in good agreement.....	91
Table 6-2	Parameters used for comparison of the MCP and Morasse's simulators operating in the cw regime. No Fresnel's losses have been taken into account here, as they have also been set to zero by Morasse in his simulation.	107
Table 6-3	Parameters used for comparison of the MCP and Eichhorn's pulsed simulations in modeling pulsed operation of Tm:ZBLAN double clad fiber amplifiers with a D-shaped inner cladding. Note that the signal overlap function Γ_j from Equation 3-6 is generated dynamically on software initialization. Radiative and non-radiative time-constants are provided in Chapter 3.....	114
Table 6-4	Parameters used for MCP pulsed simulation 20 kHz rep-rate for a co-propagating geometry. The signal overlap functions Γ_j from Equation 3-6 are generated on software initialization.	117
Table 6-5	Parameters used for the MCP simulator in modeling 10 kHz repetition rate pulsed operation in the co-propagating geometry.....	123
Table 6-6	Parameters used for the MCP simulator in modeling 577 MHz pulsed operation in the counter-propagating geometry.....	132

LIST OF FIGURES

<p>Figure 1-1 Laboratory experimental setup based on work done by Andrew Budz [56]. Achromatic lenses are used to focus and collimate multiple wavelengths of 1040 nm and 1080 nm into and out of the YDFA. Grating orientation can be designed using the diffraction grating equation [82].</p>	6
<p>Figure 2-1 The cross-sectional material distribution of a typical step index fiber. The inner core has refractive index n_{co} which is greater than the cladding index n_{cl}. The outer surface is called the jacket and usually has an index of refraction less than the cladding. Also, this fiber is axisymmetric since the refractive index is constant for any $r = \sqrt{x^2 + y^2}$</p>	16
<p>Figure 2-2 Autocorrelation trace of a pulse generated from a mode-locked diode laser taken from a) [9] and b) [14].....</p>	18
<p>Figure 2-3 Red shift of an a) asymmetric Gaussian pulse (envelope) traveling through a nonlinear medium whose b) instantaneous frequency gets chirped due to SPM. Results for the regular Gaussian pulse are plotted in c) and d) respectively. Variation of instantaneous frequency is proportional to the time rate of change of the pulse intensity. This can be observed in the contrast of the two bottom plots.....</p>	25
<p>Figure 2-4 The SSFM breaks the fiber (outer solid rectangle) into N steps (inner solid rectangles) with each step calculating one operation of SPM (at the dashed lines) in between two operations of GVD. The gain variable $g = g(z, \tau)$ is discussed in the following chapters.....</p>	29
<p>Figure 3-1 The double-clad cross-sectional geometry for the a) hexagonal and b) D-shaped fibers used in the simulations of Chapter 6.....</p>	34
<p>Figure 3-2 Three possible pumping operating geometries for a ytterbium-doped double-clad fiber amplifier. The positive convention is from left to right as indicated by the bottom arrow in the figure.</p>	38
<p>Figure 3-3 Three level laser scheme used for modeling a Tm:ZBLAN fiber amplifier. All numbers without units are in milliseconds. Data is taken from references [8] and [40]. Nonzero tensor values are $k_{3011}=7.86 \times 10^{-24} \text{ m}^3/\text{s}$ and $k_{1130}=6.00 \times 10^{-25} \text{ m}^3/\text{s}$.</p>	44

Figure 3-4 YDFA laser scheme with radiative and quenching relaxation process. The quenching relaxation time is under $5 \mu\text{s}$ according to article [45] and the value of $1 \mu\text{s}$ is taken from Yelen's article [22].45

Figure 3-5 Thulium absorption cross-section (solid line) for the signal $^3\text{H}_6 \rightarrow ^3\text{F}_4$ is adapted from Eichhorn's article [8]. Thulium emission cross-section (dashed line) for the signal $^3\text{F}_4 \rightarrow ^3\text{H}_6$ is adapted from Walsh's article [40].48

Figure 3-6 Ytterbium absorption (solid line) and emission (dashed line) cross-sections ($^2\text{F}_{5/2} \leftrightarrow ^2\text{F}_{7/2}$) for the YDFA implemented in the ultra-fast laser lab. The data used to plot this figure is provided by CorActive Inc.49

Figure 4-1 The PT block is an algorithm used to propagate the phase of the signal along with the power, or in other words to keep track of the complex amplitude.58

Figure 4-2 The standard gain algorithm is used to calculate the current gain coefficient, a procedure performed once between PT block operations for every section and time step. This updates the gain coefficient array only for the current time step.62

Figure 4-3 The block diagram of the passive transform algorithm. First the gain is updated for the current time step t_0 , and the passive operations are performed using the GGS block (illustrated in Figure 4-4) using this information as well as the previous pulse characteristics for those time steps which have not yet been attained. The correction factor performed on the output power $1 - (0.5 \times dz \times g)^2$ is applied according to Equation 4-5 when dz is not assumed to be a very small step. 64

Figure 4-4 The GGS block performs the actual gain, GVD and SPM operations onto the pulse. The entire complex amplitude pulse and gain coefficient array are sent as input. The resultant amplitude is used as input for the next section of the fiber. ...65

Figure 5-1 The first row shows an example of normal pulse amplification (from left to right in a particular section) during simulation. The second row shows how an abnormal amplification event can result in an amplified pulse with a spike for the current time-step that adds high frequency components not natural to the pulse and cause aliasing if and when the pulse in subfigure (f) is passed into an FFT. The spike power bar in (f) shows how qualitatively, the amount of amplified power can cause aliasing.....70

Figure 5-2 Pump power spectrum implies simulation inaccuracy if the pump beam is taken to be monochromatic, as the superimposed absorption cross-section (dashed line) is not constant throughout the bandwidth of the pump spectrum.....73

Figure 5-3 Memory Consumption (left) in megabytes and Computation time (right) measured for identical pulsed simulations for a selected number of wavelength bins.....75

Figure 5-4	The output ASE spectrum for a selected number of bins. Reasonable convergence happens for bin numbers greater than 30 bins.	75
Figure 6-1	MCP simulation shows normalized pulse amplitude at $z=0, 2L_D$ and $4L_D$ meters down the fiber. The pulse-width increases with distance due to the GVD effects.	87
Figure 6-2	MCP simulation shows a Gaussian pulse broadening due to natural GVD effects over a distance for pulses with selected input chirps.	88
Figure 6-3	MCP simulation output for self-phase modulation with selected $\phi_{\max} =$ a) 0π b) 0.5π c) 1.0π d) 1.5π e) 2.5π and f) 3.5π respectively for a Gaussian input pulse and all other effects turned off.	90
Figure 6-4	MCP simulation results are for SPM-only calculations with selected chirped input pulses. Results are in excellent agreement to identical SSFM simulations by Agrawal [3].	91
Figure 6-5	A Gaussian pulse (left) defined for $N=2048$ data points at $PBC=2.5$ in the time domain, and the corresponding spectrum (right).	93
Figure 6-6	A Gaussian pulse (left) defined for $N=2048$ data points at $PBC=20.0$ in the time domain, and the corresponding spectrum (right).	94
Figure 6-7	Time-domain broadening of a Gaussian pulse in normal and anomalous dispersion regimes when $L_D=L_{NL}$ or equivalently, $N=1$. In the case $\beta_2 < 0$, the Gaussian pulse morphs into a soliton (sech^2) pulse. Also included for comparison is the simulation output with SPM turned off with $N=0$. σ_0 is the initial RMS half-width.	96
Figure 6-8	Output average powers for selected launched powers in the counter-propagating geometry. Experimental data (circles) are compared to simulation results (asterisks and triangles) at selected relaxation time constants.	99
Figure 6-9	Power distribution down a 14.8 m fiber for the signal and pump for a cw simulation of the ultra-fast laser laboratory experiment with input pump power 2.11 W in the counter-propagation geometry.	101
Figure 6-10	Magnified power distribution of forward and backward generated ASE from an MCP (cw) simulation.	101
Figure 6-11	Excited level concentration is highest at 9 m down the 14.8 m fiber. For the YDFA, there are two metastable energy levels that interact with the input powers with N_0 and N_1 representing the ground and excited state dopant energy population densities in $[\text{m}^{-3}]$ respectively.	103

Figure 6-12	Output power versus fiber cut where each unit of fiber length (1, 2 ... 10 m) corresponds to a simulation for that length. The solid lines correspond to the MCP simulation outputs and Morasse's cw simulation is indicated by dashed lines.....	108
Figure 6-13	Forward and backward ASE outputs from two simulators. Backward ASE is output at the left fiber facet ($z=0$). Each data point corresponds to the total power for all 21 wavelength bins evenly ranging from 1000 nm to 1100 nm.....	108
Figure 6-14	The distribution of power throughout a 10 m long fiber for the forward propagating signal and pump powers. The solid lines correspond to the MCP simulation outputs for identical operating conditions to that of Morasse's cw simulation indicated by dashed lines.	110
Figure 6-15	Power distribution throughout a 10 m long fiber for the forward and backward ASE powers. Each data point corresponds to a total averaged power for all 21 wavelength bins ranging from 1000 nm to 1100 nm.	110
Figure 6-16	Output ASE powers versus wavelength for each of the 21 wavelength bins that are distributed evenly from 1000 nm to 1100 nm. The backward ASE powers are taken from the left facet of the fiber (Figure 3-2).....	111
Figure 6-17	Total power distribution, generated within the fiber amplifier as a sum of signal, forward and backward ASE powers from Figures 6-14 and 6-15 throughout the fiber length. Also included is the limit for the total power which is equal to the total launched pump power of 4.0 W. The dashed curve shows the result for the condition $R_{10}=\alpha_s=\alpha_p=0$	112
Figure 6-18	Output power simulation results for a Thulium doped D-shaped inner-clad fiber amplifier for three different propagating geometries. The input pump power is 3 W. For the symmetric propagation scheme, 1.5 W is launched at both facets. At 1.5 m, ASE becomes the dominant energy extractor. These results are in excellent agreement to Eichhorn's simulation results [8].....	115
Figure 6-19	Pulsed simulation output signal peak power distributions for selected launched pump powers. Numerical analysis takes into account gain and ASE only. Also provided above each plot is the output average signal power.....	118
Figure 6-20	Pulsed simulation output average ASE power distributions for selected launched pump powers. The inset shows the same plot in logarithmic scale revealing the lowest power ASE generation at a 3W pump that is difficult to make out in the outer figure. Refer to the legend in Figure 6-19 for details on each line pattern.	118
Figure 6-21	Output instantaneous pulse powers for three selected pump powers. Peak powers correspond to those at 10 m in Figure 6-19. Asymmetric distributions are caused by gain saturation within the fiber amplifier.....	119

Figure 6-22	Absorption and emission cross-sections for a YDFA fabricated by CorActive Inc. Data points totaling 316 were provided by Morasse.....	120
Figure 6-23	Absorption and emission cross-sections for 30 wavelength bins used in an MCP simulation. One wavelength bin is centered at 1064.0 nm and the bins are bounded by 1000 nm and 1100 nm as requested in the requirements specification..	121
Figure 6-24	Steady-state MCP simulation results for a) the ratio of the excited to the total dopant energy population densities and b) the power distributions throughout the fiber. These results are based on operating conditions in Table 6-5 with zero input signals.	124
Figure 6-25	Output energies for the first 10 pulses. Convergence is clear after the second pulse propagates through the fiber.....	126
Figure 6-26	The pulse energy distribution of the output pulse after the simulation reaches convergence.	126
Figure 6-27	Error propagation occurs when an inaccurate output amplitude calculated from a previous fiber step is taken as the input amplitude to the next step. In the figure, δ_{error} is sent as components of two inputs to the next P2A block. Refer to Chapter 4 for details on the algorithm.	128
Figure 6-28	Input pulse power (solid line, left scale) and its nonlinear chirp (dashed line, right scale) used in the verification of the P2A algorithm.....	129
Figure 6-29	Output pulse power results for gain and ASE calculations comparing the MCP simulator where P2A is utilized to the standard power propagation algorithm (which does not use P2A).....	129
Figure 6-30	Peak powers for the first 260000 pulses of a gain and ASE (active) simulation run on SHARCNET for the operating conditions provided in Table 6-6. The 'S' curve indicates that the simulation is converging with peak powers approaching to about 325 W. This simulation took approximately 22 days to process on the SHARCNET supercomputer.....	133
Figure 6-31	Output power and normalized power spectrum for two different time (N & PBC) resolutions. The output power spectrum for N=512 is much more resolved than the one for N=2048. Simulation operating times were 18.5 minutes for N=2048 and 1.0 minute for N=512.....	135
Figure 6-32	Input seed spectra for an unchirped simulated pulse (dashed line) and the chirped measured pulse (solid line) by Andrew Budz.	138
Figure 6-33	Theoretical chirped input seed spectrum (dashed line) utilizing the chirp function from Equation 6-19 has the same approximate distribution as that measured by Andrew Budz (solid line) from experiment.....	139

Figure 6-35 Active and passive simulation of 10000 pulses after active-only simulation of 260000 pulses. The first data point is the last peak power from the previous 260000 pulses from an active-only simulation described in Section 6.6.1. These are output powers before Fresnel's losses are taken into account.144

COGNATE BOARD

1 Introduction

The optical signal is used in numerous state of the art applications that have touched many engineering endeavors in the last couple of decades. With all of these applications considered equal, there is one common trend in the research and development: To tailor the signal in space and time. To do so requires an understanding of the conduit in which the optical energy propagates and is amplified, as well as the optical-material interactions along the way. In addition, there are complex interactions of light with matter involving the phase of the light wave, and therefore, the complex amplitude is more valuable when used to represent the optical signal in the research instead of just its intensity.

The ultrashort optical pulse is of considerable interest in photonics. The term ultra-short usually refers to pulses that have picosecond (or smaller) widths. These pulses are used in a variety of applications such as information carriers in optical fibers in the telecommunications industry, for two-photon excitation and pump-probe experiments for characterizing material properties.

Often, it is necessary to amplify these pulses for experiments that involve the probing of materials or for any nonlinear interactions to be observed. One of the least expensive ways to do this is to optically amplify a pulse when it propagates through a pumped medium. A multi-layered optical fiber with an exotic element concentration (or

doping) within the core is called the fiber amplifier and is an example of such a system. When the dopants are excited by an external light source, they can amplify a propagating optical pulse. Gas or dye lasers can be used to achieve similar results, but with the overhead of less efficiency, and increased complexity of design and operation. The semiconductor optical amplifier (SOA) is a very compact device that can be used as an alternative for amplification of short pulses. Its drawbacks include a shorter gain bandwidth, and higher noise figure when compared to the fiber amplifier.

The modeling and simulation for the amplification of complex pulses propagating in an Ytterbium doped fiber amplifier is the subject of this thesis. The first chapter is an overview of the laser technology used in the laboratory experiments including a discussion on the importance of numerical modeling in the research. Chapters two and three provide the theoretical foundation, and for each individual topic discuss how it is (or can be) applied to the simulation research that has been carried out for the previous year and a half. Chapter four presents all the new algorithm and modeling technology that has been developed. Chapter five discusses a selection of phenomena that have not been considered in the hitherto modeling. Chapter six contains the bulk of this report with simulation results and verification to experiment. The final chapter imparts what is to be done in future work.

1.1 Optical Fiber Amplifiers

Considerable effort has been focused on the optical fiber amplifier that can be amplified and/or pumped at a very broad range of wavelengths with high efficiency and low loss. The most recognized among such optical devices is the commercially viable

Erbium-doped fiber amplifier (EDFA) which provides amplification at the standard (least lossy 0.2 dB/km) telecom wavelength of $1.55 \mu\text{m}$ [59]. There are many more applications of such technology amplifying light in wavelength regimes outside the capability of excited Erbium dopants. In particular, the Ytterbium-doped fiber amplifier (YDFA) provides for amplification of shorter wavelengths from 976 nm to $1.2 \mu\text{m}$ [45][54][61] and is of considerable interest due to the large gain-bandwidth, efficient pump absorption and coupling it exhibits [68]. The YDFA has been found useful for various (but specific) material manufacturing, magnetic resonance imaging (MRI) [60], and as a pump for stimulated Raman scattering applications in the telecommunications field [62]. Other recent applications include nonlinear frequency conversion and micromachining [63].

1.2 Master Oscillator Power Amplifier Systems

The use of mode-locked semiconductor diode lasers for generation of ultra-short optical pulses at peak wavelengths greater than $1 \mu\text{m}$ have been shown to be very useful and practical, especially provided that the output pulses can be further processed in an optical amplification circuit resulting in high peak-power pulses with ultra-short widths as low as several hundred femtoseconds [56][63]. The master oscillator power amplifier (MOPA) system is the name given to such a circuit that configures a master oscillator followed by a power amplifier. Specific examples of master oscillators include passively mode-locked diode lasers [34], gain-switched laser diodes [14], and mode-locked vertical-external-cavity surface-emitting semiconductor lasers (VECSEL) [63] which produce a circular beam that can couple better with the circular core of the fiber amplifier.

Passive mode-locking in edge-emitting diode lasers is achieved through a stable interaction of a saturable absorber, gain medium, and the physical geometry of the semiconductor laser cavity bounded on both ends by highly reflective dielectric and/or diffraction grating surfaces. The saturable absorber preferentially transmits high intensity waves and absorbs low intensity ones. This process repeats as the unabsorbed waves return (after amplification in the gain medium) to the saturable absorber. The power envelope starts to shape into repeating pulses at a particular repetition rate that is dependent on the geometry of the device. Once this process is stabilized, the diode laser is mode-locked. Gain-modulation of the diode laser can induce active mode-locking. Devices designed to do so do not have a saturable absorber, and the generation of a laser pulse-train occurs from a pulsed optical or electrical injection into the gain medium [84]. The repetition rate of these spikes defines the repetition rate of the output pulse-train and is constrained by the geometry of the gain cavity.

The amplification is usually immediately performed at the output of the oscillator via semiconductor [9][83] or all-optical amplification. For the latter form of amplification, the fiber amplifier is the main tool used as illustrated in Figure 1-1. In this case, the system is referred to as the hybrid MOPA, integrating semiconductor electrical injection devices with all optical ones.

The main purpose of the MOPA is to generate high laser intensities and also to have an additional beam correction capability to modulate or tune the intensity profile, pulse-repetition rate, linewidth and chirp of the pulse train, operations which are performed after the seed source and before the amplifier [83]. This facilitates a means of tending to the disadvantages of the diode laser output, such that they do not overshadow

the many advantages available by this highly efficient and compact source. The diode laser power efficiency is superior to that of gas lasers. For example, to produce milliwatts of required output power, the Spectra Physics 120 HeNe laser needs 50 W of energy while the diode laser may require several hundred milliwatts of electrical power [33]. In addition, the power supplies and cooling components are reduced dramatically providing for the appeal of the compact MOPA system.

These systems can be applied in a variety of applications. Take for example THz pulse generation. THz generation requires high laser intensities, and this is typically provided by the Ti:Sapphire laser system [58]. Alternatively, a hybrid MOPA has been used successfully as a replacement laser source capable of producing the high peak intensity output pulses necessary for THz generation [57].

1.3 Experimental Setup

The primary analysis reported is performed on a Ytterbium-doped fiber amplifier, an amplifier component of a hybrid MOPA system that has been constructed by Andrew Budz [33]. A modified version of this setup is illustrated in Figure 1-1 below with a second laser source that is to be considered for future work (refer to Chapter 7). Note that this is a conceptual drawing, and that the wavelength selectivity due to the gratings is not necessarily the most optimal approach. Replacing the YDFA for an equivalent polarization maintaining fiber (PMF) can be used with a selection of polarization beam splitters to separate two signals as discussed in Chapter 7. The YDFA has been chosen as an amplifying medium due to its spectral overlap with the home-made seeding diode laser [56], high-efficiency, high-gain, and excellent beam quality [42].

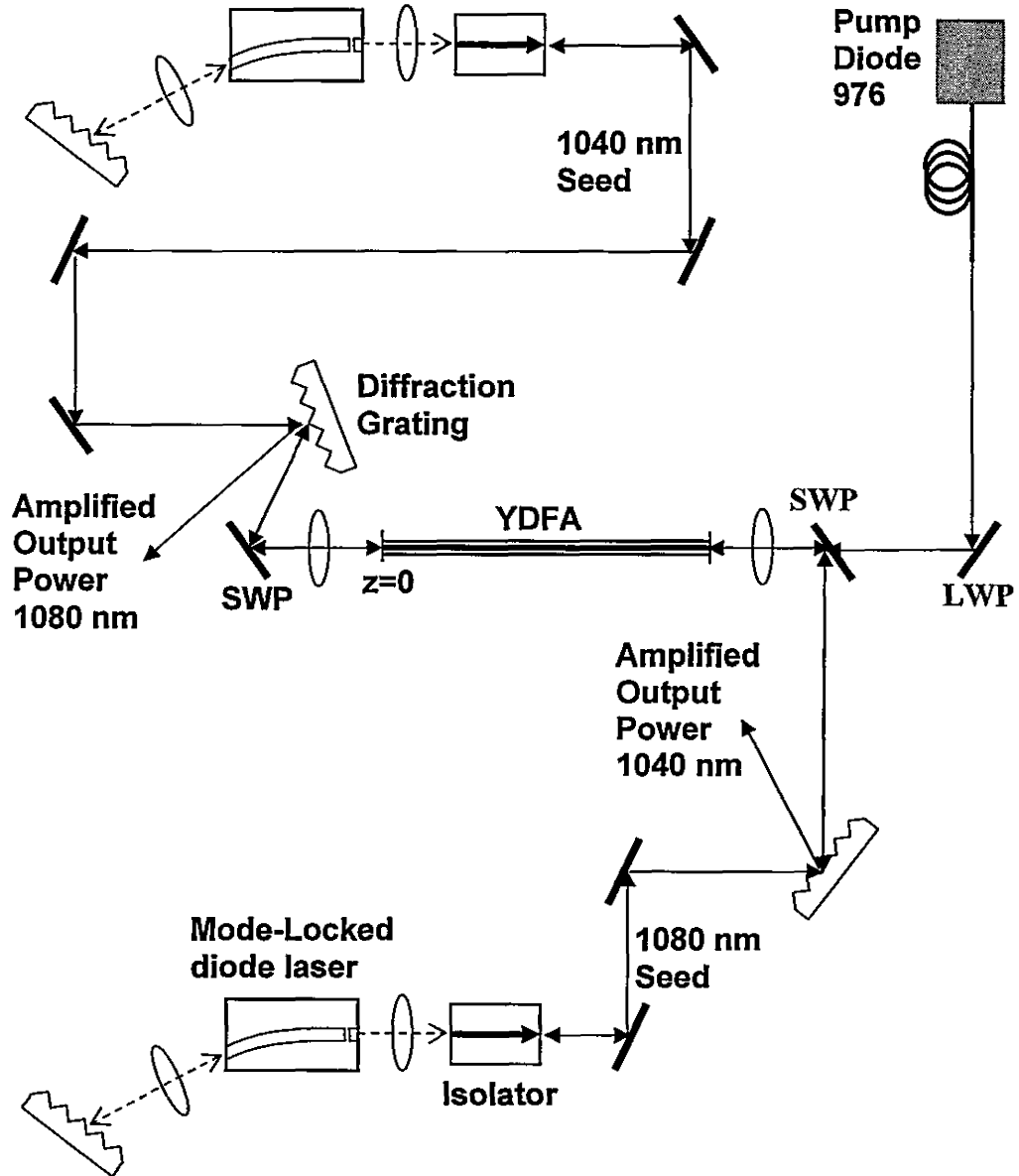


Figure 1-1 Laboratory experimental setup based on work done by Andrew Budz [56]. Achromatic lenses are used to focus and collimate multiple wavelengths of 1040 nm and 1080 nm into and out of the YDFA. Grating orientation can be designed using the diffraction grating equation [82].

1.4 Numerical Modeling Overview

There are numerous articles on how to model the propagation and amplification of light waves in optical fiber amplifiers. The theory is primarily concentrated on numerical modeling of gain and amplified spontaneous emission (ASE) for pulses propagating in optical fiber amplifiers doped with: ytterbium (Yb^{3+}), erbium (Er^{3+}) and thulium (Tm^{3+}), and less commonly with neodymium (Nd^{3+}), praseodymium (Pr^{3+}) and holmium (Ho^{3+}).

For a comprehensive review of all the numerical modeling methods, refer to the article by Giles and Desurvire [17]. In their article, Erbium is used as a platform to model how the signal and pump beams interact with dopant energy population concentrations for gain and ASE. First, it is always necessary to gather as much data as possible on the energy manifold structure of the dopant ion(s) that interact with the seed and pump signals. These include the necessary emission and absorption cross-sections. These are usually either measured experimentally or extracted from data in other journal articles and specialized texts. Next the rate equations and power propagation equations are designed according to a formalism that is common for all modeling papers encountered and usually takes into account one or both of spatial mode distribution and propagating power spectral properties. There are certainly many specific details that need to be considered and are discussed in the following chapters as they are typically specific to the fiber amplifier being analyzed.

Some articles model multiply-doped fiber amplifiers such as for example, in Yelen's erbium-ytterbium co-doped paper for DFB fiber lasers [22]. The only difference from his model and those articles modeling erbium [12][13][17] [73], ytterbium [20][32] [67][74][75], thulium [18][8][41] or neodymium [12][73] alone is an increase in the

number of differential equations. Specifically, in the case of double-doped erbium-ytterbium, all the differential equations for erbium and ytterbium ions alone are included with the additional energy transfer equations from one ion genus to the other as discussed in Chapter 3.

A subset of the aforementioned articles model the continuous wave (cw) signal amplification [18][38][75]. It turns out that with sufficient time-resolution, a pulsed analysis can be used with the same model provided that additional differential equations are considered for each wavelength that is known or expected to have a significant amount of optical energy.

So far, the discussion has been limited to simulations that are capable of modeling gain and ASE of CW and pulsed optical signals. There is a separate numerical analysis called the split-step Fourier method (SSFM) that can be used to analyze the optical propagation in the passive (un-pumped) regime for pulses undergoing dispersion and frequency modulation (refer to Section 2.6). If the emission cross-section can be approximated to a Lorentian function [76][77], then gain can be included into the SSFM model resulting in simultaneous calculation of active and passive effects on a propagating pulse. The cross-sections for the YDFA do not follow the Lorentian function, and thus, the aforementioned SSFM model cannot be used when gain is taken into account, neither can it be used for any of the cross-sections that I have reviewed thus far in the research of modeling doped-fiber amplification.

As the cross-section cannot be modeled to be Lorentian, other methods have to be employed to simultaneously model active and passive events in an optical fiber amplifier. From my experience, most recent work on doped fiber amplifier simulations is performed

in industry. In particular, I had the opportunity to discuss the work done by optical engineers at Optiwave (an Ottawa based company) during the Photonics North conference of 2007. They developed a two-step simulation which first solves for the gain and amplified spontaneous emission (ASE). The results are then processed with the (SSFM) to calculate the passive effects. In other words, they do the entire simulation for the power and then go back and do the passive part. This method does not incorporate both active and passive effects *simultaneously* and therefore is limited for calculations of highly dynamic processes in double-clad doped fiber amplifiers where calculations cannot be made mutually exclusive.

2 Optical Fibers

The optical fiber is a major component of a hybrid MOPA system. It is important to consider how the fiber constrains the electromagnetic (EM) wave traveling through its core. The following sections will introduce the passive fiber effects which will be further explored in the following chapters. Also, the Split-Step Fourier method will be introduced to demonstrate, currently, how passive simulations are made. Every section discusses topics whose details are utilized in future chapters.

2.1 Non-Linear Schrödinger Equation

A good starting point is to introduce the Non-Linear Schrödinger (NLS) Equation 2-1. It describes the dynamic properties of a light pulse as it travels down an axisymmetric optical fiber [2].

$$\frac{\partial A}{\partial z} + \frac{i\beta_0''}{2} \frac{\partial^2 A}{\partial \tau^2} - i \frac{2\pi n_2}{\lambda_0} |A|^2 A = 0 \quad 2-1$$

$A = A(z, \tau)$ is used to describe the envelope of the traveling (longitudinal) pulse at

position z and relative time τ . $\beta_0'' = \left. \frac{d^2 \beta}{d\omega^2} \right|_{\omega=\omega_0}$ is the second derivative of the

wavenumber β with respect to frequency and evaluated at $\omega_0 = \frac{2\pi c}{\lambda_0}$, the center angular

frequency of the pulse. n_2 is a number that represents a third order nonlinearity (or the

Kerr effect). The magnitude of n_2 is a function of the cross-sectional modal distribution $F(x_\perp)$ of the pulse where $(x_\perp) = (x, y)$. The time and frequency domain equations for the traveling pulse in the fiber can be defined as [2]:

$$\begin{aligned}\bar{E}(x_\perp, z, t) &= \hat{e}F\left(x_\perp, \omega_0 + i\frac{\partial}{\partial \tau}\right)A(z, \tau)\exp[i(\beta_0 z - \omega_0 \tau)] + (*) \\ \hat{E}(x_\perp, z, \omega) &= F(x_\perp, \omega)\hat{A}(z, \omega - \omega_0)\exp(ik_0 z) + (*)\end{aligned}\tag{2-2}$$

where \hat{e} is a normalized vector indicating polarization direction, and $(*)$ represents the complex conjugate of the expression to the left of the addition operator. In the above equation, F is a *normalized* cross-sectional distribution of the electric field inside the core of the optical fiber. Other useful properties of this function include $\max(F) = 1$ and $F(x^2 + y^2 \rightarrow \infty) = 0$. The NLS equation is one of several equations that are used in simulating the changes in shape for the traveling pulse. However, the use of this theory is limited to passive effects such as dispersion, attenuation and nonlinear effects.

Passive effects will be discussed further in the following sections. A discussion on active fibers is left for the following chapters. Equation 2-1 is not fully generalized and other physical effects will be introduced into the equation in the following subsections.

2.1.1 The Retarded Reference Frame

The derivation of the NLS equation leads to the following intermediate equation [1][2]:

$$\frac{\partial B}{\partial z} + \beta'_0 \frac{\partial B}{\partial t} + \frac{i\beta''_0}{2} \frac{\partial^2 B}{\partial t^2} - i \frac{2\pi n_2}{\lambda_0} |B|^2 B = 0\tag{2-3}$$

This result comes before Equation 2-1. An observer following the propagation of the pulse using Equation 2-3 has the laboratory frame of reference. That is, the observer

is stationary and views the pulse of amplitude $B(z,t)$ traveling down the fiber from a particular (and static) location. Then, for convenience, a coordinate transformation is made to a “retarded frame of reference” [3][8][24]:

$$\begin{aligned} z' &= z \\ \tau &= t - \frac{z}{v_g} \end{aligned} \tag{2-4}$$

The canonical NLS Equation 2-1 is the result and it describes the dynamics of a pulse to an “observer” that travels with the pulse at the group velocity v_g . When modeling the physics of a propagating pulse, it is important to take note of the reference frame in which calculations are made. For example, in chapter 4 of this report, additional equations are introduced to the calculation process that are initially defined in the laboratory reference frame and are transformed to the retarded frame in order to tailor the physics into a practical simulation.

2.1.2 Amplitude Normalization

The amplitude function $A(z,\tau)$ from the NLS equation has units $[V/m]$. However, in the laboratory, all we can measure is power with units $[W]$. It would be convenient to modify the amplitude function by some constant multiple so that $|A(z,\tau)|^2$ becomes the optical power with units in $[W]$. The constant of multiplication will now be derived.

First, we need to model the real amplitude of our signal. One can only measure the average power (which can be used to infer a peak power) from experiment. The electric field can be expressed as

$$\begin{aligned}
 E(r, t) &= 1/2 E_0 \exp[i(\beta_0 z - \omega_0 t)] + (*) \\
 &= 1/2 F(x, y) A(z, t) \exp[i(\beta_0 z - \omega_0 t)] + (*)
 \end{aligned}
 \tag{2-5}$$

Experimentally measurable intensity (in MKS units) is defined as [1]:

$$\begin{aligned}
 I &= \frac{n}{2Z_0} |E|^2 \quad [W/m^2] \\
 &= cn\varepsilon_0 |A|^2 \quad [W/m^2]
 \end{aligned}
 \tag{2-6}$$

where ε_0 is the permittivity of free-space. The peak amplitude A_0 can be defined with respect to the maximum electric field:

$$\begin{aligned}
 |E|^2 &= [F(x, y)A(z, t)]^2 + [F(x, y)^* A(z, t)^*]^2 \\
 \therefore \max\{|E|^2\} &= [A_0(z, t)]^2 + [A_0(z, t)^*]^2 \\
 &= 2 \operatorname{Re}\{A_0(z, t)^2\} \\
 &= 2A_0(z, t)^2 \quad \text{if } A_0 = \operatorname{Re}\{A_0\} \\
 A_0(z, t) &= \max\{A(z, t)\}
 \end{aligned}$$

The normalized function $F(x, y)$ is defined mathematically to exist throughout the cross-sectional plane and has a maximum value of unity. Most of the optical energy is localized within an area called the effective core area [23][28]:

$$A_{eff} = \frac{\left[\int_{-\infty}^{\infty} \int_{-\infty}^{\infty} |F(x, y)|^2 dx dy \right]^2}{\int_{-\infty}^{\infty} \int_{-\infty}^{\infty} |F(x, y)|^4 dx dy}
 \tag{2-7}$$

If the majority of incident power $P(z)$ with peak power P_0 overlaps the effective core area, then according to Equation 2-6, the peak intensity I_0 can be defined:

$$\begin{aligned}
 I_0 &= \frac{P_0}{A_{eff}} \\
 &= \max \left[\frac{n}{2Z_0} |E|^2 \right] = \frac{n}{Z_0} A_0^2
 \end{aligned}
 \tag{2-8}$$

Re-writing equation 2-8 gives us the relation between the peak amplitude and the corresponding peak power P_0 :

$$\therefore A_0 = \sqrt{P_0} \sqrt{\frac{Z_0}{nA_{eff}}}
 \tag{2-9}$$

If the function $A(z, t)$ gets multiplied by the correct factor (i.e. $\sqrt{nA_{eff}/Z_0}$) then the peak of the instantaneous function $|A(z, t)|^2$ exactly equals the peak power P_0 . More generally, it turns out that the entire normalized-amplitude-squared equals the power for all points in time. The amplitude and NLS equations are modified as follows:

$$\begin{aligned}
 A(z, \tau) &\rightarrow A(z, \tau) \sqrt{\frac{nA_{eff}}{Z_0}} \\
 \frac{\partial A}{\partial z} + \frac{i\beta_0''}{2} \frac{\partial^2 A}{\partial \tau^2} - i\gamma |A|^2 A &= 0
 \end{aligned}
 \tag{2-10}$$

The nonlinear coefficient $\gamma = n_2\omega_0/cA_{eff}$ replaces the old value of $2\pi m_2/\lambda_0$ used for the less-convenient non-normalized amplitude in Equation 2-1.

2.2 Step-Index Fibers

The step index fiber is typically composed of two overlapping cylindrical layers as shown in Figure 2-1. Light propagates down the fiber core under the effective index guiding principle as discussed in Section 2.2.1.

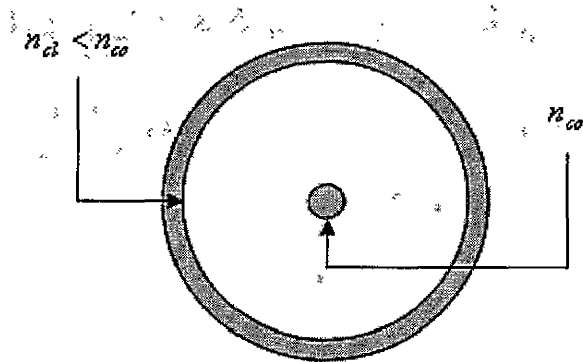


Figure 2-1 The cross-sectional material distribution of a typical step index fiber. The inner core has refractive index n_{co} which is greater than the cladding index n_{cl} . The outer surface is called the jacket and usually has an index of refraction less than the cladding. Also, this fiber is axisymmetric since the refractive index is constant for any $r = \sqrt{x^2 + y^2}$.

2.2.1 Mode-Field Distributions

The cross-sectional EM distribution (regardless of its initial shape) converges to a linear superposition of basis modes that can exist as guided waves in the core of the optical fiber. There are many sources that discuss the distribution in much detail. Equation 2-11 is one version taken from Gloge's article [19] that is defined properly in the context of the simulator since it directly relates the overlap function, power and intensity. It can be implemented as is without any necessary manipulations.

Assuming that the weak guidance condition $\Delta = (n_{co} - n_{cl})/n_{cl} \ll 1$ is satisfied (i.e. the cladding index is almost the same value as the core index), the optical intensity (or the "mode-field") of guided light in the fiber is:

$$I(r = \sqrt{x^2 + y^2}) = \kappa(u^2/V^2) \frac{P}{\pi a^2} \left\{ \frac{J_1^2(ur/a)/J_1^2(u)}{K_1^2(wr/a)/K_1^2(w)} \right\}. \quad 2-11$$

The mode field is therefore defined by the Bessel function $J_1(ur/a)$ inside the core ($r \leq a$) and the modified Hankel function $K_1(ur/a)$ outside the core ($r \geq a$). $P = P(z)$ is

the total power (in Watts) present at position z at which we consider our cross-section.

The core-diameter is defined as $2a$, and the remaining parameters are expressed as

$$\left(\frac{u}{a}\right)^2 = k^2 n_{co}^2 - \beta^2 \quad 2-12$$

$$\left(\frac{w}{a}\right)^2 = \beta^2 - k^2 n_{cl}^2 \quad 2-13$$

$$V = \sqrt{u^2 + w^2} = \sqrt{a^2 k^2 (n_{co}^2 - n_{cl}^2)} = \frac{2\pi}{\lambda} a \cdot NA \quad 2-14$$

$$\vec{k} = (k_x, k_y, \beta) \quad k = |\vec{k}| = \sqrt{k_x^2 + k_y^2 + \beta^2} \quad 2-15$$

The numerical aperture (NA) is discussed in Section 2.2.3, and β is the propagation constant defined as $\beta = \vec{k}(\omega) \cdot \hat{z}$ with limits $n_{cl}k \leq \beta \leq n_{co}k$.

As the value of the core index approaches that of the surrounding inner cladding (i.e. $n_{co} \rightarrow n_{cl}$), fiber guiding gets weaker and J_l does not exist for positive orders with $l > 0$. In other words, $\beta \rightarrow n_{cl}k$ and as a result the mode-field no longer feels the step-index. The only propagative solution remaining called the first order mode, is $J_0(u)$, which necessarily has $\beta > n_{cl}k$ (although this solution can also reach cut-off when $u = 0$ and therefore $\beta = n_{cl}k$).

In the simulation, the first order mode is approximated as Gaussian throughout the two radial regions. This approximation is discussed thoroughly in section 3.1.1.

2.2.2 Input Pulse Distributions

In the previous section, I discussed the cross-sectional spatial distribution of the signal mode. In this report, the primary analysis of the optically amplified signal is

performed on its longitudinal distribution (down the fiber). This can also be performed spatially, however it is more natural to discuss it in the temporal perspective.

The shape of the pulse incident at the fiber facet is usually bell shaped with a single peak. This can be seen below in Figure 2-2 with respect to time from the autocorrelation traces of pulses generated in the ultra-fast laser lab.

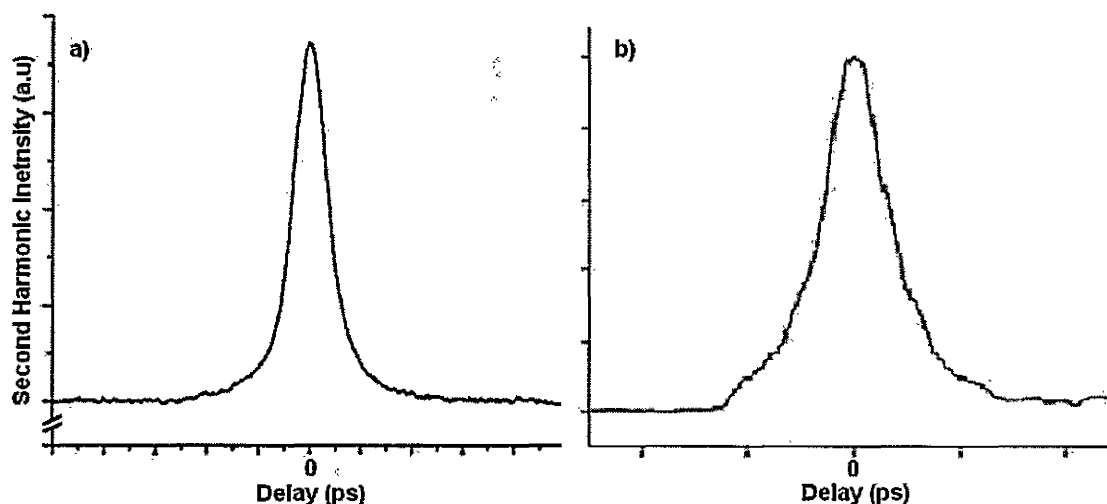


Figure 2-2 Autocorrelation trace of a pulse generated from a mode-locked diode laser taken from a) [9] and b) [14].

There are two major functions used to model this in a simulation. These are the Gaussian distribution and hyperbolic secant squared function as tabulated in

Table 2-1. There are two generally accepted methods of providing a metric to the width of a pulse (Appendix A). These are the full-width at half the maximum (FWHM), and the $1/e$ width called the root-mean-square (RMS). These have analytic representations for the two pulse distributions given in the following table.

Table 2-1 Properties of Gaussian and sech^2 functions commonly used as input pulse power distributions in simulation runs. FWHM is the full-width at half maximum pulse peak power, and RMS is the root-mean-square.

Pulse Distribution	Instantaneous Power	FWHM
Gaussian	$P_0 \exp\left(-\frac{\tau^2}{T_0^2}\right)$	$1.6651T_0$ (RMS = T_0)
Hyperbolic Secant	$P_0 \text{sech}^2\left(\frac{\tau}{T_0}\right)$	$1.763T_0$

The aforementioned functions can approximate the output pulse of a mode-locked diode laser and can be used in the simulation validation process. For example, if an input pulse is defined as Gaussian, then (as verified in Chapter 6) the pulse spread due to dispersion after a predefined propagation length can be calculated analytically and compared in a verification test of the simulator outputs for the same operating conditions.

Theoretical pulses are defined on a continuum of data points up to time infinity. This cannot possibly be represented in our computer systems and therefore, the pulses are approximated by a set of sample points. Just how many samples must be taken to prevent aliasing is somewhat discussed in Chapter 5, but is in general outside the scope of this report. The sample number also depends on the time resolution that is required. This cannot be solved until a decision is made as to just how far out in time the pulse is defined. We define the pulse boundary coefficient (PBC) for the Gaussian pulse with peak power defined at time $t = 0$ seconds such that the principle leading and trailing data points correspond to the following times respectively:

$$t_{MIN} = -1.0 \times FWHM \times PBC$$

$$t_{MAX} = +1.0 \times FWHM \times PBC$$

Therefore, the initialization of the pulses is defined according to the requested full-width at half maximum and the pulse boundary coefficients. There are many other methods of defining the input pulses, but this way I could limit the number of variables used in the software. Values for PBC are always positive and are typically set from 2.5 to 20.0. The decision is based on experience in working with the system, as one must consider the sampling frequency, those passive and active effects that are included in the simulation, and what level of accuracy is required when deciding on PBC.

2.2.3 Numerical Aperture

It is important to consider at what angles light rays can successfully couple into the inner core of the optical fiber. The numerical aperture (NA) is the metric used for this measurement and is defined in Equation 2-16 [6].

$$NA = n_0 \sin \alpha_{\max} = \sqrt{n_{co}^2 - n_{cl}^2} \quad 2-16$$

In the above equation α_{\max} is the maximum angle (in radians) with respect to the normal of the fiber facet that a light ray enters into the fiber core. Note also that α_{\max} varies with wavelength since any material refractive index $n = n(\lambda_0)$ is wavelength dependent to some degree.

2.3 Chromatic Dispersion

A monochromatic light source has a unique wavelength and propagation velocity that is fully defined by the medium in which it travels. A pulse is a superposition of many such monochromatic waves [7] each with a distinct amplitude, wavelength and velocity, where the velocity is inversely related to the index of refraction which is in turn a

function of the wavelength. If different spectral components of a pulse envelope travel at different velocities, then after some distance, the pulse shape changes accordingly. This form of pulse shaping is called chromatic dispersion which can be broken down into two categories: Material and waveguide dispersion.

Material dispersion is defined as a pulse spread in time after traveling a predefined distance L . The pulse spread per unit length is quantified by Palais [5] to be:

$$\Delta(\tau/L) = -\frac{\lambda}{c} \frac{d^2 n}{d\lambda^2} \Delta\lambda = -D\Delta\lambda \quad 2-17$$

Here the dispersion parameter D is measured in $ps/(km \cdot nm)$ and $\Delta\lambda$ is the bandwidth of the pulse in question. To calculate pulse dispersion, we simply solve for the delay $\Delta\tau = -D(\lambda_0)L\Delta\lambda$ where λ_0 is the peak wavelength of the propagating optical energy. For zero dispersion or zero group velocity dispersion (discussed in the following section), the value of the dispersion parameter D is zero. The dispersion of a pulse can be normal or anomalous which corresponds to a negative or positive dispersion parameter (or second derivative of the index of refraction) respectively.

The boundary conditions of a fiber waveguide (including the core radius) define the effective index for a mode having a particular wavelength, corresponding to a core and inner clad refractive indices. The velocity of this mode is a function of the effective index. Each wavelength component of a propagating pulse having some finite bandwidth has a slightly different spatial energy distribution within the core and inner cladding layers once again due to the boundary conditions. This gives rise to a unique effective index for each of these spectral components of the pulse, and also a distinct modal velocity. Dispersion of the pulse will arise due to a spread in spatial mode velocities for

each of the spectral components. In general, waveguide dispersion is small compared to material dispersion and can be disregarded in most simulations except where the peak wavelength in question is close to the zero-dispersion wavelength λ_D as described by Agrawal [3].

For a fiber which is not single mode, modal dispersion must also be considered [5].

2.3.1 Group Velocity Dispersion

The NLS equation is essentially a dispersion operation on the (incident) pulse amplitude $B(z, t)$. Using Equation 2-3, the dispersion operator D is defined:

$$D(\beta(\omega))B = 0 \quad 2-18$$

where

$$D(\beta(\omega)) = \frac{\partial}{\partial z} + \beta_0' \frac{\partial}{\partial t} + \frac{i}{2} \beta_0'' \frac{\partial^2}{\partial t^2} - i \frac{2\pi n_2}{\lambda_0} |B|^2$$

More generally, the dispersion operator can be defined as a second order Taylor expansion [2]:

$$\begin{aligned} D(\beta(\omega)) &= \frac{\partial}{\partial z} - i \frac{2\pi n_2}{\lambda_0} |B|^2 - i\beta \left(\omega_0 + i \frac{\partial}{\partial t} \right) \\ &\cong \frac{\partial}{\partial z} - i \frac{2\pi n_2}{\lambda_0} |B|^2 - i\beta(\omega_0) + \beta_0' \frac{\partial}{\partial t} + i \frac{\beta_0''}{2} \frac{\partial^2}{\partial t^2} \end{aligned} \quad 2-19$$

where $\beta(\omega) = n(\omega)\omega/c$. Here, $n(\omega)$ is the (linear) effective refractive index discussed earlier in section 2.2.1, and n_2 corresponds to an intensity dependent refractive index reviewed below in section 2.4. The nonzero constant β_0'' causes a frequency chirp on the pulse called the group velocity dispersion (GVD). This frequency chirp can be either

blue-chirped (red-shifted) or red-chirped (blue-shifted) after some distance resulting from a positive or negative value for the double differentiation of the refractive index respectively [52]. Normal dispersion (or blue-chirp) occurs in the former case, while anomalous dispersion (or red-chirp) occurs in the latter. For a detailed discussion on the GVD of the pulse, refer to Agrawal's text [3].

2.4 Self Phase Modulation

When the index of refraction is modified by the intensity of the propagating pulse, the frequency of the pulse changes in a manner such that the pulse is red-shifted or in other words that large wavelengths are present in the leading edge of the pulse while small wavelengths make up most of the energy at the trailing edge. Since the pulse does this to itself, the phenomenon is well named as self-phase modulation (SPM).

In the NLS equation, the effect of SPM is mathematically expressed by the term $\gamma = n_2\omega_0/cA_{eff}$ (in Equation 2-10 above), and it can be shown that the refractive index n and its nonlinear component n_2 are defined respectively [2]:

$$n(\omega, |E|^2) = n_0(\omega) + n_2(\omega)|E|^2 \quad 2-20$$

$$n_2 = \frac{1}{2} \frac{k_0' \langle F, \chi^{(3)}(F \cdot F) F^* + 2\chi^{(3)}(F \cdot F) F \rangle}{\langle F, n(n\omega_0/c)' F \rangle} \quad 2-21$$

The derivation of Equation 2-21 is beyond the scope of this report, however, it is important to note that the strength of the SPM effect is a function of n_2 which is in turn a function of the modal distribution $F(x_1, \omega)$ of the pulse (Equation 2-2) as well as the standard third order nonlinearity $\chi^{(3)}$ for an isotropic and centrosymmetric material such

as silica (the host material for the dopants in the optical fiber core). The value of n_2 is experimentally measurable, and has been taken to be $2.2 \times 10^{-20} \text{ m}^2/\text{W}$ for silica, the YDFA core background material. Clearly, the effect of SPM on a propagating pulse is governed by the intensity of the pulse and is not normally uniform throughout the cross-sectional plane. It would be interesting to design an experiment on modal distributions that would target exotic SPM effects on the propagating pulse.

The most common way of summarizing SPM begins by defining the intensity dependant refractive index (in contrast to that defined for the electric field earlier) [1][2][3][23]:

$$n = n_0 + n_2^I I \quad 2-22$$

where n_2^I , a multiple of the intensity I [W/m] is used instead of n_2 defined earlier as a multiple to the square of the electric field (Equation 2-20). For high intensities, the phase of the propagating pulse changes accordingly:

$$\exp[i(\beta_0 z - \omega_0 \tau)] \rightarrow \exp\left[i\left(\left(\beta_0 + \frac{2\pi}{\lambda_0} n_2^I I\right)z - \omega_0 \tau\right)\right]$$

If the pulse propagates a length L down the optical fiber, a nonlinear phase, ϕ_{NL} accumulates on the pulse due to SPM. This nonlinear phase has an instantaneous differential component $\delta\omega$ that contributes to the (now time-dependent) frequency $\omega(t)$.

With Gaussian input pulse intensity $I_0 \exp(-\tau^2/T_0^2)$, the instantaneous frequency (or time-differentiation of phase) at length L is expressed as:

$$\omega(\tau) = \omega_0 + \frac{4\pi n_2^I L I_0}{\lambda_0} \frac{\tau}{T_0^2} \exp(-\tau^2/T_0^2) \quad 2-23$$

and is illustrated in Figure 2-3 c and d below. In part d of this figure, one will notice that due to the frequency chirp (described by the second term on the right of Equation 2-23), long wavelength (or low frequency) components move toward the leading edge of the pulse and those components with small wavelengths (or high frequency) move toward the trailing edge as the pulse travels down the fiber.

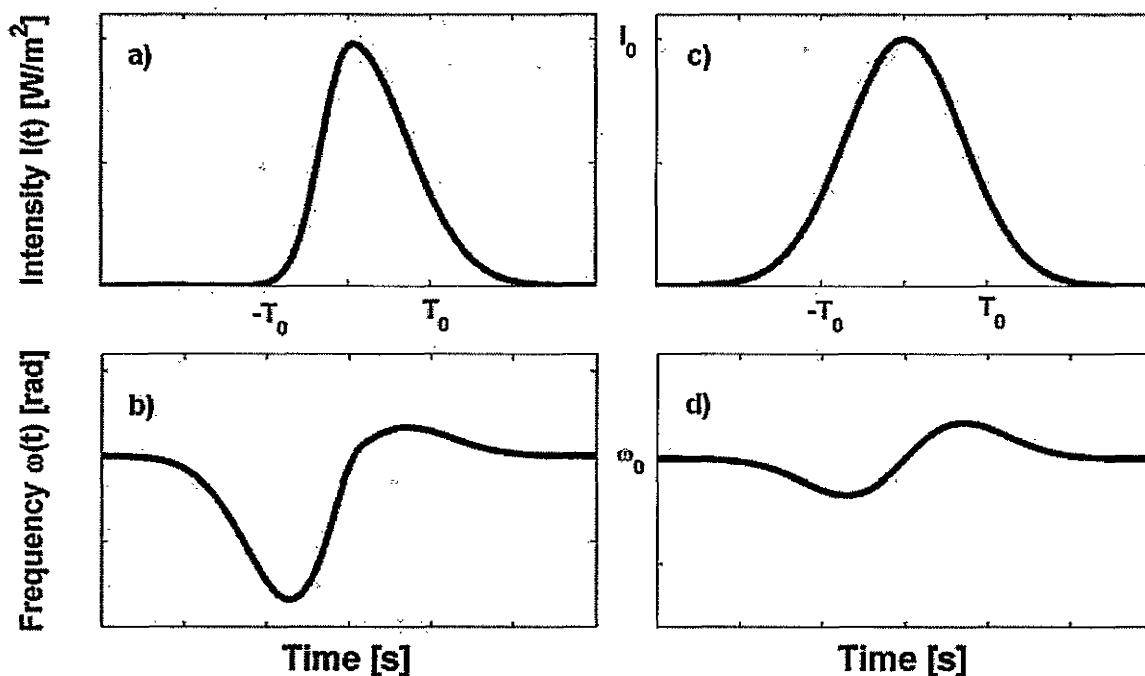


Figure 2-3 Red shift of an a) asymmetric Gaussian pulse (envelope) traveling through a nonlinear medium whose b) instantaneous frequency gets chirped due to SPM. Results for the regular Gaussian pulse are plotted in c) and d) respectively. Variation of instantaneous frequency is proportional to the time rate of change of the pulse intensity. This can be observed in the contrast of the two bottom plots.

The red-shift of the pulse is a spectral phenomenon and does not have any immediate effect on the pulse in the time domain, however if the pulse is traveling through a dispersive medium which is the case for all materials in the scope of this thesis, the pulse shape in the time domain changes accordingly due to the frequency chirp from SPM.

2.5 Polishing Angle and Fresnel Loss

The Yb-doped fiber amplifier used in the laboratory MOPA system is designed to be a single traversal system. That is, the series of pulses should travel through the core once (for amplification) and exit the other end. To keep the pulses from reflecting back into the oscillator cavity and causing undesirable effects, the facets are cleaved at an angle called the polishing angle which dramatically reduces the back reflection when compared to exit facets normal to the fiber axis.

In the model, all the calculated powers are inside the fiber. The launched pump and signal powers are therefore lower than the values just outside the entrance facet. In addition, the output powers are also reduced due to an identical polishing angle at the exit facet. Just how much of the EM field is lost (or reflected away) can be found by utilizing the Fresnel Equations 2-24 and 2-25 [6], the results of which are fairly accurate assuming smooth facet surfaces.

In the simulator, the polishing angle constant variable is declared as PA and defined at 8° for the laboratory experiment in the ultra-fast laser lab. In the following equations, n is the core background linear refractive index, r_s and r_p are the reflectances for senckrekt (meaning perpendicular in German) and parallel polarizations respectively.

$$r_s = \frac{\cos(\text{PA}) - \sqrt{\frac{1}{n^2} - \sin^2(\text{PA})}}{\cos(\text{PA}) + \sqrt{\frac{1}{n^2} - \sin^2(\text{PA})}} \quad 2-24$$

$$r_p = \frac{-\frac{1}{n^2} \cos(\text{PA}) + \sqrt{\frac{1}{n^2} - \sin^2(\text{PA})}}{\frac{1}{n^2} \cos(\text{PA}) + \sqrt{\frac{1}{n^2} - \sin^2(\text{PA})}} \quad 2-25$$

For either the entrance or exit facet, the incoming power defined as P_{in} will be truncated to a transmitted power defined as P_{out} according to the following expression:

$$P_{out} = (1 - R) \times P_{in} \quad 2-26$$

where $R = \max(|r_s|^2, |r_p|^2)$ ¹. The absolute square of the reflectances is used because we are dealing with powers. The Fresnel's reflectances were originally defined for the EM field. The choice of maximum is an approximation. No matter what ratio of two possible polarizations exists, it was decided early on that the maximum possible loss is accounted as the fiber in the laboratory experiment is not polarization maintaining. Alternatively, one can choose some average value. Typical values used were $|r_s|^2 = 0.036$ and $|r_p|^2 = 0.032$ for a polishing angle $PA = 8^\circ$.

2.6 Split-Step Fourier Method

A common method for numerically simulating the NLS equation for passive operating conditions is the Split-Step Fourier Method (SSFM). This calculation can be used to simultaneously model the following effects for a (possibly chirped) input pulse:

- Group Velocity Dispersion (GVD)
- Self-Phase Modulation (SPM)
- Stimulated Raman Scattering (SRS)
- Background Loss (Attenuation)

¹ $\max(a, b) = \begin{cases} a & \text{if } a \geq b \\ b & \text{otherwise} \end{cases}$

- Higher Order Dispersion

The usefulness of this algorithm is owing to its fast computation time and the accuracy of the results achieved. In particular, the high speed processing capability is due to a Fourier trick discussed below. Equation 2-1 describing the NLS equation for the pulse amplitude propagation can be expressed in the equivalent form [2][3]:

$$\begin{aligned}\frac{\partial A}{\partial z} &= (\hat{D} + \hat{N})A \\ &\equiv \left(\frac{\hat{D}}{2} + \hat{N} + \frac{\hat{D}}{2} \right) A\end{aligned}\tag{2-27}$$

The dispersion and nonlinear operators representing the GVD and SPM operations are defined respectively:

$$\hat{D} = -i \frac{\beta_0^n}{2} \frac{\partial^2}{\partial \tau^2} \quad \text{and} \quad \hat{N} = i\gamma |A|^2.\tag{2-28}$$

Define a real number $h \rightarrow dz$ to be small enough so that the exact solution for the pulse amplitude as it travels from position z to $z+h$ down the fiber is given by:

$$A(z+h, \tau) = \exp\left(h \left(\frac{\hat{D}}{2} + \hat{N} + \frac{\hat{D}}{2} \right) \right) A(z, \tau)\tag{2-29}$$

The Baker-Hausdorff formula:

$$\exp(\hat{D}) \exp(\hat{N}) = \exp\left[\hat{D} + \hat{N} + \frac{1}{2} [\hat{D}, \hat{N}] + \frac{1}{12} [\hat{D} - \hat{N}, [\hat{D}, \hat{N}]] + \dots \right]\tag{2-30}$$

can be used to approximate the exact solution for the amplitude propagation:

$$A(z+h, \tau) \cong \exp\left(\frac{h}{2} \hat{D} \right) \exp(h \hat{N}) \exp\left(\frac{h}{2} \hat{D} \right) A(z, \tau)\tag{2-31}$$

The operators are non-commuting (i.e. $[\hat{D}, \hat{N}] = \hat{D}\hat{N} - \hat{N}\hat{D} \neq 0$) and therefore the amplitude approximation as presented above is accurate to 3rd order. This is a *symmetric*

SSFM, and its application to the fiber amplifier starts by analytically partitioning the fiber into N steps each with distance $h = \Delta z$:

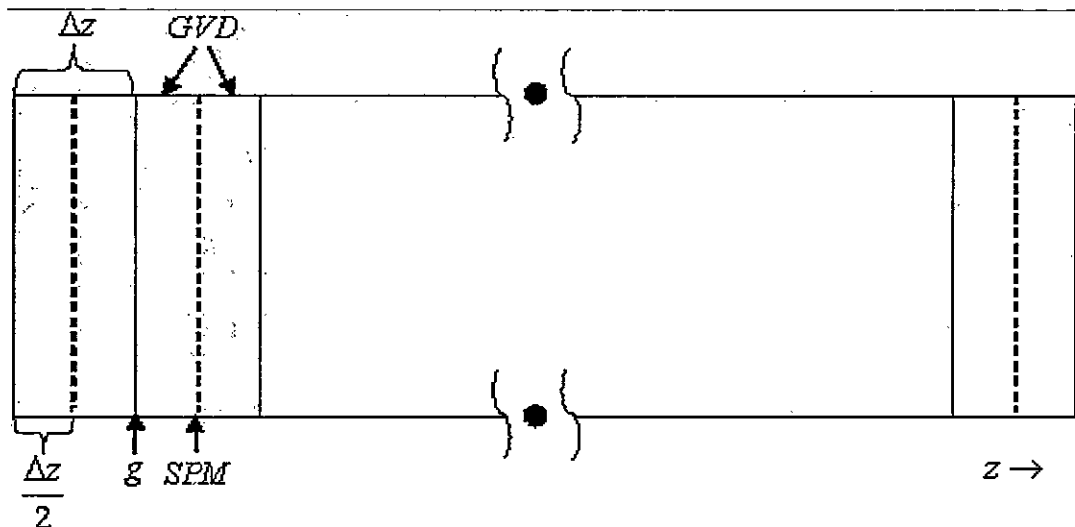


Figure 2-4 The SSFM breaks the fiber (outer solid rectangle) into N steps (inner solid rectangles) with each step calculating one operation of SPM (at the dashed lines) in between two operations of GVD. The gain variable $g = g(z, \tau)$ is discussed in the following chapters.

Suppose that the pulse has traveled some distance down the fiber and is propagating through the i^{th} step. To traverse through this section, the incoming amplitude will transform according to the three operations in Equation 2-31 above. The difficulty lies in the dispersion operation. It can be shown that this calculation is surprisingly simple and fast to calculate as a multiplication in the frequency domain:

$$\exp\left(\frac{h}{2} \hat{D}\right) A(z, \tau) = IFFT\left(\exp(iaK^2) FFT(A(z, \tau))\right) \quad 2-32$$

where $a = (\beta_0''/2)(dz/2)$ and K is the FFT discrete frequency index. First the amplitude function is transformed using the FFT with respect to the τ variable. The result is then multiplied by an exponential factor, and the result of that is transformed back to the time

domain via the inverse fast Fourier transform (*IFFT*). The proof of this result is provided in Appendix B. This operation is extremely simple and fast compared to any alternatives for the application of the complicated differential dispersion operator \hat{D} on the propagating amplitude function. The pseudo-code for the SSFM is as follows for the i^{th} step of the fiber:

1. $A\left(z + \frac{dz}{2}, \tau\right) = \text{IFFT}\left(\exp\left(i\frac{\beta_0''}{4} dz \cdot K^2\right) \text{FFT}(A(z, \tau))\right)$
2. $A\left(z + \frac{dz}{2}, \tau\right) = \exp\left(i\frac{2\pi n_2}{\lambda_0} dz \cdot \left|A\left(z + \frac{dz}{2}, \tau\right)\right|^2\right) A\left(z + \frac{dz}{2}, \tau\right)$
3. $A(z + dz, \tau) = \text{IFFT}\left(\exp\left(i\frac{\beta_0''}{4} dz \cdot K^2\right) \text{FFT}\left(A\left(z + \frac{dz}{2}, \tau\right)\right)\right)$

The above three steps will calculate the GVD and SPM effects on the amplitude (to 3rd order accuracy) from the entrance facet of the fiber to its end. The remaining passive effects are now included in the following generalized NLS equation:

$$\frac{\partial A}{\partial z} + \frac{\alpha}{2} A + \frac{i\beta_0''}{2} \frac{\partial^2 A}{\partial \tau^2} - \frac{1}{6} \beta_0''' \frac{\partial^3 A}{\partial \tau^3} - i \frac{2\pi n_2}{\lambda_0} \left[|A|^2 A + \frac{i}{\omega_0} \frac{\partial}{\partial \tau} (|A|^2 A) - T_R A \frac{\partial |A|^2}{\partial \tau} \right] = 0$$

2-33

where β_0''' is a third-order dispersion briefly discussed in section 5.9, and the last two components on the left-hand-side are the self-amplitude modulation [3][66] and stimulated Raman scattering (Section 5.10), both of which are products of the Kerr effect. In the former case, provided that the pulse width is greater than a picosecond $T_0 \geq 1$ ps and the time-frequency product $\omega_0 T_0 \gg 1$ for an operating frequency ω_0 , then according to Agrawal [3] self-amplitude modulation has limited effect on the pulse

envelope and can be zeroed in the SSFM calculations. This is the case for $\lambda_0 = 1075 \text{ nm}$, the peak wavelength of the picosecond-pulses generated in the laboratory experiment.

3 Optical Amplification in Doped Fibers

In the following discussion, active effects will be added to the theory of passive fiber pulse propagation which was discussed in the previous chapter. At the end of this chapter, a most useful simulation model will be introduced to demonstrate how gain and ASE can be calculated for active fiber simulations.

3.1 Double-Clad Fiber Amplifiers

A fiber with an extra layer of cladding (before the outer jacket cladding) and a doped core is referred to as a double-clad fiber amplifier. This allows one to use high powered yet inexpensive multimode pump lasers to be easily coupled into the inner cladding. The pump is focused down to the inner cladding diameter instead of the core which can better avoid the damage limit of the fiber. A percentage of the pump still overlaps the active core to provide gain for a core-propagating signal.

It is important to note that the physics of the double-clad fiber with respect to light propagation in the core is the same as that for the step-index fiber discussed in the previous chapter.

Inner cladding geometries vary significantly. For example, in Figure 3-1, two double-clad fiber cross-sections are illustrated. These are used in modeling for the double-clad ytterbium-doped and thulium-doped double-clad fibers reported in Chapter 6.

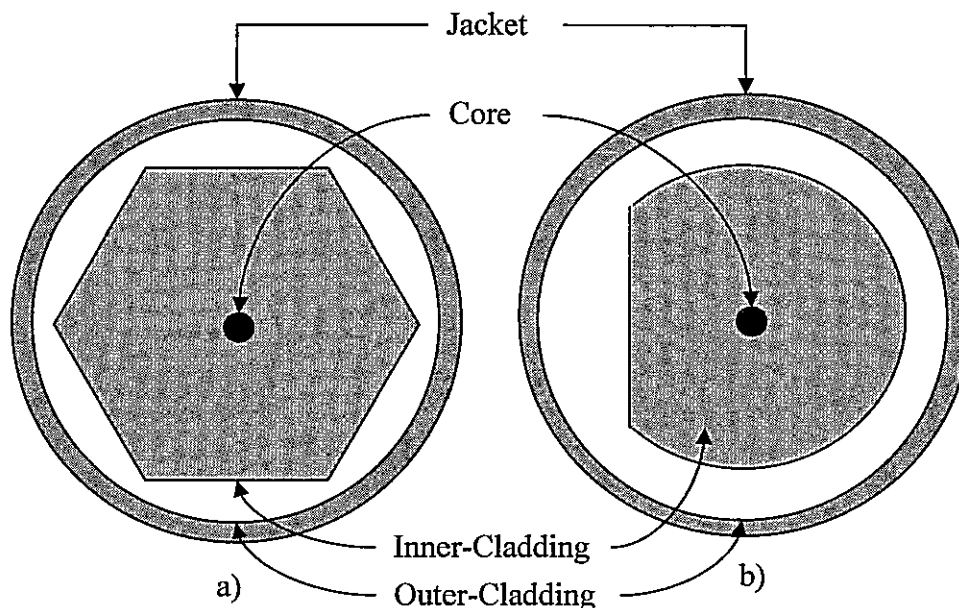


Figure 3-1 The double-clad cross-sectional geometry for the a) hexagonal and b) D-shaped fibers used in the simulations of Chapter 6.

Double-clad fibers with irregular inner-clad geometries such as those shown in Figure 3-1 are commonly called “chaotic fibers”. Qualitatively, this means that the pump power reflects in random directions so that the energy would have a greater probability of overlapping the core and thus exciting the dopant population at some point down the length of the optical fiber.

There are available analytical techniques to calculate the pump absorption characteristics for such double-clad fibers. The prescription for such a measurement is the absorbable power ratio $\mu = P_a/P_T$. The parameters P_a and P_T are the absorbed pump power and the total pump power incident on the entrance facet respectively. For a double-clad fiber with a circular inner cladding and a core offset from the center by $p[\mu m]$, the absorbable power ratio can be deduced [21]:

$$\mu = \frac{2}{\pi} \left[\frac{r_0 + p}{R_0} \sqrt{1 - \left(\frac{r_0 + p}{R_0} \right)^2} + \sin^{-1} \left(\frac{r_0 + p}{R_0} \right) \right] \quad 3-1$$

Constants r_0 and R_0 are the core and inner cladding radius respectively. Sometimes it is convenient to make the assumption of an effective circular inner-clad geometry with an effective diameter. In such cases, one can utilize Equation 3-1 as an approximation. For example, if modeling a hexagonal inner-clad fiber, the flat-flat (or diagonal-diagonal) distance can be taken as the effective diameter. However, one can go a step further and solve for the actual geometry of the system.

The circular (with or without the offset core) and square cladding geometries have absorbable power ratios derived fully in [21]. The pump power overlap calculations for the hexagonal inner-clad geometry is analyzed briefly in [20] and is the geometry used for our YDFA in the laboratory. In these calculations, ray optics are utilized to model the propagation of fiber modes. Each ray incident on the entrance fiber facet can be projected with one component lying on the cross-section of the fiber (i.e. the x, y dimensions). This projection indicates in which direction light will travel cross-sectionally (i.e. by internal reflections) as the optical field propagates down the fiber.

3.1.1 Overlap Function

Cross-sectionally, the optical power distribution at any z position along the double-clad fiber has, in general, some distribution that is dependent on the fiber design. To model this, it is necessary to know how much power is inside and outside of the waveguide by using an accurate cross-sectional power distribution function. Two overlap

functions are used in simulations to define the distribution of pump and signal power and their overlap with the inner cladding and core respectively.

Pump power is typically launched into the inner cladding of the fiber amplifier. It is assumed that the pump power is uniform within the inner cladding due to the chaotic nature of how the rays travel within this layer of the waveguide. Simply, the overlap function is defined as the ratio of the core area to the inner cladding area:

$$D = \frac{\pi\alpha_{core}^2}{A_p} \quad 3-2$$

This value multiplied with the pump power results in that power which actually pumps the dopants from the lower energy level to their excited states. The interaction between signal and dopant energy populations is very specific, and one cannot make the same homogenous assumptions about the signal power as above for the pump power.

The optical fiber can propagate multiple modes each with distinct intensity distributions. Even in a single mode fiber, the fundamental mode LP_{01} has a non-uniform distribution analytically defined utilizing the first order Bessel function (Equation 2-11). At any position z along the fiber, the total signal power $P_k(z)$ and signal intensity $I_k(z)$ (i.e. power/area) at wavelength λ_k are related by the equation:

$$P_k(z) = \int_0^{2\pi} \int_0^\infty I_k(r, \phi, z) r dr d\phi \quad 3-3$$

Let $P_{s,k} = P_k(z)$ and $I_{s,k} = I_k(r, \phi, z)$, where s indicates signal light whose total power is spectrally divided into K wavelength bins, each bin with discrete index k where $\{k \mid k \in [0, K]\}$. Section 3.8 details how this is implemented in the simulator for signal discretization in the wavelength domain.

Assuming single-mode operation in a double-clad fiber amplifier, one can approximate the intensity distribution as Gaussian [8]:

$$\begin{aligned} I_{s,j}(r,\phi) &= \frac{2P_{s,j}}{\pi w_j^2} \exp\left(-\frac{2r^2}{w_j^2}\right) \\ &= P_{s,j} i_j(r,\phi) \end{aligned} \quad 3-4$$

where i_j is a cross-sectionally distributed function relating the power to intensity at the j^{th} wavelength bin. The effective radius of this Gaussian distributed power is $w_j = a(0.65 + 1.619V_j^{-1.5} + 2.876V_j^{-6})$, where the well-known V-number is defined as:

$$\begin{aligned} V_j &= \frac{2\pi a}{\lambda_j} NA \\ &= \frac{2\pi a}{\lambda_j} \sqrt{n_1^2 - n_2^2} \end{aligned} \quad 3-5$$

Substituting Equation 3-4 into integral 3-3 and integrating from $r = 0$ to $r = a$, the radius of the core, a fraction of the total power results:

$$\Gamma_j P_{s,j} = \left[1 - \exp\left(-\frac{2a^2}{w_j^2}\right) \right] P_{s,j} \quad 3-6$$

The signal overlap function Γ_j quantifies just how much of the total power in the j^{th} mode will interact with the dopants within the fiber core.

Regardless of the approximation made on the mode field distribution, all such choices must always satisfy Equation 3-3. With that in mind, there are other options for a simulation. For example, Cao [29] suggests the following Gaussian distribution:

$$i_j = B \exp\left[-(\ln V_j) R^2\right] \quad 3-7$$

where B is a normalization constant such that $\int_0^{\infty} i_j R dR = 1$ and $R = \frac{r}{w}$.

Giles and Desurvire [17] propose a more general solution to the overlap function concept. In fact, the overlap function is broken into two overlap functions (in the case of Ytterbium dopants) to take into account the overlap with the ground and excited state dopant energy populations (see Appendix C). These equations will be used in future simulations instead of the total overlap function Γ_k used in the current version of the simulator.

3.1.2 Propagation Geometries

Optical beams can enter the fiber at both fiber facets. It is assumed that there is only one signal beam (pulsed or CW) and that it is input from the left side and where the positive convention is set from left to right. The pump beam can enter at both directions as shown in the following figure:

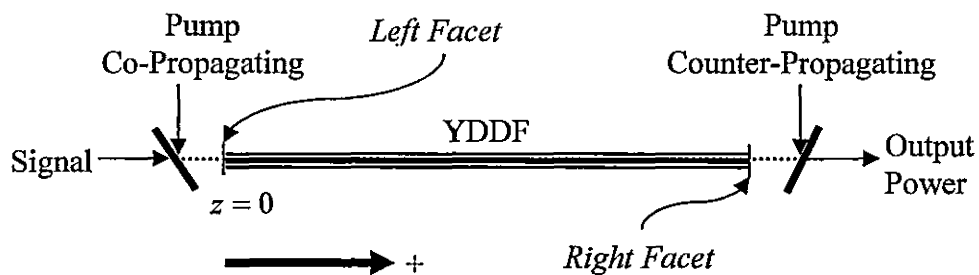


Figure 3-2 Three possible pumping operating geometries for a ytterbium-doped double-clad fiber amplifier. The positive convention is from left to right as indicated by the bottom arrow in the figure.

3.2 Stimulated Emission and Absorption

The coherent amplification of propagating power by stimulated emission of excited ions is the primary means of signal amplification in a doped-fiber amplifier. Background theory on this subject can be found in numerous texts and journals [10]. Just how this is represented in the fiber amplification model is the intention of this section.

As power P travels (say from left to right) in the pumped fiber amplifier core, it interacts with excited and ground state dopants of concentrations N_1 and N_0 [m^{-3}] at a cross-section of σ_e and σ_a [m^2] respectively. Assuming that all the power P is traveling through this active medium, the amount of generated power per unit length is $\sigma_e \times P \times N_1$ [W/m]. Similarly, the amount of absorbed power per unit length by ground state atoms (leading them to become excited) is $\sigma_a \times P \times N_0$ [W/m]. For a travel distance of dz , just from stimulated emission and absorption, the power is expected to change according to the following expression: $P \rightarrow P + (\sigma_e N_1 - \sigma_a N_0) \times P \times dz$. This concept will be expanded in the following sections.

3.3 Rare-Earth Dopants and Their Lifetimes

Ytterbium (Yb), Erbium (Er) and Thulium (Tm) are examples of Rare-Earth dopants that have a useful property that their excitation lifetimes are on the order of milliseconds. This is very important because the spontaneous emission rate is low and consequently laser light would dominate the de-excitation process via stimulated emission.

3.3.1 Radiative Lifetimes

The time τ_{10} it takes a dopant atom to de-excite spontaneously (and without external interference) is referred to as the “Radiative Lifetime”. In considering a macroscopic scale of many atoms (i.e. $\sim 10^{26}$ atoms/ m^3), one can define two energy levels with the higher (lower) energy dopant population density defined as N_1 (N_0) with units of [atoms/ m^3], and the coupled differential equations:

$$\begin{aligned} \frac{dN_1}{dt} &= -\frac{N_1}{\tau_{10}} = -R_{10}N_1 \\ \frac{dN_0}{dt} &= +\frac{N_1}{\tau_{10}} \end{aligned} \tag{3-8}$$

Here, $1/\tau_{10}$ is the rate (per second) at which the dopant population density at the excited energy level N_1 decreases and the corresponding ground-state concentration N_0 increases by that same amount. For the simulation, it is assumed that other energy states are not involved such that $dN_1/dt + dN_0/dt = 0$. The finite energy lost during the de-excitation process manifests as a photon [10]. This photon is assumed to have any direction of propagation throughout the 4π solid angle; however in general, there could be angular dependencies.

In general there is both radiative and non-radiative relaxation and can be calculated theoretically with good accuracy. One recognized method is the Judd-Ofelt analysis which has been used by Walsh and Barnes in their detailed analysis of the Thulium dopant [40].

3.3.2 Non-Radiative Lifetimes

A non-radiative process is an alternative form of energy dissipation of dopant ions from their excited state to some lower (ground) energy level where the energy loss manifests as a phonon, which is a vibrational mode quantized in the crystal lattice of the core material (see Kittel [79] for an excellent review). These phonons can be created or absorbed in the same fashion as the light and matter interactions discussed in Section 3.2 for stimulated emission and absorption. A standard method of calculating the non-radiative lifetimes is discussed by Jackson and King [18].

3.3.3 Excited State Absorption

Excited state absorption (ESA) occurs when a dopant in the excited energy level absorbs a photon from the signal or pump beams and is excited to an even higher energy level (if such a transition is possible). The de-excitation of the dopant ion from that energy level results in phonon generation, or as spontaneous emission (discussed in Section 3.4 below), both of which do not provide any energy for the amplification of the signal.

Analytical expressions for power propagation incorporating an ESA cross-section (or σ_{ESA}) for Erbium and Neodymium doped optical fibers can be found in reference [73]. For the inclusion of ESA into the simulator, a numerical solution provided in reference [13] is to be utilized. The differential equation for a propagating power going through ESA is therefore modified: $P \rightarrow P - \sigma_{ESA} \times P \times N_1 \times dz$ for every spatial step dz .

The Erbium dopant has a 3-level laser scheme. However, there are several higher energy manifolds that can provide for significant ESA if the pump wavelength is not chosen properly [80]. Although there are mixed-dopant optical fibers that include Ytterbium ions with ESA cross-sections available, no articles have been located for Ytterbium ions alone. Due to the large separation of the manifolds in its two energy level scheme, there is no ESA as declared by H.M. Pask [35]. Therefore, there is no need to investigate ESA for the current laboratory experiment; however ESA cross-sections for other dopants such as Thulium and Erbium should always be available for future applications of the simulation.

3.3.4 Cross-Relaxation Tensors

Sometimes, a change in atomic energy levels does not correspond to a creation or absorption of a photon or phonon. In fact, it can happen that two dopant ions interact with one another with the result that both their energy levels change – still satisfying energy conservation laws. This inter-dopant energy transfer phenomenon is also known as quenching [42], coherent up conversion [22], or cross-relaxation [8].

In general, there is a probability that two ions at energy levels i and j interact and exchange energy such that their final energy levels are k and l respectively. The chance that this will happen in a unit of time is defined by the cross-relaxation tensor k_{ijkl} multiplied by the number of dopants in energy levels i and j (i.e. N_i and N_j). The interaction event can be defined mathematically as follows:

$$\begin{aligned}\frac{dN_i}{dt} &= -\left(k_{ijkl}N_j\right)N_i & \frac{dN_j}{dt} &= -\left(k_{ijkl}N_i\right)N_j \\ \frac{dN_k}{dt} &= +\left(k_{ijkl}N_j\right)N_i & \frac{dN_l}{dt} &= +\left(k_{ijkl}N_i\right)N_j\end{aligned}$$

The tensor must operate on two population densities (refer to [44] for an excellent review of tensor calculus). Notice how the power equations are not involved in this calculation as photons are not generated here and energy is simply moved around. Some of these tensor components are known for Thulium or Ytterbium (the dopants used in the simulation research) and these are provided in the following subsections.

3.3.5 Thulium Manifold

The Thulium-doped fiber amplifier has been modeled by the simulator for the purpose of benchmarking pulsed operating conditions. For the case of ZBLAN¹ background material, the energy level model adapted from Eichhorn's article is illustrated in Figure 3-3. During the development process, one of the reasons for choosing this material as a benchmark was due to the abundant data available describing the many energy-matter interactions. Thulium is very interesting because the dominant lasing event is not directly due to the pump, but to the cross-relaxation mathematically defined by the k_{3011} tensor. The cross-relaxation forces two atoms from the zero and third energy levels to interact with the result that both atoms are in the first energy level. Then laser photon generation at $1.85 \mu\text{m}$ occurs as these two atoms are de-excited to the ground state.

¹ ZBLAN is a type of glass that is composed of zirconium, barium, lanthanum, aluminum, and sodium fluorides. It is useful as a core material when performing large wavelength (infrared) fiber amplification experiments.

Without this cross-relaxation process, simulations show that fiber amplification is not possible.

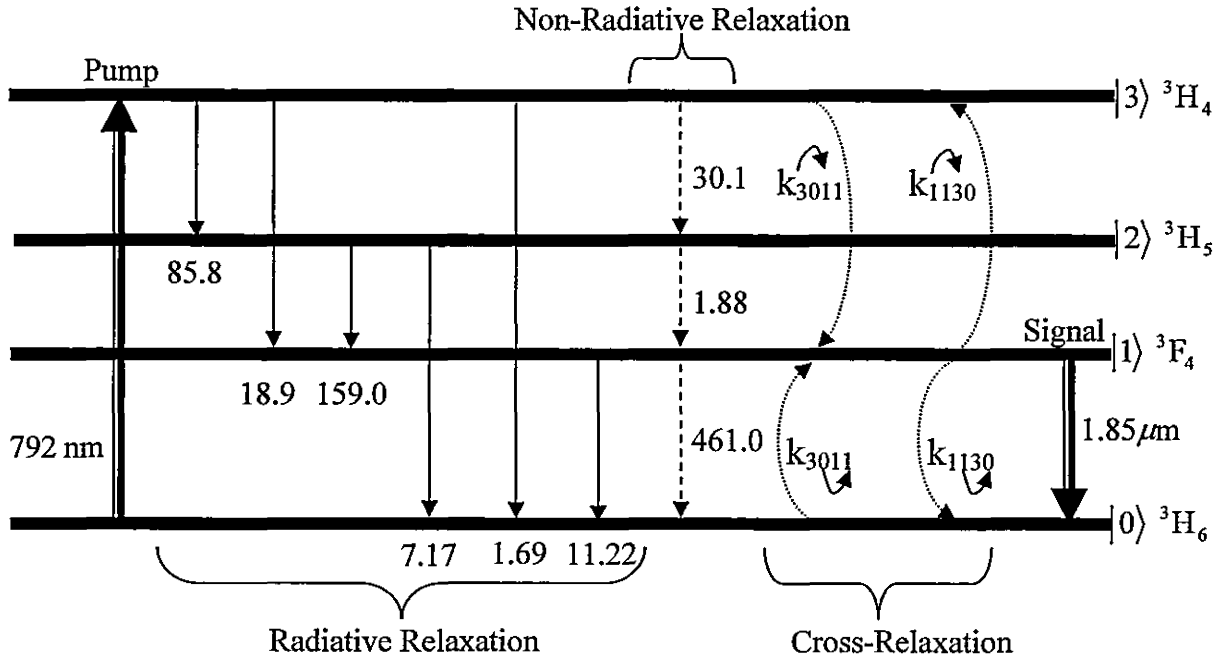


Figure 3-3 Three level laser scheme used for modeling a Tm:ZBLAN fiber amplifier. All numbers without units are in milliseconds. Data is taken from references [8] and [40]. Nonzero tensor values are $k_{3011}=7.86 \times 10^{-24} \text{ m}^3/\text{s}$ and $k_{1130}=6.00 \times 10^{-25} \text{ m}^3/\text{s}$.

There is one more pair of cross-relaxation tensors k_{2011} and k_{1120} that are approximated to zero by Eichhorn [8]. These are however nonzero for Thulium doped fibers of silica host material which has several known cross-relaxation values. These are tabulated by Jackson [18]. The cross-relaxation in this scenario is definitely beneficial for laser action. However, lifetime quenching can be detrimental to the fiber amplification process. This is further explored in section 5.4 for the unsaturable pump absorption.

3.3.6 Ytterbium Manifold

The YDFA has two manifolds where practical laser operation has been performed. Each of these manifolds is broken up into a series of Stark energy levels. The major transitions are illustrated in Figure 3-4.

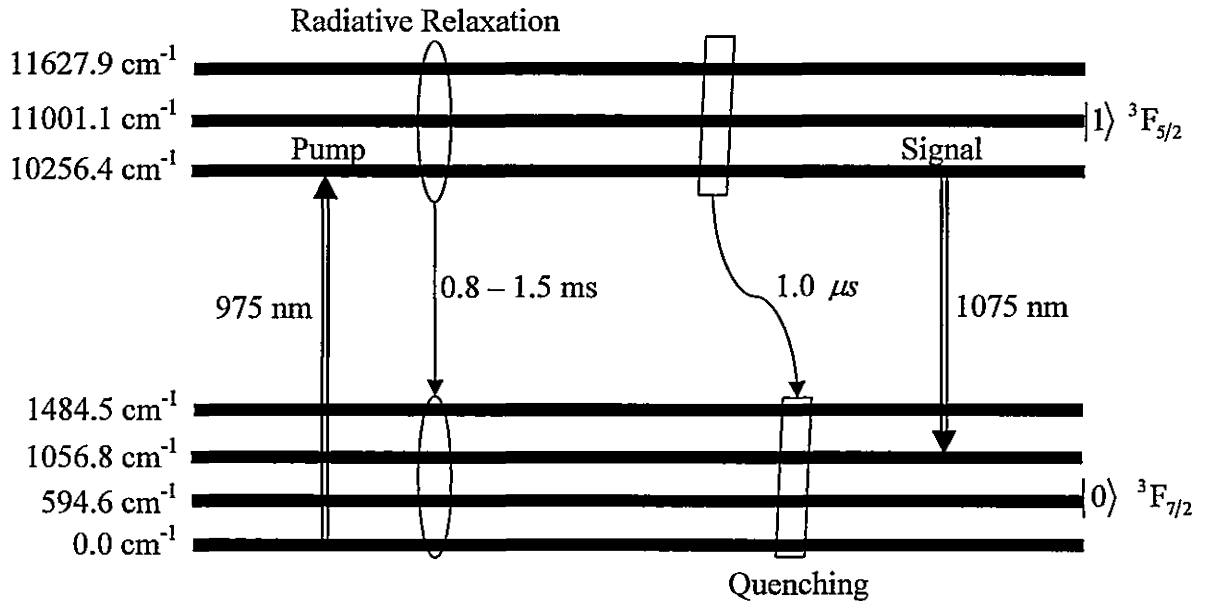


Figure 3-4 YDFA laser scheme with radiative and quenching relaxation process. The quenching relaxation time is under 5 μs according to article [45] and the value of 1 μs is taken from Yelen's article [22].

There are many different radiative processes, however, only one radiative life-time was found in the literature. Its value varies between different YDFAs from 0.8 ms [32] to 1.5 ms [42]. Also plotted are the pump and signal transition schemes used in the laboratory experiment. Many other possible lasing configurations (not indicated in the figure) can take place. For example, a pump at 910 nm can be used to amplify signals at 975 nm. Refer to Paschotta's article [42] for detailed discussions on several operating schemes. There are no significant ESA effects due to the simple energy level structure. However, there can be a quenching process in certain Yb-doped fibers (not conclusively

explained as of yet) that causes an unsaturable absorption of the pump to occur. This fast decay rate is quick and within the microsecond range. Depending on the YDFA, quenched ions can make up from 20% to 90% of the ion concentration in the fiber. Refer to articles [45] and [46] for further details.

3.4 Amplified Spontaneous Emission

Amplified spontaneous emission is another expression for the stimulated emission of excited dopants using vacuum noise always present within the fiber amplifier that can only be explained by quantum mechanics. It is thus inherently a probabilistic event. ASE is the stimulated emission of more photons due to the propagating energy already generated by spontaneous emission. The derivation of ASE in the quantum mechanical context is available in Yariv's text [51].

A simpler semi-classical approach will be shown below. It is based on a 1-D laser resonator geometry also used by Henry [11] to achieve the same result as Yariv. The ASE equation has been used in all articles for the modeling of doped fiber amplifiers and the issue of not using optical fiber geometry in the derivations is further explored in Chapter 5.

Given a one-dimensional Fabry-Perot cavity, a set of standing waves can be defined by the electric field Equation 3-9 below and under the constraints given in Equation 3-10 [15].

$$E(x,t) = E_0 \sin(2\pi x/\lambda) \sin(2\pi \nu t) \quad 3-9$$

$$\nu = cn/2a \quad n = 1, 2, 3, 4, \dots \quad 3-10$$

where a is the resonator length. Taking into account two possible polarizations for each mode, it turns out that the number of allowed modes in frequency range ν to $\nu + d\nu$ per unit length is defined as:

$$N(\nu)d\nu = \frac{4d\nu}{c} \quad 3-11$$

The spectral radiance function for blackbody radiation or in other words the radiated power per unit area per unit frequency interval centered at ν is defined as [6]:

$$I_\nu = \frac{1}{4} c g_\nu h\nu \langle n_\nu \rangle \quad 3-12$$

Variables c , h and ν are the speed of light, Planck's constant and frequency respectively. g_ν is the number of modes per unit frequency interval per unit length, area or volume (depending on the system geometry being calculated). Therefore substitute Equation 3-11 for g_ν . The final variable $\langle n_\nu \rangle$ is the most probable number of photons at frequency ν . It is defined [15] as:

$$\langle n_\nu \rangle = \frac{1}{\exp(h\nu/kT) - 1} \quad 3-13$$

Substituting Equations 3-11 and 3-13 into Equation 3-12 gives [11]:

$$I_\nu = h\nu d\nu \frac{1}{\exp\left(\frac{h\nu - eV}{kT}\right) - 1} = 2m \times h\nu d\nu \quad 3-14$$

where eV is the reference potential of the background material, such as for example, the chemical potential in the context of semiconductors [16]. According to Henry [11], the variable m representing the number of optical modes in the fiber core is usually set to 1 for long-wavelength lasers. In all the gain and ASE modeling articles discussed in

Chapter 1, m denotes the number of modes that are to be amplified. For a single-mode-fiber, this variable is set to unity.

3.5 Absorption and Emission Cross-Sections

There is a wavelength dependent distribution that is used to describe just how much of the propagating power gets absorbed or emitted (by a collection of dopant atoms of predefined concentration) by the process of stimulated absorption or emission. These are the absorption $\sigma_a(\lambda)$ and emission $\sigma_e(\lambda)$ cross-sections respectively with units of m^2 . The power propagation equations incorporate these functions in the following sections.

In the simulations, cross-sections were needed for Thulium and Ytterbium dopants. These are illustrated in Figures 3-5 and 3-6 respectively.

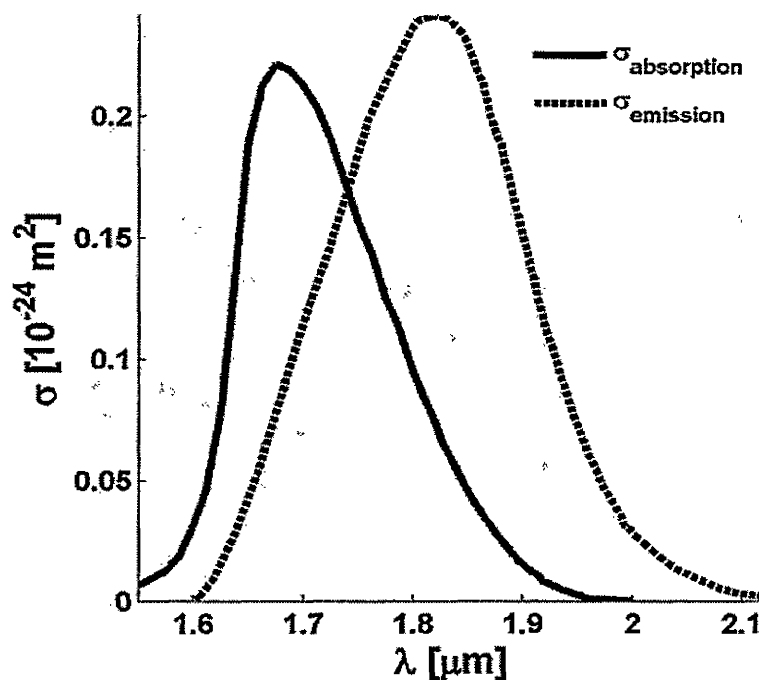


Figure 3-5 Thulium absorption cross-section (solid line) for the signal ${}^3\text{H}_6 \rightarrow {}^3\text{F}_4$ is adapted from Eichhorn's article [8]. Thulium emission cross-section (dashed line) for the signal ${}^3\text{F}_4 \rightarrow {}^3\text{H}_6$ is adapted from Walsh's article [40].

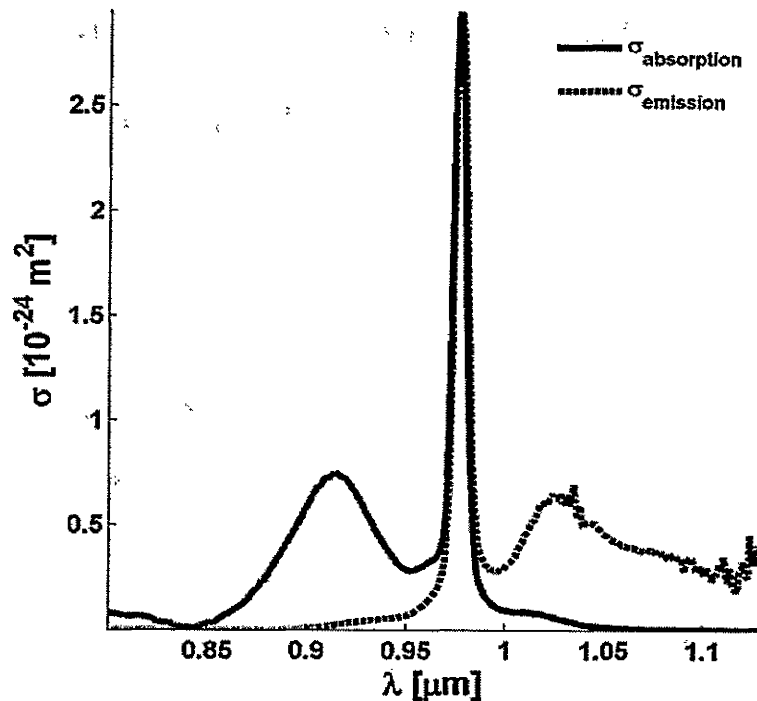


Figure 3-6 Ytterbium absorption (solid line) and emission (dashed line) cross-sections (${}^2F_{5/2} \leftrightarrow {}^2F_{7/2}$) for the YDFA implemented in the ultra-fast laser lab. The data used to plot this figure is provided by CorActive Inc.

For Ytterbium simulations, cross-section data were originally extracted from journal articles [35] and [42]. However, in the subsequent months, we were provided with accurate measured results from CorActive Inc. (the manufacturer of our laboratory YDFA) for the exact fiber that was used in experiment. Refer to chapter 6 for details on our collaborations.

3.6 Rate Equations

In the doped fiber amplifier, dopants are spread out in the core with a distinct population density. The density distribution is usually a function of radius and is axisymmetric. For simplicity, let us assume that it is uniform throughout the core (the validity of this assumption is reviewed in chapter 6).

Earlier, the radiative life-time differential equations were introduced for a two-level manifold. These equations can be generalized to include:

1. EM energy and matter interactions,
2. Radiative and Non-Radiative Relaxations,
3. Cross-Relaxation,
4. ESA,
5. Background losses.

Regardless of the dopants chosen, there is a formalism that is used to define the differential rate equations which can be solved for Ytterbium, Thulium, Ytterbium-Erbium co-doped and other doped optical fibers. This formalism has been used in many articles as presented earlier in Section 1.4. For example, Eichhorn has provided the equations for the 4-level Thulium manifold [8] which have been implemented into the simulations for benchmarking purposes.

The excitation (de-excitation) processes of dopant atoms are followed by a decrease (increase) in the number of photons in the signal and pump beams and this affects power propagation differential equations. This is qualitatively expressed in equation 3-15 where a change in the number of photons $\Delta_{PHOTONS}$ is directly related to the change in the dopant energy level concentrations ΔN . This is the coupled nature of the rate and power equations: There are interrelationships that exist between the optical intensity and the dopant energy populations:

$$\Delta_{PHOTONS} = \frac{\Delta I}{h\nu_{resonant}} \leftrightarrow \Delta N \quad 3-15$$

In the context of Ytterbium with two metastable dopant energy population levels, a decrease (increase) in the number of photons corresponds to an increase (decrease) of the upper (lower) energy population density:

$$\begin{aligned}\uparrow I &\equiv \downarrow N_1 \text{ and } \uparrow N_0 \\ \downarrow I &\equiv \uparrow N_1 \text{ and } \downarrow N_0\end{aligned}\tag{3-16}$$

This phenomenon governs the energy conservation in the simulator. It is very straightforward to infer the rate equations for the YDFA by applying the formalism discussed by Eichhorn [8] for the two-level manifold:

$$\begin{aligned}\frac{\partial N_1}{\partial \tau} &= \frac{N_0}{hc} \sum_{j=0}^h \sigma_a(\lambda_j) \lambda_j \Gamma_j \frac{P_{s,j}^+ + P_{s,j}^-}{\pi a^2} - \frac{N_1}{hc} \sum_{j=0}^h \sigma_e(\lambda_j) \lambda_j \Gamma_j \frac{P_{s,j}^+ + P_{s,j}^-}{\pi a^2} \\ &+ \frac{N_0}{hc} \sigma_a(\lambda_p) \lambda_p D \frac{P_p^+ + P_p^-}{\pi a^2} - \frac{N_1}{hc} \sigma_e(\lambda_p) \lambda_p D \frac{P_p^+ + P_p^-}{\pi a^2} \\ &- R_{10} N_1\end{aligned}\tag{3-17}$$

$$\frac{\partial N_0}{\partial \tau} = -\frac{\partial N_1}{\partial \tau}\tag{3-18}$$

$$\begin{aligned}\frac{\partial P_{s,j}^\pm}{\partial z} &= \mp \alpha_{s,j} P_{s,j}^\pm \mp \sigma_a(\lambda_j) \Gamma_j P_{s,j}^\pm N_0 \pm \sigma_e(\lambda_j) \Gamma_j P_{s,j}^\pm N_1 \\ &\pm \sigma_e(\lambda_j) \Gamma_j M_j \frac{2hc^2}{\lambda_j^3} d\lambda_s N_1 \quad \forall j\end{aligned}\tag{3-19}$$

$$\frac{\partial P_p^\pm}{\partial z} = \mp \alpha_p P_p^\pm \mp \sigma_a(\lambda_p) D P_p^\pm N_0 \pm \sigma_e(\lambda_p) D P_p^\pm N_1\tag{3-20}$$

Since the signal power is not monochromatic, it must be resolved in a set of wavelength bins. $P_{s,j}^\pm(z)$ is the total instantaneous signal power for the j^{th} wavelength bin that is centered at λ_j with a bandwidth of $d\lambda_s$. The superscript $+(-)$ indicates forward (backward) propagation with respect to some positive directional convention within the fiber, a convention mentioned earlier in Section 3.1.2. Also, the notation $\forall j$

stands “for all integer values of j ”. The pump power in Equation 3-20 has been limited to a single wavelength bin. This is an approximation made for all the models that have been encountered for gain and ASE fiber amplification. In reality, the pump power is not monochromatic, as discussed in section 5.5, and the formalism can be easily generalized to further take this into account.

The retarded reference frame is used in the above equations, and hence we use the τ variable instead of t . Refer to Wang’s article [32] for the rate equations in real space-time variables.

3.7 Parabolic Pulse Amplification

So far the Gaussian and sech^2 pulses have been used almost exclusively for the input pulse in the simulations. However, in experiment, it is very difficult to keep these power distributions from undesirable amplitude and phase modulation during propagation. There is, however, a very special pulse called the parabolic pulse [65]. It has the property of maintaining its parabolic shape and more importantly a linear chirp for its entire (nonlinear and amplified) propagation in a fiber amplifier, in the normal dispersion regime, where a high degree of SPM is present. Experimental verification of this was first reported by Fermann *et al.* [47][64][85].

After amplification, it is a simple matter to temporally compress the signal into (or very close to) a transform limited pulse due to the linear chirp. This can be performed using a prism compressor [48] or a special configuration of two grating mirrors [49]. The choice of input parabolic pulse conditions is so specific that the standard experimental

trial and error is a very unattractive approach. Instead, simulators taking into account both active and passive effects should be used before the experiment is set up.

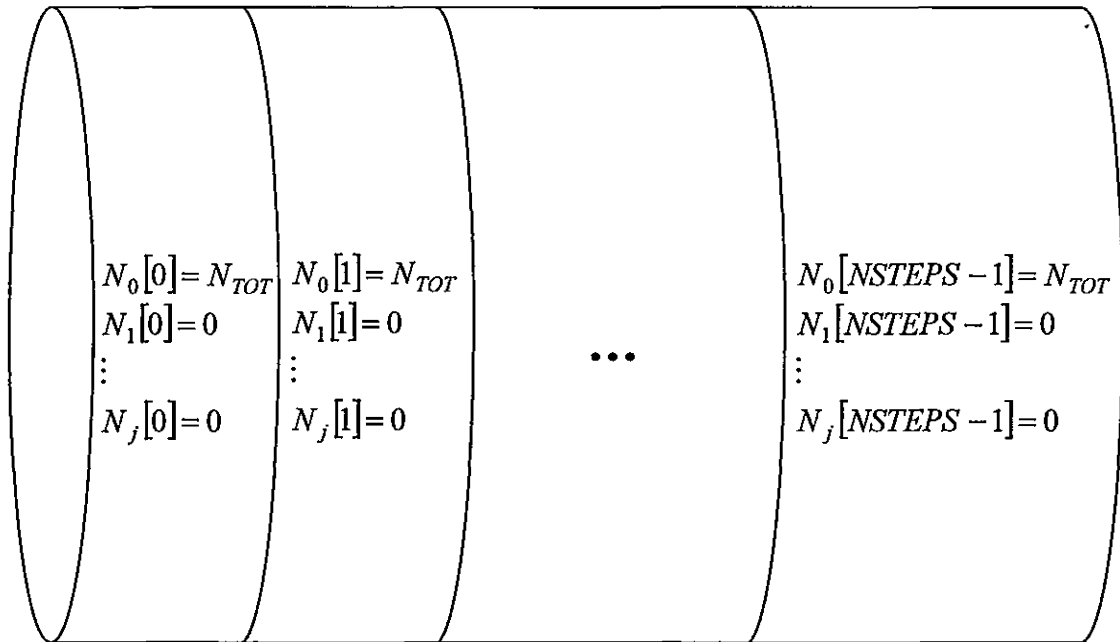
3.8 Standard Pulsed Simulation Algorithm

The population and power propagation rate equations have already been discussed for the Tm-doped ZBLAN fiber and the YDFA in section 3.6. In general, these continuous differential equations must be discretized (such as the power in Equation 3-20) for implementation into algorithms that run using computer array structures. The first order differential equation can be approximated to the following:

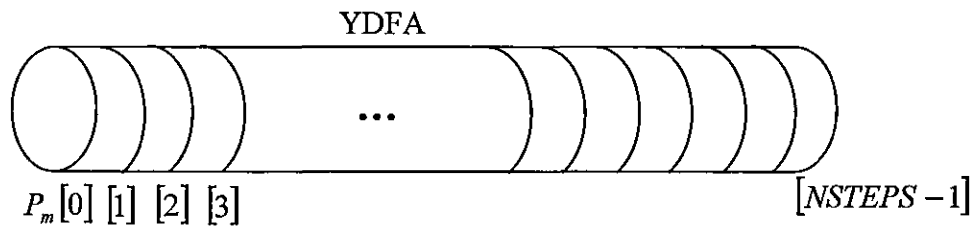
$$\frac{dP}{dz} \underset{\lim \Delta \rightarrow dz}{=} \frac{P(z + \Delta) - P(z)}{\Delta} \quad 3-21$$

Here Δ is a non-zero step which should be taken as small as possible. The accuracy of the simulation depends directly on how close we set Δ to the differential spatial step size dz . To propagate the power for one step to the next via the differential equation $dP/dz = qP$, one must simply evaluate $P \rightarrow P(1 + \Delta \times q)$ where the arrow symbolizes a setting of the left hand side variable to the right hand side. The discretization approach is the same for all differential equations and steps. The simulation is designed to follow the following steps:

1. Set the time step $\tau = 0$
2. Define the dopant energy population arrays and set the ground state population array to the total dopant population concentration N_{TOT} . Remaining upper energy level dopant population arrays are to be initialized to zero.



3. Define the fiber steps and power propagative arrays. Set all array variables to zero, except for the input powers according to the initial conditions (listed below). The powers are defined for each section boundary:



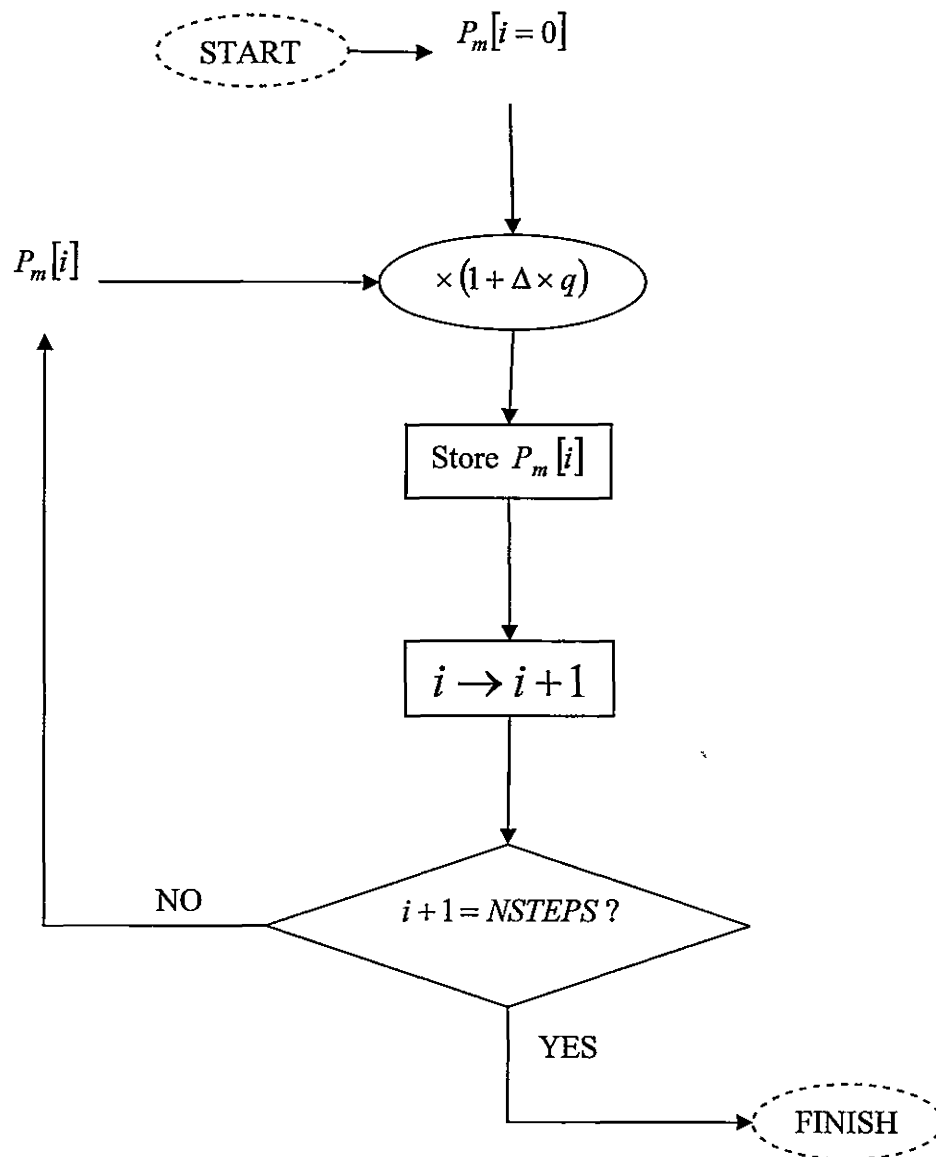
$$P_m[i] = 0 \quad \forall i$$

$$P_p[0] = (\text{left facet}) \text{ Input pump power}$$

$$P_p[NSTEPS - 1] = (\text{right facet}) \text{ Input pump power}$$

$$P_m[0] = \text{Input Signal Power at wavelength } \lambda_m \text{ at time } \tau$$

4. Propagate the (instantaneous) signal and pump powers for the current time step from the left entrance facet to the other (exit) end of the fiber amplifier. This is performed in the following way:



This can be performed simultaneously for all the power types (i.e. signal, ASE and pump powers) and therefore the software can be programmed with multi-threading capability (in this case three threads). In the above diagram, the operators $1 + \Delta \times q$

are defined based on which power is being propagated at the time. For example, if modeling the YDFA, the signal power for the m^{th} wavelength bin is propagated from section i to $i+1$ by the following operator definition:

$$1 + \Delta \times q = 1 + dz \times \left(-\alpha_m + \Gamma_m (\sigma_e(\lambda_m) N_1[i] - \sigma_a(\lambda_m) N_0[i]) + \sigma_e(\lambda_m) \Gamma_m M_m \frac{2hc^2}{\lambda_m^3} d\lambda_s N_m \right)$$

The same formalism applies to the pump power propagation. Suppose that the pump power is input from the opposite (right facet) end. Then the same algorithm is input but in the opposite direction. That is, the input power is $P_p[i = NSTEPS - 1]$, the counter variables are decremented $i \rightarrow i - 1$, and the conditional is checking for $i - 1 = -1$. If in the conditional, the answer is yes, the pump propagation has reached the left fiber facet and the last pump power $P_p[i = 0]$ is calculated.

5. For the current time step, the dopant energy population densities are updated based on their rate equations (section 3.6). In the calculation process, forward propagating powers at the in i^{th} boundary $P^+[i]$ and backward propagating powers in the $i+1^{\text{th}}$ boundary $P^-[i+1]$ are substituted into the rate equation for the dopant concentration in the i^{th} section $N_j[i]$ for all energy levels j . This differential calculation is implemented with a similar algorithm to that illustrated in step 4 above.
6. If the current time step is the last time step in the pulse and there are more pulses in the series, set the current time step to zero $\tau = 0$ and go to step 4, otherwise, end the simulation. If the current time step is not the last time step, increment the current time step $\tau \rightarrow \tau + 1$ and go to step 4.

4 Simulator Innovation

There is a custom algorithm implemented into the simulator used to model both passive and active fiber amplification simultaneously. A mathematical connection had been made by the union of equations used in the SSFM method and those equations used in the power propagation algorithm (of Section 3.9).

After reviewing numerous sources, I located a method in Eichhorn's article [8] that incorporates the power propagation rate equations defined using the retarded reference frame (section 2.1.1). Once I had the amplitude equations for GVD and SPM as well as the power equations for gain and ASE all in the same reference frame, the next task was to link the two theories. I chose to keep the equations the way they were, but to keep track of the energy in the form of amplitude $[V/m]$ as well as power $[W]$ for the pulse when (algorithmically) switching between theories. Obviously, the amplitude has an additional phase, which is not considered in the power propagation equations. To remedy a context switch from the power equations to the amplitude (NLS) equation, an algorithm called the Power to Amplitude (P2A) was developed. Its purpose is apparent from the name – it takes as input the power of the pulse, and returns the complex amplitude. The details of this are discussed in section 4.2. In section 4.3, details on how the simultaneous calculations of active and passive components are made will be provided. The following section summarizes the passive transform (PT) block, which is

the software that propagates the optical energy in two forms: Power and Complex Amplitude.

4.1 Passive Transform Block

Carrying on from any particular junction i along the fiber, the standard power amplification is made according to Section 3.9. Then the gain factor g is extracted using the differential equation $dP/dz = gP$. Assuming that the input amplitude is also known, the following block also calculates using this input power, input amplitude, g , and the output power what the output amplitude should result. The active and passive calculations are made within the PT block for the amplitude function, and it all starts at the first slot where the input amplitude is the only one known a priori.

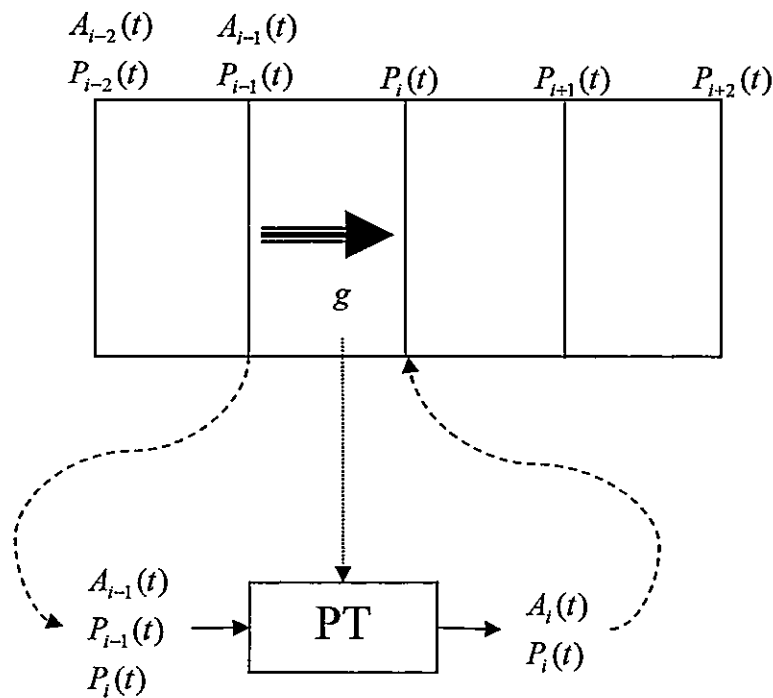


Figure 4-1 The PT block is an algorithm used to propagate the phase of the signal along with the power, or in other words to keep track of the complex amplitude.

The PT block is the finished product representing the overall algorithm used to propagate complex EM waves down the optical fiber amplifier. The inner workings of this block will be discussed further in Section 4.3. Note that the coding implementation of the following software is outside the scope of this report. Suffice it to say that many data structures and algorithms such as the circular array (representing the amplitude function) have been utilized.

4.2 Transforming Pulse Power to Complex Amplitude

During the simulation process, it is necessary to transform the pulse distribution from the complex amplitude $A(z, \tau) = \text{Re}\{A(z, \tau)\} + i \text{Im}\{A(z, \tau)\} = A_R + iA_I$ to power $P(z, \tau) = |A(z, \tau)|^2$ and back again. This is no easy process to maintain in space and time because the phase information of the complex amplitude can be lost when transformed to the power. The following theory is customized to the simulation algorithms to maintain the complex information of the amplitude as it gets amplified.

Recall that the PT block in section 4.1 (and also the SSFM algorithm in Section 2.6) splits up the optical fiber into a discrete set of steps each with length dz and the input power to one of those sections comes in from the left boundary, gets amplified (if the fiber is active) and exits at the right boundary (or junction) as the incoming signal to the next section. Let us Choose one of these sections, say $i-1$ and suppose that the incoming amplitude and power $A_{i-1}(\tau)$ and $P_{i-1}(\tau)$ respectively are given. The following algorithm is designed to keep track of the incoming amplitude while first finding out the amplification of the input power. This is calculated using the standard algorithm

discussed in section 3.9. The simulator then back-tracks the step and similarly amplifies the amplitude function to the next section using the power gain information.

We need to simulate $A \rightarrow A + \delta A$ through any section. Knowing the value of A , the task is to solve for $\delta A = \text{Re}\{\delta A\} + i \text{Im}\{\delta A\}$. The solution is given by Equation 4-4.

The proof is as follows:

First, the Taylor expression for the power as it propagates from position z to $z + dz$ is defined to second order, after which the equation is re-arranged to the following:

$$\frac{P(z + dz) - P(z)}{dz} = \frac{dP}{dz} + \frac{1}{2} \frac{d^2 P}{dz^2} dz + \dots \quad 4-1$$

Similarly, given the gain coefficient g , and complex amplitude A , the power propagation equation has the alternative expression (with amplitude normalization in mind):

$$\frac{dP}{dz} = gP = g|A|^2 \quad 4-2$$

The first and second spatial differentiations of the power are

$$\frac{dP}{dz} = \frac{dAA^*}{dz} = 2 \text{Re} \left(A \frac{dA^*}{dz} \right) \quad \frac{d^2 P}{dz^2} = 2 \left| \frac{dA}{dz} \right|^2 + 2 \text{Re} \left(A \frac{d^2 A^*}{dz^2} \right)$$

Note that this is not a complex valued differentiation as dz is real valued, and therefore the Cauchy-Riemann conditions [55] are not needed for validation. Using the right side of Equation 4-2 to first order, one may calculate:

$$\begin{aligned}\frac{g|A|^2}{2} &= \operatorname{Re}\left(A \frac{dA^*}{dz}\right) \\ \therefore 0 &= \operatorname{Re}\left(-\frac{g|A|^2}{2} + A \frac{dA^*}{dz}\right) \quad 4-3 \\ \therefore 0 &= -\frac{g|A|^2}{2} + \left(A_R \frac{dA_R}{dz} + A_I \frac{dA_I}{dz}\right)\end{aligned}$$

The third expression in the above caption has infinite solutions because the complex amplitude can approach the same solution from any direction on the complex plane. With that in mind, an assumption can be made to achieve a particular solution. The standard gain and ASE algorithm states that the power is amplified without any dependence on the phase of the complex amplitude. It is assumed then that the amplification of the amplitude be independent of the relative relationships between the real and imaginary components. In other words, the rate of change of the real component depends only on how much real amplitude already exists at the section input. The same concept is repeated for the imaginary component. Mathematically, this is expressed for some constant f :

$$\begin{aligned}\frac{dA_R}{dz} &= fA_R \\ \frac{dA_I}{dz} &= fA_I\end{aligned}$$

Equation 4-3 is used to solve for this constant with the result that $f = g/2$. After amplification, the new amplitude and power are expressed as follows:

$$A_{out} = A_{in} \left(1 + \frac{gdz}{2}\right) \quad 4-4$$

$$P_{out} = |A_{in}|^2 \left(1 + gdz + \frac{g^2 dz^2}{4}\right) \cong |A_{in}|^2 (1 + gdz) \text{ when } dz \rightarrow 0 \quad 4-5$$

In Equation 4-4, the input and output amplitudes to a particular section of the fiber is $A_{in} = A_R + iA_I$ and A_{out} . There is an error factor if the output power is set to the absolute square of the output amplitude, however it becomes insignificant for high spatial resolutions where the differential step approaches zero.

The results provided in this section were analyzed and tested for validity. Refer to section 6.5 for more details on the validation process after which it was concluded that the first order approximation is accurate enough for our purposes.

4.3 Inside the Black Box

In propagating from junction $i-1$ to i along the simulated fiber, two software components are executed in series starting with the standard gain and ASE algorithm and followed by the PT block as is illustrated in the block diagram below:

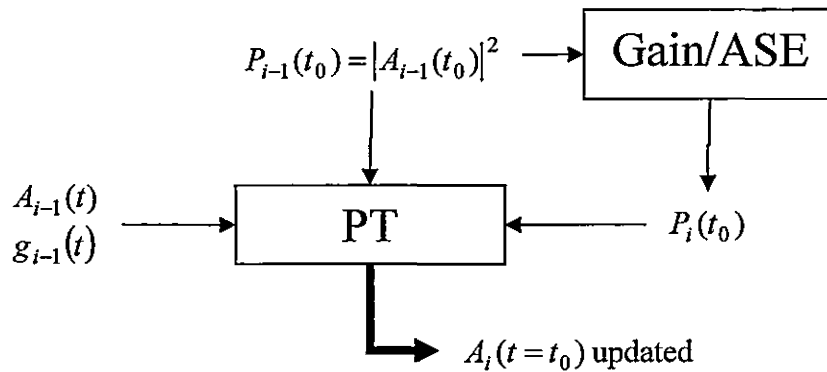


Figure 4-2 The standard gain algorithm is used to calculate the current gain coefficient, a procedure performed once between PT block operations for every section and time step. This updates the gain coefficient array only for the current time step.

The inputs are the incoming instantaneous power $P_{i-1}(t)$, complex amplitude $A_{i-1}(t)$ and the corresponding gain coefficients (for all of the time steps) $g_{i-1}(t)$. The gain coefficients have values belonging to the amplification of the complex amplitude of the

préviously simulated pulse for time steps $t > t_0$ where the current time step is defined to be t_0 . The resulting outputs are the amplified complex amplitude $A_i(t)$ exiting at junction i and the gain coefficients for the current section $g_{i-1}(t)$ (both of which are updated for the current time step $t = t_0$).

A GVD operation is non-causal as the operation requires pulse samples for all the defined time-steps. Therefore, future values of gain coefficients are necessary - hence the borrowing of future gain coefficients from the pulse immediately preceding the current one being solved in the simulation. Assuming these values do not differ significantly from what they should be valued at, all the internal and output powers are expected to converge. Whether this is a valid assumption is left as a verification of the laboratory experiment. The ASE calculation is assumed to be mutually exclusive from those of the GVD and SPM, and therefore these ASE powers (already calculated with the standard gain algorithm in Figure 4-2) are propagated along side the signal power but not through the PT block. In addition, since attenuation α has also been calculated in the formulation of $g_{i-1}(t)$ - effectively, only the *net* gain, GVD and SPM are calculated for the pulse itself at the signal wavelength bin inside the PT block.

The internal logic procedure of the PT block is illustrated in Figure 4-3. First the P2A algorithm is used to attain the most recent up to date gain coefficient at the current time step $t = t_0$. This is set within the gain coefficient array $g_{i-1}(t)$ that still contains the gain coefficients of the previous pulse for time steps $t > t_0$. This array and the complex amplitude $A_{i-1}(t)$ is sent into the GGS software block (to solve for Gain, GVD and SPM

effects) illustrated in Figure 4-4. The resultant data output is a pulse that has traveled from junction $i - 1$ to i that has been simultaneously processed for gain, GVD and SPM.

The same procedure essentially repeats itself in the next section. However, that cannot be executed until all the powers are propagated in the current one. This concept is actually the bottle neck of the entire operation. If there is a way to parallelize the MCP algorithm further, it would greatly increase the computation time of the simulation.

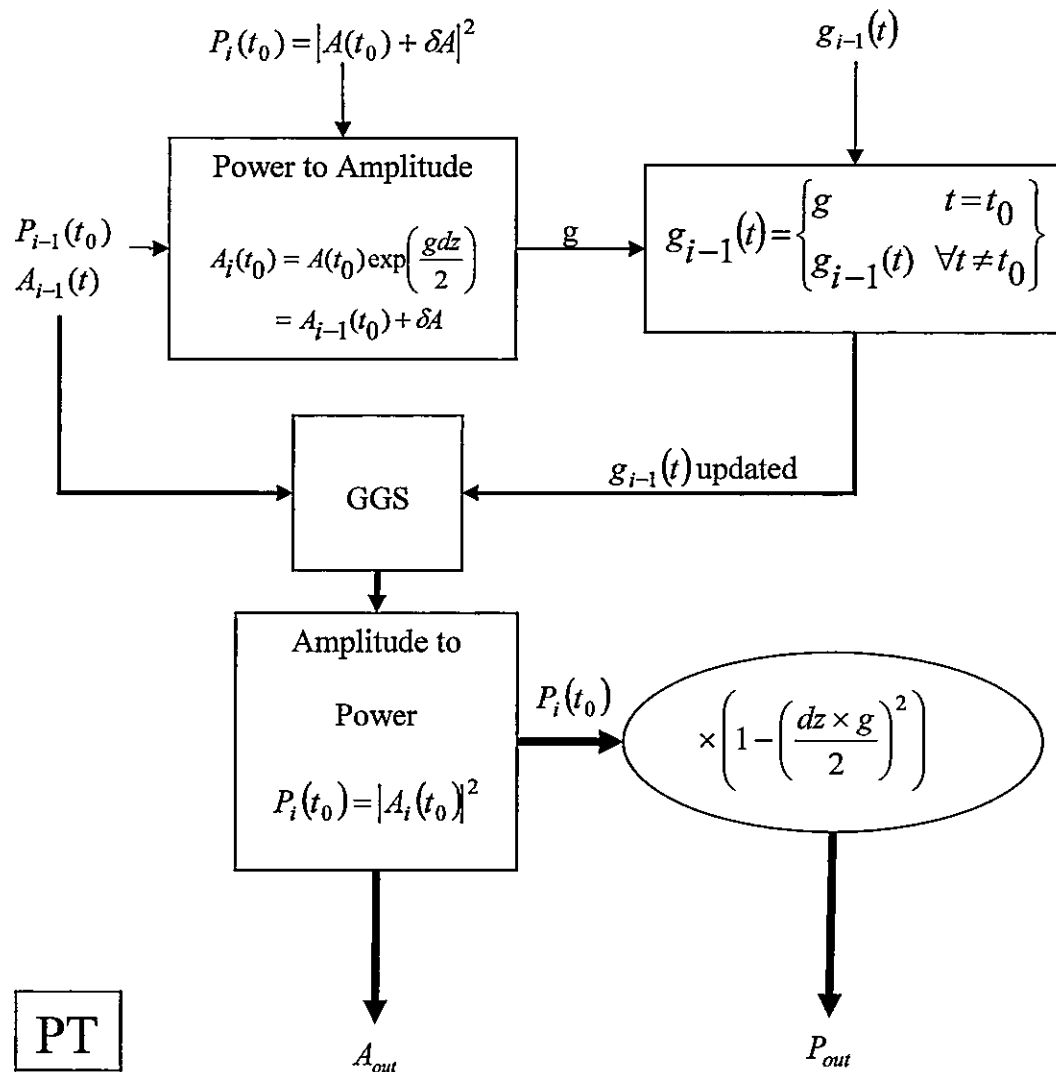


Figure 4-3 The block diagram of the passive transform algorithm. First the gain is updated for the current time step t_0 , and the passive operations are performed using the GGS block (illustrated in Figure 4-4) using this information as well as the previous pulse characteristics for those time steps which have not yet been attained. The correction factor performed on the output power $1 - (0.5 \times dz \times g)^2$ is applied according to Equation 4-5 when dz is not assumed to be a very small step.

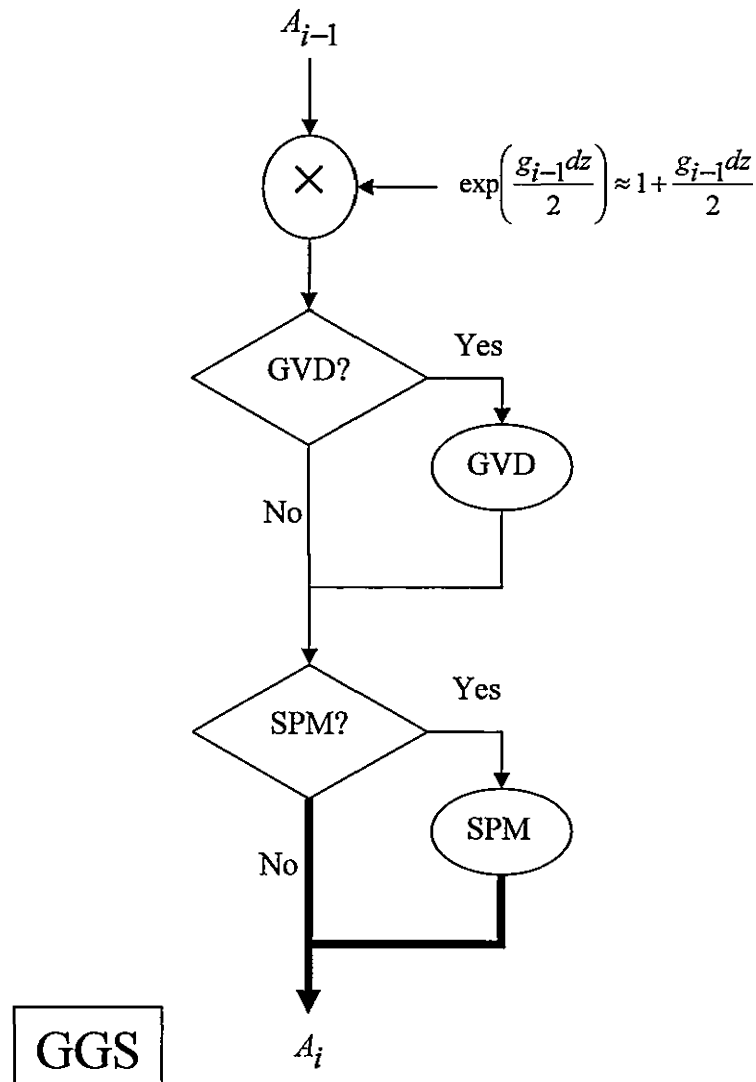


Figure 4-4 The GGS block performs the actual gain, GVD and SPM operations onto the pulse. The entire complex amplitude pulse and gain coefficient array are sent as input. The resultant amplitude is used as input for the next section of the fiber.

During simulation initialization, the gain coefficient arrays for all the sections $i=0$ to $NSTEPS - 2$ get initialized to zero for all the pulse time steps. There is no way of knowing what the gain is until the simulation goes through at least one pulse iteration of the standard gain and ASE algorithm. By doing so, the gain coefficient arrays are set to gain values which are to be used in the active and passive calculations. Hence, for the simulation of the very first pulse, the GVD and SPM components are off, however the

P2A algorithm is still on so that complex amplitude is also recorded. Then, for all the following pulse iterations, the passive bocks are turned on, and the operations are expected to converge after a number of pulses. How many pulses it really takes depends on the details of the calculation procedure and it is left as future work to predict how many pulses would be required for system convergence.

5 Theoretical Unknowns and Limitations

Many simulation conditions have to be assumed and/or approximated due to the unknowns discussed in this Chapter. The following should not be considered a complete account. However, those topics discussed are considered as the most significant issues.

5.1 Input Chirp

The input pulse in the MOPA experiment contains linear and higher ordered chirp. Formally, input chirp is defined as an additional complex phase to the input pulse. The full electric field in Equation 3-2 can be generalized even further to include the phase function ϕ :

$$\vec{E}(x_{\perp}, z, t) = \hat{e}U \left(x_{\perp}, \omega_0 + i \frac{\partial}{\partial \tau} \right) A(z, \tau) \exp[i(\beta_0 z + \phi(\tau))] + (*)$$

where

5-1

$$\phi(\tau) = -\omega_0 \tau + \left(\frac{-C}{T_0^2} \right) \frac{\tau^2}{2!} + D \frac{\tau^3}{3!} + E \frac{\tau^4}{4!} + \dots$$

The phase function $\phi(\tau)$ has higher order components. The derivative of $\phi(\tau)$ indicates how the frequency changes in time for the operating wavelength of the instantaneous optical pulse,

$$\omega(\tau) = -\frac{d\phi(\tau)}{d\tau} = \omega_0 + \left[\left(\frac{C}{T_0^2} \right) \tau - D \frac{\tau^2}{2!} - E \frac{\tau^3}{3!} + \dots \right]$$

5-2

If a pulse has no chirp (i.e. $C = D = E = \dots = 0$), then the operating wavelength is uniform throughout time ($\omega(\tau) = \omega_0$). However, if a linear chirp exists (i.e. $C \neq 0, D = E = \dots = 0$), then the full EM field has an additional higher-order phase.

The instantaneous frequency $\omega(\tau)$ was discussed earlier in Section 2.6. An input pulse with linear chirp does not have a uniform (operating) frequency ω_0 throughout time. If the input chirp is positive $C > 0$, then according to Equation 5-2, the instantaneous frequency increases linearly from the leading to the trailing edges of the pulse. In optics, this is usually referred to as blue-chirp [52]. In cosmology, this is an event referred to as the red-shift. The opposite occurs for a negative chirp condition $C < 0$. In this case, the pulse has a red-chirp (or blue-shifted).

To simplify the chirp expressions, one can assimilate all higher order phase components into the amplitude function in Equation 5-1. Therefore, an input Gaussian pulse amplitude with linear chirp is expressed as:

$$A(0, \tau) = \sqrt{P_0} \exp\left[-\frac{(1+iC)T^2}{2T_0^2}\right] \quad 5-3$$

There are ways to estimate ultra-short temporal pulse chirp such as utilizing an interferometric autocorrelation [53][54] or second harmonic frequency resolved optical gating (SH-FROG) [78]. Note that these methods utilize a fitting algorithm which still has some finite uncertainty. This effort however is left for future work. Currently, the only way of finding out the temporal chirp is to infer some chirp conditions until the simulations verify experiment (Section 6.6.3).

5.2 Pulse Shape

The temporal pulse shape output from the single-quantum-well passively mode-locked semi-conductor diode laser used in the laboratory experiment is not bell shaped. In the case of this two-section [69] laser diode composed of gain and saturable absorber sections, the pulse is almost certainly asymmetrical. The leading edge of the pulse is steeper than the trailing edge owing to the effect of the saturable absorber [10]. Refer to [72] for a comprehensive discussion of saturable absorption on multi-section diodes and their effect on pulse shape.

To be able to control the seed pulse shape before it is coupled into the fiber amplifier is an important component of a MOPA design. Perhaps it would be beneficial to develop a complementary diode laser simulator which synthesizes seed pulses that are more representative of that which is output from the diode laser used in experiment. A difference in seed pulse shape in the time domain can have diverse effects on the spectrum, and this could lead to different input chirp designs as discussed at the end of Chapter 6.

The development of a diode laser simulator is left as a future endeavor.

5.3 High Frequency Errors

For this simulation, so many intermediate steps are programmed that any incorrect or highly volatile algorithm is expected to destabilize the calculation results significantly. For example, Figure 5-1 illustrates a case where the numerical amplification of a pulse can cause aliasing. The first column in the figure shows the incoming noiseless pulse before it gets amplified at the beginning of a particular section in the fiber. The middle

column illustrates power amplification for this pulse in the current time step. The final column shows the amplification for the other time-steps where a power increase for previous time steps for the current pulse has already been calculated and power amplification of future time steps is taken from amplification characteristics of a previous propagating pulse.

If there is a significant discontinuity (as illustrated in Figure 5-1 2nd row), these high frequency components cause significant aliasing if an FFT is performed on the amplitude. This is certainly the case if GVD operations are in effect.

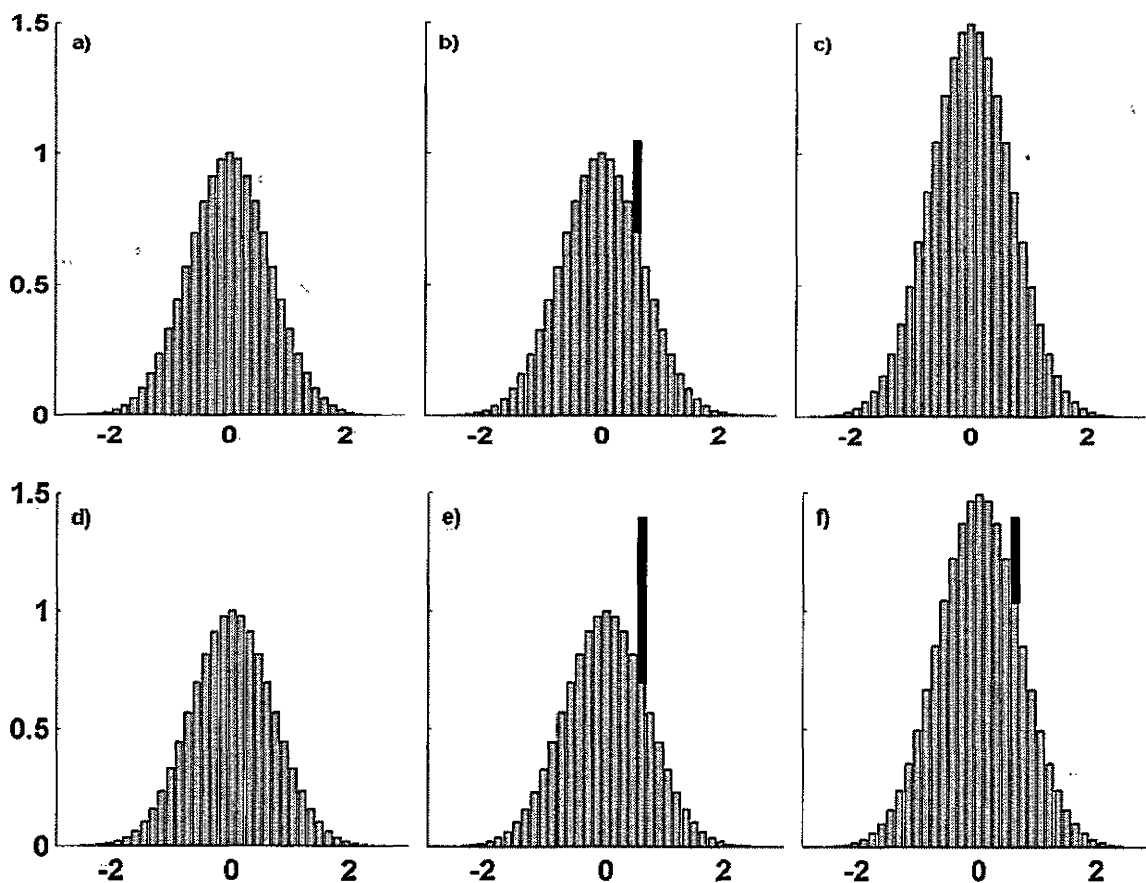


Figure 5-1 The first row shows an example of normal pulse amplification (from left to right in a particular section) during simulation. The second row shows how an abnormal amplification event can result in an amplified pulse with a spike for the current time-step that adds high frequency components not natural to the pulse and cause aliasing if and when the pulse in subfigure (f) is passed into an FFT. The spike power bar in (f) shows how qualitatively, the amount of amplified power can cause aliasing.

For details on this signal processing issue, refer to Haykin's text [7]. If aliasing is in fact significant, then the digital signal gets corrupted, information is lost, and ultimately a non-realistic simulation results.

5.4 Unsaturable Pump Absorption

Ideally, a high enough launched pump power will cause 50% inversion due to the pump power for the ytterbium dopant population causing fiber transparency at the pump wavelength and thus zero background losses. However there are several physical interactions in the fiber such as ESA, cross-relaxation, and quenching of ytterbium ions which change the ideal saturated pump absorption condition to the unsaturated one. More specifically, the absorption [m^{-1}] for selected fiber length versus launched pump power does not go down to zero, but levels off to some non-zero absorption regardless of how high the pump power is set.

A minority in a pool of ytterbium dopants have a faster relaxation process compared to the remaining ions in an YDFA. These dopants are called quenched ions and because they relax quickly, absorption of pump photons will re-occur many times in comparison to regular dopants. The inversion of dopant populations can not be 50-50 as a result and therefore results in unsaturable absorption. In contrast, at least theoretically, the system can still be fully saturated provided the pump power is high enough.

In his paper, Yelen discusses an attempt to account for cross-relaxation and ESA contributions to the unsaturable absorption [22]. However, it turned out that the theoretical values necessary to achieve numerical results that satisfy experimental results were not realistic when compared to reported values in previous literature. The

conclusion was that lifetime quenching of ytterbium ions is the dominant cause of the unsaturable absorption for YDFAs. Some useful values from Yelen's work for simulation of an unsaturable Ytterbium doped fiber amplifier are tabulated below:

Table 5-1 Parameters for lifetime quenching of ytterbium [22].

Parameter	Value
Pump Wavelength	978 – 980 nm
Yb Concentration	$34 \times 10^{25} \text{ m}^{-3}$
Yb $^2F_{5/2}$ life-time	2 ms
Yb $^2F_{5/2}$ quenched life-time	1 μ s
$\frac{\text{Quenched Yb}}{\text{Total Yb}}$	0.11

For the YDFA, quenching at 976 nm can be significant [45][46]. Although our pumping wavelength used in the ultra-fast laser laboratory experiment is approximately 975 nm, we are not sure if our fiber exhibits unsaturable absorption, as it does not happen in all fibers. However, it can be that the output signal power simulated without this quenching process taken into account will result in higher values than should otherwise be. A future version of the simulator will divide its dopant concentrations into two parts representing the quenched and un-quenched populations just like it is done in Yelen's simulations, but only for those fibers that are certain to cause unsaturable absorption. This should correct the quantum efficiency of such systems for more realistic results, and in addition is expected to lower the slope efficiency as some of the pump power can be unabsorbed.

5.5 Pump Spectrum

The assumed condition of pump power being monochromatic is an oversimplification as there is always some bandwidth present with the pump laser beam. In addition, the spectrum has a highly structured bandwidth as illustrated in Figure 5-2 that shows experimental pump spectral measurements taken by my colleague Andrew Budz from the Lumics pump diode used in the MOPA system. Some characteristics of this pump include maximum operating power of 4 W, peak pump wavelength 974.6 nm and a FWHM of 3.4 nm.

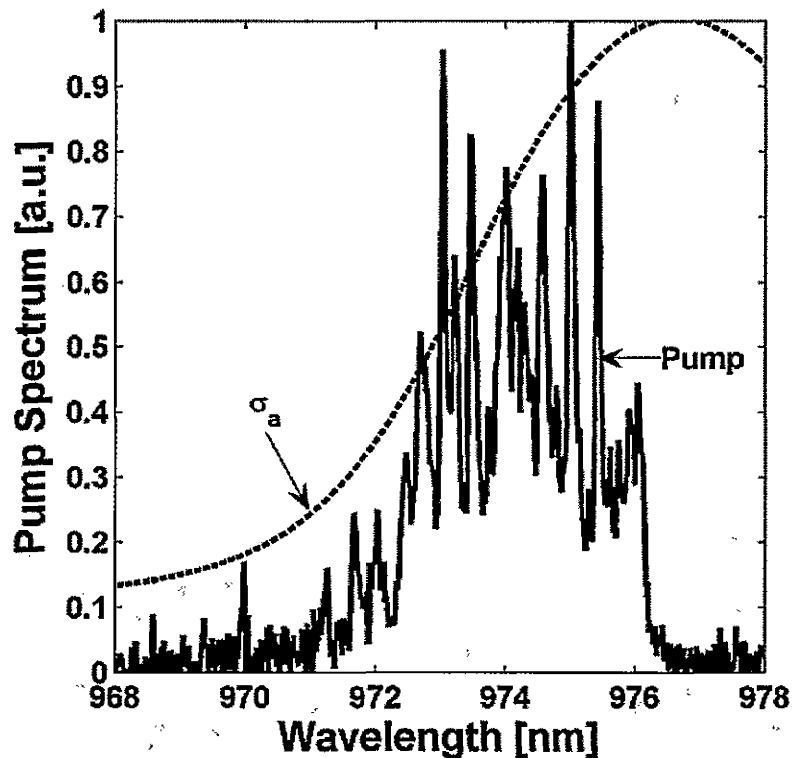


Figure 5-2 Pump power spectrum implies simulation inaccuracy if the pump beam is taken to be monochromatic, as the superimposed absorption cross-section (dashed line) is not constant throughout the bandwidth of the pump spectrum.

The calculation of pump power propagation goes through exactly the same numerical computations as the signal power. To save on computation time and memory consumption, the pump power was kept at one wavelength bin centered at 975 nm. For

better accuracy, one can calculate the weighted average peak operating wavelength of the pump power by correlating with the absorption cross-section which results in ~ 974 nm, although this has not been considered in the simulations reported here. One can also use the weighted center of the pump bandwidth for a peak wavelength. More details on how the system would be affected by an increase in wavelength bins are discussed in the following section.

The pump bandwidth may have a significant effect in the simulator since the pump absorption peak is so narrow at 975nm. The fact that the real pump bandwidth is ~ 3 -4 nm means that an effective absorption cross-section is somewhat smaller.

5.6 Wavelength Bin Resolution

Each power propagation (differential) equation belongs to a distinct wavelength bin as discussed in Section 3.9. Every additional wavelength bin requires a differential equation to be implemented into the simulation. As discussed earlier, there is only one wavelength considered for the pump power, and hence only one differential equation. The signal (which includes the ASE power) can have multiple wavelength bins. It is clear that with every additional differential equation will increase the processing time as well as the memory requirements of the system. During development, wavelength bin numbers from 5 to 40 bins were used (Figure 5-3). It turns out that selecting more than 30 bins does not improve the accuracy significantly (Figure 5-4). A balance of computational requirements and accuracy had to be made.

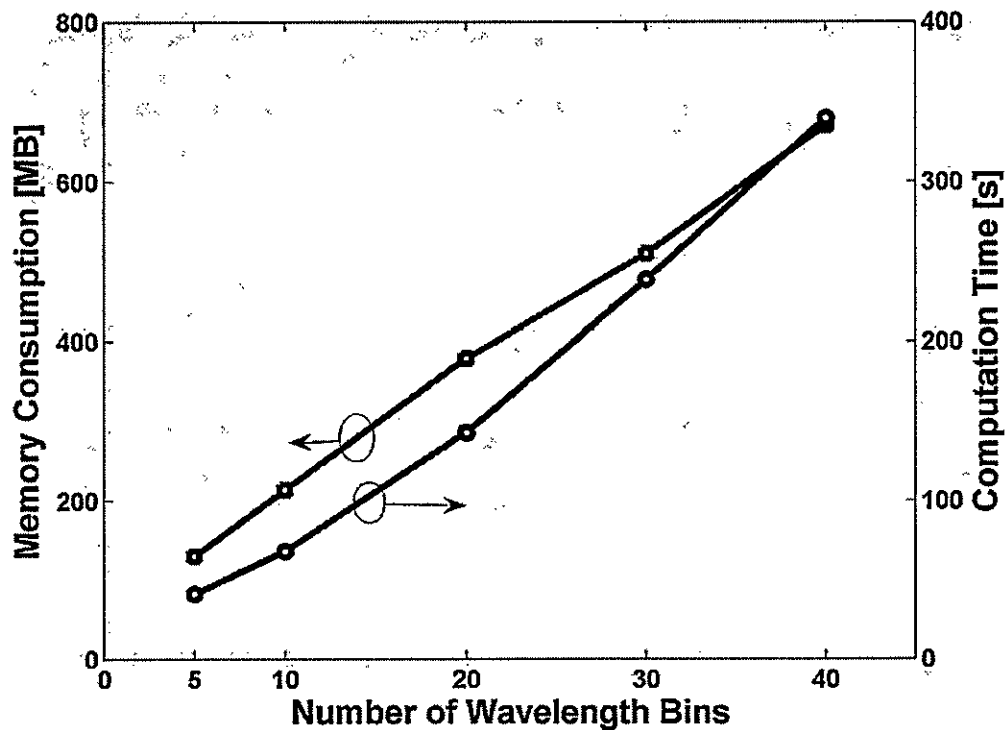


Figure 5-3 Memory Consumption (left) in megabytes and Computation time (right) measured for identical pulsed simulations for a selected number of wavelength bins.

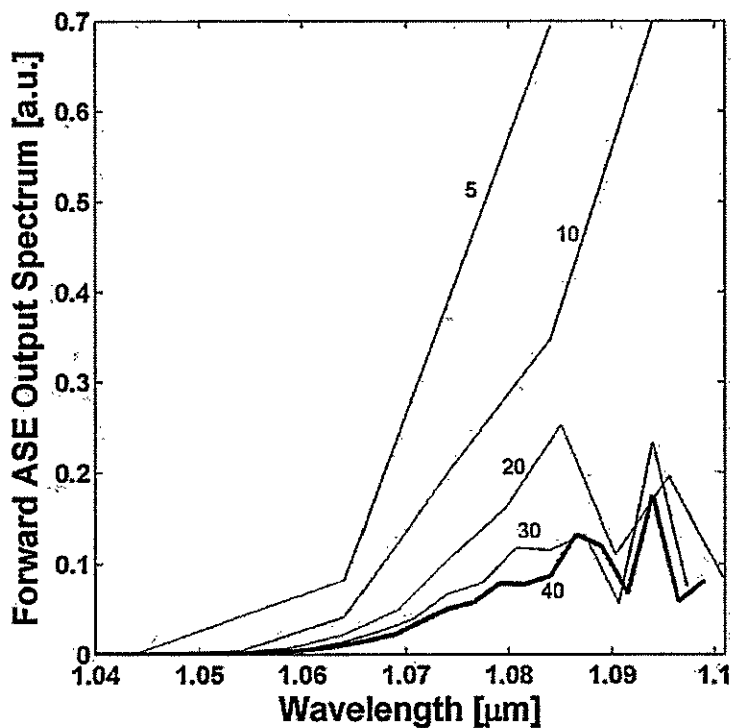


Figure 5-4 The output ASE spectrum for a selected number of bins. Reasonable convergence happens for bin numbers greater than 30 bins.

5.7 Non-uniform Spatial Resolution in the SSFM

The simulation algorithm incorporating active and passive effects simultaneously (Chapters 4 and 6) has a split-step approach very similar to the SSFM algorithm (Section 2.6). Both approaches have assumed a uniform spatial step from one section of the fiber to the next. As we know, it is in many cases necessary to have very small spatial steps to resolve some interactions that cannot be observed with lower discretization. Reducing the step size dramatically increases the processing time on an exponential scale, and as reported by Sinkin, it turns out that this is the least efficient approach compared with all other methods that modify the step sizes in some fashion [27].

In general, the efficiency of the SSFM is dependent on the time-domain and frequency-domain resolutions. Depending on how one decides to distribute the resolution throughout the fiber, many detrimental artifacts can arise. Bosco reported that if the spatial-step is kept constant, it is not only least efficient, but causes an overestimated calculation of four-wave mixing [3][26], and that to suppress this effect, the step size h_i for the i^{th} step is defined logarithmically:

$$h_i = -\frac{1}{2\alpha} \ln \left[\frac{1 - i\sigma}{1 - (i-1)\sigma} \right] \quad 5-4$$

where α is the fiber attenuation, and $\sigma = [1 - \exp(-2\alpha L)]/N\text{STEPS}$. Other methods are also proposed by Sinkin, and all are specialized to a particular operating configuration, such as a multiple-channel communication fiber.

In future work, four-wave-mixing is to be implemented into the simulator for high-power experiments. It is important to keep the logarithmic spatial-step length of

Equation 5-4 in mind for optimizing results and minimizing unwanted numerical artifacts.

5.8 Round off Errors

There are countless areas where round-off errors accumulate in the simulation process. Most of these are due to the fact that computer memory cannot store data on a continuum, but instead keep discrete data selections each with a limited number of decimal places.

In the development process, there were difficulties with the accuracy of the fast Fourier transform (FFT). In signal processing, when an analytical function (or signal) is operated on by the FFT and that result is operated on by the inverse fast Fourier transform (IFFT), the output must be the original analytical function provided that the sampling frequency is at least twice the Nyquist frequency of the signal:

$$h(t) = \text{IFFT}(\text{FFT}(h(t))) \quad 5-5$$

Unfortunately, we are not dealing with analytical functions and floating-point arithmetic is not exact enough. Due to the round-off errors, every execution of Equation 5-5 on the amplitude results in a slightly different magnitude than what should actually be. The difference in magnitude is very small ($\sim 10^{-15}$ W) for any part of the (Gaussian) amplitude. This error can be significant as it can be propagated on and on in the passive calculations of the simulator just like the pulse power is propagated along the fiber in the SSFM algorithm.

When the PBC variable (section 2.2.2) is increased, the amplitude of the Gaussian tails decreases accordingly at the ends. So small are these amplitudes that they are

comparable and in most cases less than the round-off noise generated by the FFT and IFFT algorithms. Therefore, one must assume that there is round off error every time the signal is operated on by the FFT or IFFT:

$$h(t) = \text{IFFT}(\text{FFT}(h(t))) + e(t) \quad 5-6$$

where $e(t)$ is the round-off error imposed by the computer system. The solution to this problem was to increase the number of pulse samples by a factor of two until round-off errors were insignificant (within the error of the double precision variable defined in C++). Alternatively, one can keep the PBC value relatively low causing the tails of the input Gaussian pulse to be at least an order of magnitude greater than the round-off errors.

5.9 Higher Order Dispersion

The expansion of the propagation constant β (formally defined in Section 2.3.1) to the third order component of the dispersion operator (Equation 2-21) should be made if the pulses in question are ultrashort.

$$-\frac{\beta'''(\omega_0)}{3!} \frac{\partial^3}{\partial t^3} \quad 5-7$$

This third order dispersion can become dominant when GVD effects are minimal in comparison. Such conditions arise when the peak pulse wavelength is at, or very close to the zero-dispersion wavelength λ_D such that the second order component $\beta''(\omega_0) \approx 0$ as described by Agrawal [3]. Also, it can happen for non-zero values of $\beta''(\omega_0)$. It turns out that for pulses with widths less than or equal to 100 femtoseconds, third order dispersion has a significant effect on the pulse shape, and its magnitude is high enough

that $\beta''(\omega_0)$ values can be as high as $1 \text{ ps}^2/\text{km}$. The observable effect from third-order dispersion on a Gaussian pulse is an asymmetric shaping with oscillations at one of the tails [3].

Picosecond pulses require $\beta''(\omega_0) < 0.001 \text{ ps}^2/\text{km}$ for third order dispersion to become significant. The β'' value employed in the simulations has been set to $15 \text{ ps}^2/\text{km}$ that corresponds to a peak wavelength of 1075 nm . Therefore one may conclude that GVD dominates the dispersion procedure. It was assumed, for simplicity of the simulation project, to zero the value of $\beta'''(\omega_0)$. In future work, at least the third order dispersion will be considered for modeling completeness.

5.10 Stimulated Raman Scattering

All materials at room temperature have excited vibrational energy levels whose electric-dipole-like phonon-photon interaction with the incident pump beam causes a downshift in the optical frequency. The resulting Stokes wave generated spontaneously is generally negligible, can travel in all directions, and depletes the signal energy whose wavelength is defined as λ_s . However, this can lead to undesirable events.

The Stokes waves can be further amplified as they propagate through the fiber (in both directions) via stimulated emission given that there is a non-zero cross-section at the Stokes wavelength. This phenomenon is called stimulated Raman scattering (SRS) and can be prevented in a number of ways. However, the first approach is usually to limit the peak signal power below the SRS threshold. The threshold (or critical) peak signal power P_0^{th} for SRS has been defined by Agrawal [3] for an ultrashort pulse:

$$P_0^{th} \cong 16 \times 2 \times \left(\frac{A_{eff}}{g_R \times \left(\frac{1 \mu m}{\lambda_s} \right) \times L_{eff}} \right) \quad 5-8$$

where the effective area A_{eff} is given by Equation 2-7, the effective interaction length is defined by $L_{eff} = \text{FWHM}/|d|$ where $|d| = \left| \nu_{gs}^{-1} - \nu_{gSTOKES}^{-1} \right|$ with ν_{gs} and $\nu_{gSTOKES}$ being the pump and stokes group velocities respectively, g_R is the Raman gain spectrum with respect to the frequency shift $\omega_{STOKES} - \omega_p$ (in Hz) at a pump wavelength $\lambda_p = 1 \mu m$ (plotted in Figure 8.1 in Agrawal's text for silica fibers), and the factor of 2 is included if the fiber is not polarization maintaining (PM). The peak of the Raman gain spectrum is approximately 1.0×10^{-13} m/W and is modified accordingly when $\lambda_s \neq 1 \mu m$.

Coupled amplitude equations for SRS are used to solve (after some approximations) for Equation 5-8 above [3]. These differential equations are beyond the scope of this report as they have not been implemented into the simulator. This is because the ultra-fast laser laboratory amplified signal peak power is far below the threshold necessary for any significant SRS effects in the YDFA. A quick calculation (using Table 6-6 simulation values) shows that the minimum threshold pump power required for any significant SRS is over 5.0 kW for a non-PM fiber. Since we have at most ~320 W peak signal power, SRS effects are assumed to be insignificant.

For any high-power experiments, SRS cannot be disregarded so easily, and so it is left as a future exercise to implement the Raman effect into the simulator. The coupled-amplitude equations are provided by several texts [1][2][3] and can be implemented into

the simulation in the same formalism as the gain and ASE implementation. This has already been accomplished by Wang [67] for the standard gain and ASE model.

5.11 Stimulated Brillouin Scattering

The interaction of signal photons with acoustical phonons that travel through the material as pressure waves is called stimulated Brillouin scattering (SBS). Stokes waves can be generated by SBS; however they travel in the opposite direction from that of the signal power. The Brillouin gain spectrum g_B has a very narrow bandwidth of approximately $\Delta\nu_B=10$ MHz and has a peak value at about 6×10^{-11} m/W for a signal with narrow-bandwidth. If the signal laser has a larger bandwidth $\Delta\nu_s$ than the Brillouin gain spectrum, then the gain dramatically decreases by a factor $\Delta\nu_s / \Delta\nu_B$. Our signal seed has a bandwidth of approximately 1.43 THz (where the FWHM is taken to be 5.5 nm from Figure 6-34). Therefore, the signal is far too broad in the frequency domain for any significant observable SBS effects.

For high-power systems with ultra-short bandwidth signals, there is a threshold equation very similar to Equation 5-8 that can be utilized to see if SBS is a significant issue in Ytterbium fiber amplification. Refer to reference [3] for fundamental theories and [71] for details on a numerical implementation of SBS. A cw threshold power is also available in Keiser's text [86].

5.12 Polarization Effects

The fibers used in the simulation are not polarization maintaining and therefore one must consider random polarization effects on the signal and the dynamic dopant

populations. The linearly polarized input field gets scrambled as it travels down a fiber that is not polarization maintaining. The intensity dependent refractive index $\delta n = n_2 |A|^2$, introduced for SPM in chapter 3, is defined for a linearly polarized field, and must be modified for the random polarization conditions. The correction factor $5/6$ has been suggested by Stolen and Lin [23]. This is derived from the fact that the intensity dependent refractive index for circular polarization is approximately related to the linear version by $\delta n_{circular} = (2/3)\delta n_{linear}$. A simple average intensity dependent refractive index is then calculated:

$$\begin{aligned}\delta n_{avg} &= \frac{(1 + 2/3)\delta n_{linear}}{2} \\ &= \frac{5}{6} n_2 |A|^2\end{aligned}\tag{5-9}$$

5.13 Numerical Inaccuracies of the SPM Model

In section 2.6, the nonlinear operation for the SSFM method is set constant for every propagation step. In reality, the nonlinear operator \hat{N} is spatially dependent because the amplitude function (with which this operator is defined) is also a function of the z dimension:

$$\hat{N} = i\gamma |A|^2 = i\gamma |A(z)|^2\tag{5-10}$$

This z -dependence has not yet been taken into account in the simulation. The main reason for this was due to the anticipation that it would take too much time to numerically solve for results that would not be significantly different from those that were simulated without the nonlinear z -dependence: Assuming that the section lengths are kept minimal.

This will however be implemented in future work, and the following shows how this will be done.

The nonlinear operator in the execution of $\exp(h\hat{N})$ for the SSFM should be modified analytically by an integral as revealed in Potasek's article [66]:

$$\exp\left(\int_z^{z+h} N(z') dz'\right) \approx [N(z) + N(z+h)] \frac{h}{2} \quad 5-11$$

The right side is a Trapezoidal rule approximation which should be implemented iteratively. On the first iteration, amplitude values for both locations are set to the known value at location z . Once the amplitude is known at location $z+h$, the second iteration updates the equation accordingly. Potasek found that two such iterations were enough.

5.14 Amplified Spontaneous Emission Equation

To summarize, the ASE Equation 3-14 is a seed source for stimulated emission of ASE in a 1D Fabry-Perot cavity. This waveguide does not have the same geometry as the cylindrical fiber core cavity, and as such, one would not expect to get accurate ASE power results from this equation. However, even though this model is designed for an entirely different waveguide structure, many use it in modeling YDFAs with reasonable results [20][32][67][74][75].

Unfortunately, due to time limitations, I was unable to try to develop an expression that would better fit the geometry of the fiber core. In any case, I had to implement Equation 3-14 to verify the results of other articles. Future work will certainly include the modeling of ASE in the YDFA.

6 Results and Verification

The following is a discussion of the results obtained and techniques used by the simulator for modeling the Ytterbium fiber component of the hybrid MOPA experiment running in the laboratory. The applied theory is complex and therefore experimentation via simulation of real cases is a must to verify that the software is working correctly.

At the end of Chapter 3, a standard model was introduced for calculating the gain and ASE effects on a propagating pulse in a doped optical fiber amplifier. This approach cannot take into account complex (or phase) information of the pulse. Therefore the model had to be modified to incorporate the complex amplitude. This was one of the accomplishments of this thesis, and for convenience, the new algorithm will be called the modified complex power method or MCP. To the best of my knowledge, this method has not been developed in previous works.

The results in this chapter concentrate on selected physical interactions that in my opinion are the most difficult to simulate simultaneously. These are gain, ASE, GVD and SPM. The addition of higher order dispersive effects, SRS, SBS, and other nonlinear effects is not significant in the context of proof of concept. That is, the implementation of the extra effects is trivial provided the simulator is capable of already simulating GVD and SPM accurately. The following sections on verification and results should be a sufficient baseline for future work.

There are many ways to verify that the passive components of the software are running correctly. Throughout the development phase, most of the passive results were compared to simulations by Agrawal [3]. For verification purposes, the symmetric split-step Fourier method has also been coded into MATLAB, a far less efficient platform than C++, but easily programmable.

6.1 GVD and Input Chirp Verification

We begin with the calculation of GVD effects on a Gaussian pulse whose input RMS half-width T_0 at $z = 0$, changes on propagation according to the following equation [3]:

$$A(0, \tau) = \exp\left(\frac{-\tau^2}{2T_0^2}\right) \rightarrow A(z, \tau) = \frac{T_0}{T_1} \exp\left(\frac{-\tau^2}{2T_1^2}\right) \quad 6-1$$

The RMS width varies as a function of propagation distance, and its magnitude is formally defined as:

$$|T_1| = T_0 \left[1 + (z/L_D)^2\right]^{\frac{1}{2}}. \quad 6-2$$

The dispersion length $L_D = T_0^2/|\beta_2|$ is one of two constants used to validate whether or not soliton conditions (discussed later on) are in effect. The GVD on an input Gaussian pulse was calculated by the MCP algorithm and the results are illustrated in Figure 6-1 for selected lengths down the fiber. These results were compared to SSFM results by Agrawal [3] for identical operating conditions (with SPM turned off). The comparison showed that the results were identical. From that figure, it is evident that GVD broadening effects are significant for fiber cuts longer than the dispersion length.

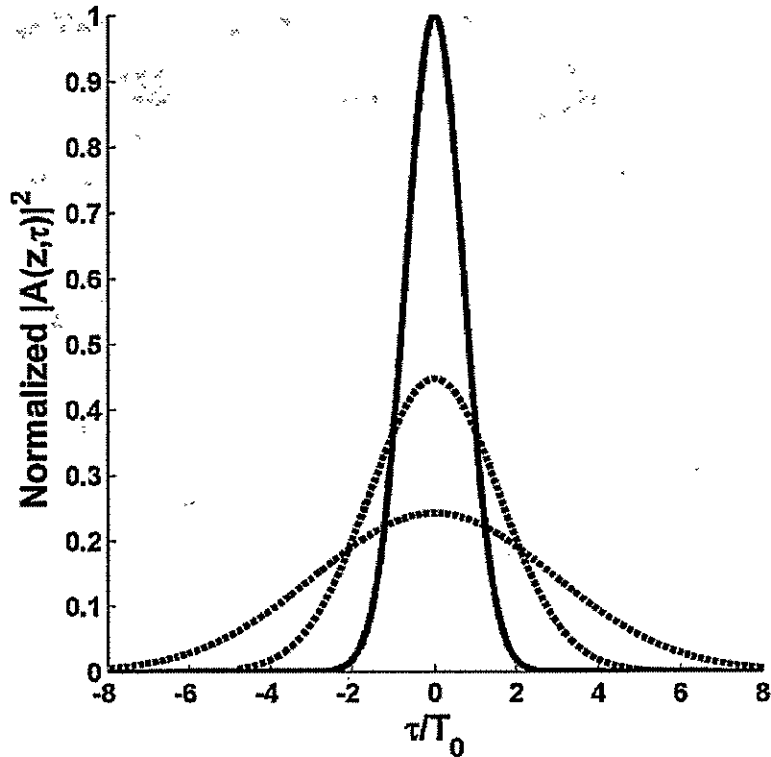


Figure 6-1 MCP simulation shows normalized pulse amplitude at $z=0$, $2L_D$ and $4L_D$ meters down the fiber. The pulse-width increases with distance due to the GVD effects.

Pulse broadening due to GVD varies differently depending on the choice of chirp added to the input pulse (as discussed in Section 5.1). Consider the linearly chirped input Gaussian pulse defined in Equation 5-3. Simulations for a selected set of linear chirp constants $C = 0, \pm 2$ have been performed that take GVD and input chirp into account. The results are now illustrated in Figure 6-2 and once again, are identical to SSFM output plots by Agrawal [3].

With input chirp C , the RMS broadening equation is modified after the pulse propagates a distance of z down the fiber [3]:

$$|T_1| = T_0 \left[\left(1 + \frac{Cz}{L_D} \right)^2 + \left(\frac{z}{L_D} \right)^2 \right]^{\frac{1}{2}} \quad 6-3$$

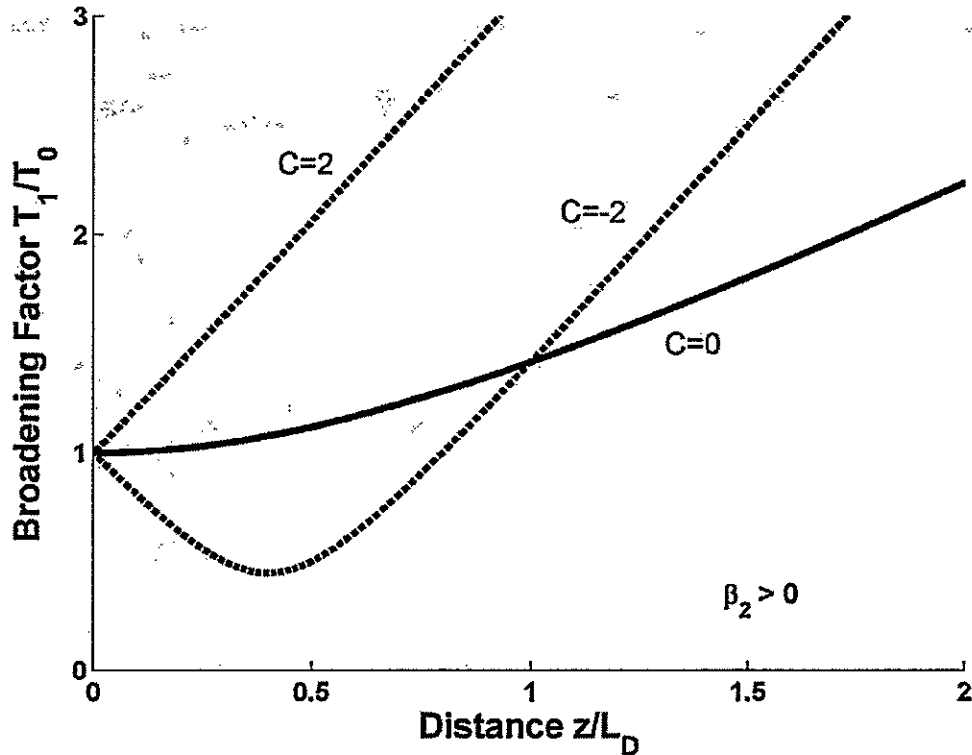


Figure 6-2 MCP simulation shows a Gaussian pulse broadening due to natural GVD effects over a distance for pulses with selected input chirps.

The normally dispersive operating conditions ($\beta_2 > 0$) and negative chirp ($C < 0$) are the cause of the dip in pulse-width for $C = -2$. The Gaussian pulse goes through a pulse compression stage ($T_1 < T_0$) in this region. After pulse propagation to some distance down the fiber, there is an inflection point and GVD becomes the dominant broadening factor. Note that similar pulse compression occurs for positively chirped input pulses if the operating conditions are in the anomalous-dispersion regime of the optical fiber ($\beta_2 < 0$). This is explained by first recalling that the GVD on a propagating pulse causes a red-shift. This phenomenon happens over time as the pulse travels down the fiber. If the pulse has negative input chirp, a narrowing effect occurs until GVD effects finally catch up and overpower the initial blue-shift.

6.2 SPM and Input Chirp Verification

Switching off all pulse-propagation effects except for SPM in the simulator infers the mathematical equivalent:

$$\frac{\partial A}{\partial z} = i\gamma |A|^2 A$$

Therefore the amplitude has a unique solution:

$$A(z, \tau) = A(0, \tau) \exp(i\gamma |A(0, \tau)|^2 z) \quad 6-4$$

The maximum phase shift ϕ_{\max} occurs where the peak power for a bell-shaped (amplitude normalized) pulse $|A(0,0)|^2 = P_0$ is at a maximum:

$$\phi_{\max} = \gamma P_0 z \quad 6-5$$

SPM effects can be visualized in the wavelength (or frequency) domain for selected locations down the fiber. Such plots are provided in Figure 6-3 from an MCP simulation and these are in excellent agreement with plotted calculations by Stolen and Lin [23] under identical operating conditions.

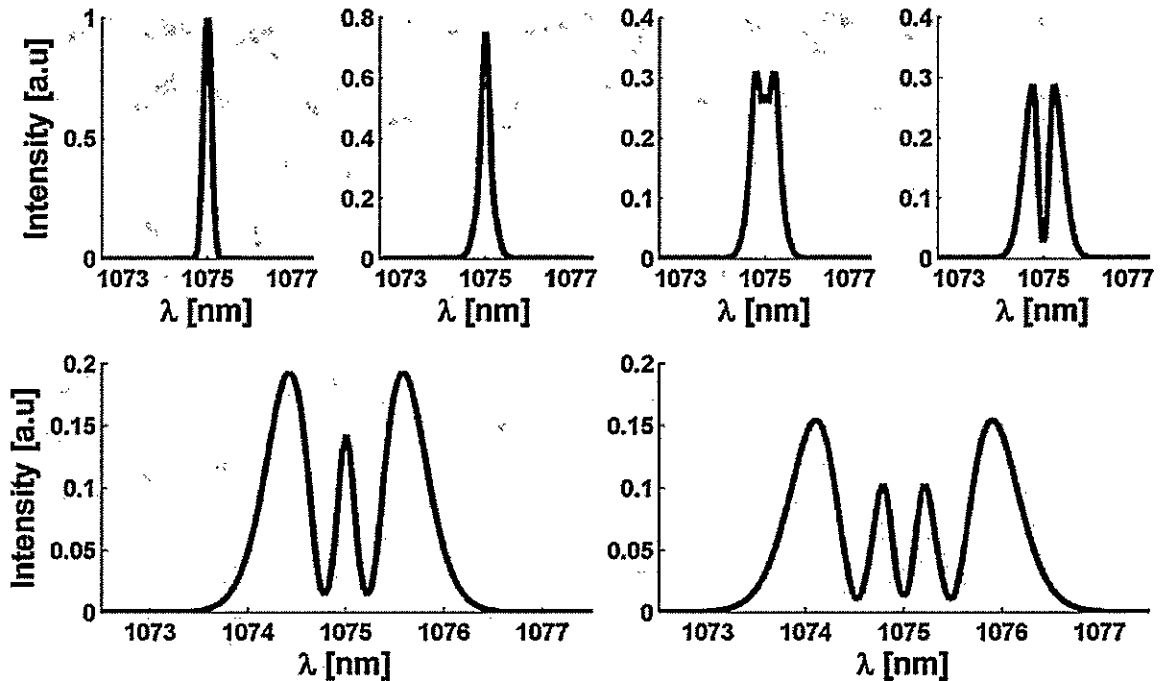


Figure 6-3 MCP simulation output for self-phase modulation with selected $\phi_{\max} =$ a) 0π b) 0.5π c) 1.0π d) 1.5π e) 2.5π and f) 3.5π respectively for a Gaussian input pulse and all other effects turned off.

Spectral broadening for the input Gaussian pulse as it propagates has been solved analytically by Pinault [30]:

$$\frac{\Delta\lambda}{(\Delta\lambda)_0} = \left(1 + \frac{4}{3\sqrt{3}}\phi_{\max}^2\right)^{\frac{1}{2}} \quad 6-6$$

$$\cong \left[1 + (0.88\phi_{\max})^2\right]^{\frac{1}{2}}$$

where $(\Delta\lambda)_0$ is the input RMS half-width in the wavelength domain, and the second line approaches an equality under the condition $\phi_{\max} \gg 1$. The following table lists the theoretical values of Equation 6-6 for selected distances down the fiber and also included are the calculated RMS widths utilizing the MCP simulator of Figure 6-3 shown above and which are in good agreement with the theory.

Table 6-1 RMS widths for an SPM-only MCP simulation compared to analytical results from Equation 6-6. Results are in good agreement.

ϕ_{\max}	Theoretical RMS [nm] $\left(1 + \frac{4}{3\sqrt{3}}\phi_{\max}^2\right)^{\frac{1}{2}}(\Delta\lambda)_0$	Theoretical RMS [nm] $\left[1 + (0.88\phi_{\max})^2\right]^{\frac{1}{2}}(\Delta\lambda)_0$	MCP Simulated RMS [nm]
0.0π	0.0893	0.0893	0.0893
0.5π	0.1521	0.1524	0.1498
1.0π	0.2618	0.2625	0.2581
1.5π	0.3799	0.3809	0.3733
2.5π	0.6218	0.6236	0.6112
3.5π	0.8661	0.8687	0.8515

The following verification step is used to benchmark input chirp and SPM. Figure 6-4 reveals two possible scenarios for positive ($C > 0$) and negative ($C < 0$) input chirp.

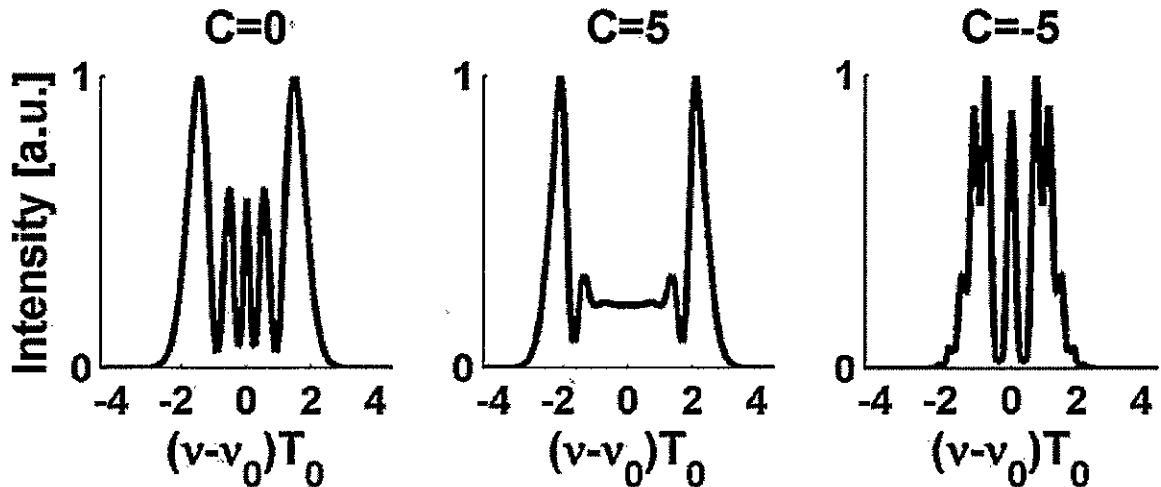


Figure 6-4 MCP simulation results are for SPM-only calculations with selected chirped input pulses. Results are in excellent agreement to identical SSFM simulations by Agrawal [3].

It is not beneficial at this point in the report to provide simulations for measurement of spectral width narrowing due to negative chirp and SPM alone, since such events are intrinsically dispersive over a length of the fiber when the length is greater than the dispersion length L_D . In such cases, GVD would have to be included in order for the calculation to make much sense. On the other hand, if $L_D \gg L_{NL}$ where

$L_{NL} = (\gamma P_0)^{-1}$ is defined as the length after which SPM is considered to play an important role in the numerical simulation [3], then provided that the fiber is short enough - some qualitative results from a simulation of chirp and SPM alone could be achieved. Refer to Limpert's article [70] for experimental research on SPM and negative input chirp interplay.

The time-frequency uncertainty principle applies to pulses at or near the transform limit [43]. Qualitatively this means that there is a finite region in time and frequency where most of pulse power is present. Spreading the signal samples further apart in time (i.e. extending the wings of the Gaussian pulse or effectively decreasing the sampling rate in time) causes a compression (or increase in sampling rate) of the signal in the frequency domain. This can be accomplished in the simulator by increasing the PBC variable (defined in Section 2.2.2) or decreasing the sample number N . With all this in mind, increasing the PBC variable will increase the resolution of the pulse where it really matters, in the region where most of the pulse power is defined within the frequency domain.

Since there can be several effects including GVD that are handled in the Fourier domain, it is beneficial to know ahead of time exactly how resolved the frequency domain will be for the calculations before any benchmarking is performed on the MCP simulator. For this purpose, a fast symmetric split-step Fourier method was implemented in Matlab. Several quick passive calculations can be made with results such as those illustrated in Figure 6-5 and 6-6 to determine operating conditions that are necessary for accurate results - at least for passive effects in a fiber simulation. Figure 6-5 illustrates an example where the spectrum is not resolved enough. If any GVD or other spectral

calculations are made for such operating conditions, it is clear that the results will not be accurate after pulses are propagated some distance. Improvement in the frequency domain resolution is illustrated in Figure 6-6, where the time domain has been down sampled. Note that the decrease in the spectral range scaling (compared to Figure 6-5) is due to the increased sampling period from increasing the PBC variable, a side-effect of fast Fourier transform normalization.

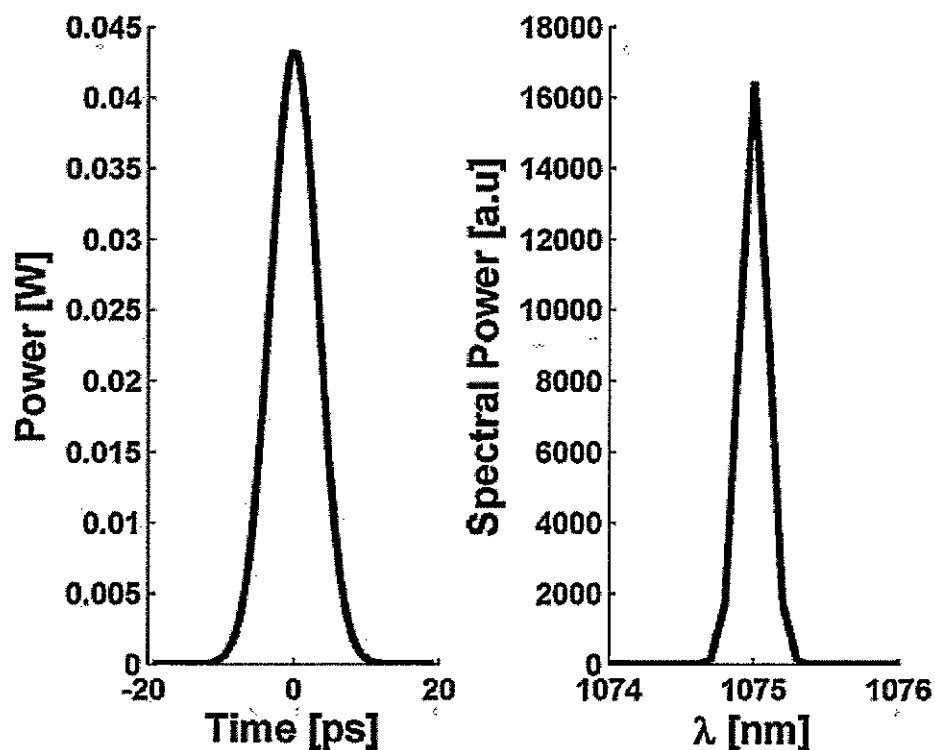


Figure 6-5 A Gaussian pulse (left) defined for $N=2048$ data points at $PBC=2.5$ in the time domain, and the corresponding spectrum (right).

Knowing ahead of time what resolutions were necessary saved computation time in the MCP simulations which calculate passive and active effects. In general, it is best to have as much resolution as possible for both domains, but sacrifice must be made due to the time-frequency uncertainty principle.

The same passive-only calculations could have been made on the MCP simulator for pre-testing. However, the algorithm was designed for simultaneous passive and active simulations and runs slowly even if the active components are turned off.

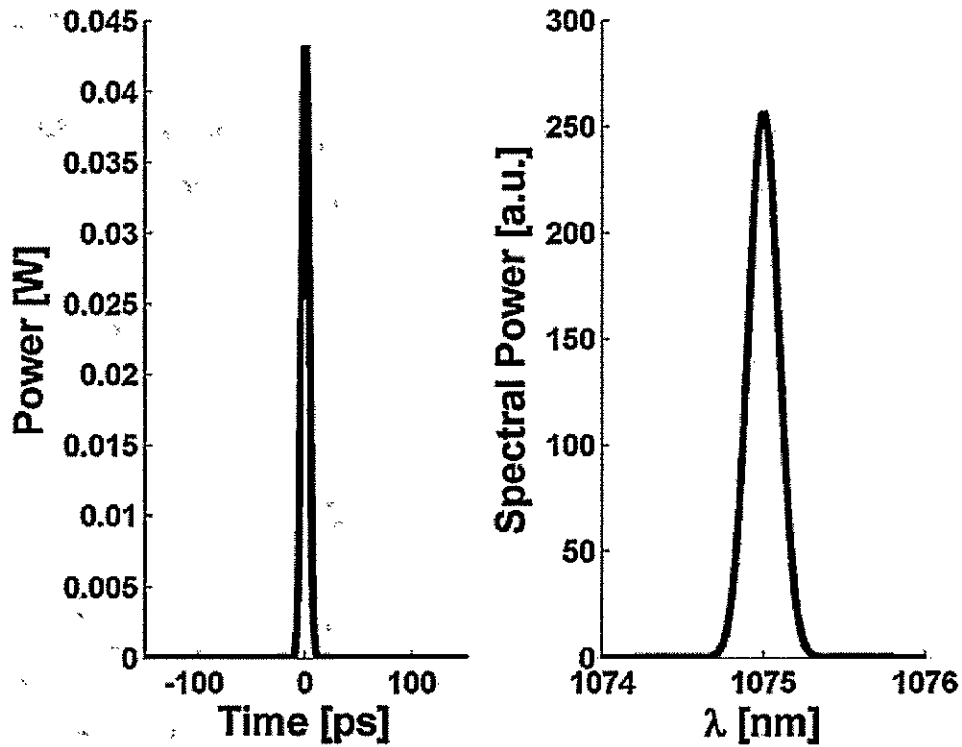


Figure 6-6 A Gaussian pulse (left) defined for $N=2048$ data points at $PBC=20.0$ in the time domain, and the corresponding spectrum (right).

6.3 GVD and SPM Verification

In the following simulation verification, all the significant passive effects according to the normalized NLS equation are considered. A very useful parameter N can be found [3]:

$$N^2 = \frac{L_D}{L_{NL}} = \frac{\gamma P_0 T_0^2}{|\beta_2|} \quad 6-7$$

This parameter should not be confused with the number of pulse samples which is defined in this report with the same variable. When $N \ll 1$, dispersion due to GVD is the dominant effect and therefore significant pulse broadening occurs in the time domain while the spectrum remains more or less the same over the dispersion length. In contrast, if $N \gg 1$, spectral broadening due to SPM is dominant while the time-domain pulse remains the same over the nonlinear length. If however $N = 1$ and $\beta_2 < 0$ (indicating that dispersion is in the anomalous region), then the traveling pulse quickly becomes a fiber soliton with amplitude time-distribution $\text{sech}^2(\tau)$. In Figure 6-7, a broadening plot was generated to show how an input Gaussian pulse broadens due to equally dominant GVD and SPM effects ($N = 1$). This plot is in excellent agreement with calculated and plotted results by Agrawal [3].

In the first case, with $\beta_2 > 0$, broadening from GVD reinforces broadening due to SPM (both causing a red-shift). This can be compared to a simulation with all the same conditions except that SPM is turned off (or in other words by setting $N=0$). It can be seen from the plot that the latter case is weaker in broadening the pulse. Finally, in case $\beta_2 < 0$, the broadening is observed in the region where the input Gaussian morphs into the sech^2 soliton function. At the soliton condition, the RMS half-width remains unchanged as can be seen if the figure were to be substantially extended in distance.

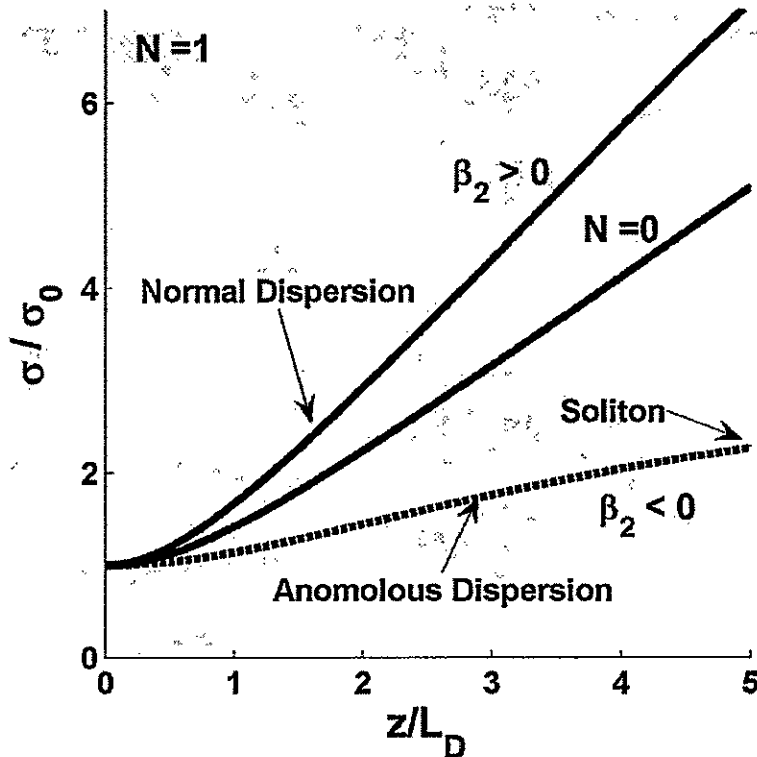


Figure 6-7 Time-domain broadening of a Gaussian pulse in normal and anomalous dispersion regimes when $L_D=L_{NL}$ or equivalently, $N=1$. In the case $\beta_2 < 0$, the Gaussian pulse morphs into a soliton (sech^2) pulse. Also included for comparison is the simulation output with SPM turned off with $N=0$. σ_0 is the initial RMS half-width.

6.4 Gain and ASE Simulation Results and Verification

The numerical calculation by the gain and ASE component is relatively complex. It was necessary to compare outputs to other simulators as well as published results to assure the correct operation when running active fiber simulations. The following subsections discuss in detail the verifications and benchmarks attained during the development cycle.

6.4.1 MCP Output Data Types

The MCP software provides detailed output data for the individual simulation. For each section along the fiber, these include:

1. Time-dependent amplitude
2. Frequency-dependent amplitude
3. Forward signal power
4. Forward and Backward Pump powers
5. Peak (pulse) powers
6. Forward and Backward ASE powers
7. Forward and Backward ASE spectra
8. Dopant energy population densities
9. RMS widths in time and wavelength domains, and
10. Gain coefficients for each time step and section along the fiber

Currently, all of the above are stored in a simulation output folder for future analysis after the simulation ends.

6.4.2 CW Results

For cw simulations, the MCP simulator was unchanged with respect to software code. In fact, the only difference from pulsed operation is in the input seed power which is set as the (time independent) value of average power of the input beam.

The operating conditions from the laboratory experiment include a MHz pulse repetition rate. At such high repetition rates one can expect that simulations performed in a cw regime will yield similar results to those from pulsed calculations. This can be explained by the high meta-stable 0.8 ms life-time of Ytterbium dopant atoms [32] – a

time over which almost half a million pulses would pass by (given a repetition rate of 577 MHz). Over this transient life-time, the dopant energy population densities are expected to stabilize to nominal levels because the dopants cannot fluctuate between energy levels quickly. For example, in erbium doped fiber amplifiers with a (long) relaxation life time of 10 ms (taken from [22]), and for rep-rates greater than 10 kHz, Giles [31] sets the time derivatives of the energy population densities to zero, a method used by many to model fiber amplification of cw input beams [38][75].

Thus, for qualitative results, high-repetition-rate pulsed fiber amplification may be simulated in the cw context. To perform a cw simulation for pulsed laboratory conditions, the input power was set constant and equated to the measured average power of the pulse train [33]. Simulation results are provided in Figure 6-8 to complement experimental results for 6 ps input pulses at a 577 MHz repetition rate and a peak wavelength 1075 nm. The input pulse train average power was measured to be 0.2 mW – also the value used for the cw input power. The double-clad fiber with (130 μm flat-flat) hexagonal inner cladding is 14.8 m long with core radius 3 μm and 0.13 numerical aperture.

CW simulations may not be sufficient for a fully quantitative and accurate simulation of the laboratory experiment. In Figure 6-8, the simulated output average powers for two selected relaxation time constants (refer to section 3.3.6) do not match exactly those that were measured in the ultra-fast laser lab by Andrew Budz. This may be due to several unknowns as discussed in the previous chapter; however it appears that the simulation with a shorter relaxation time constant is more accurate. Remember that a cw

simulation has been performed here for comparison to a pulsed experiment at high repetition rates.

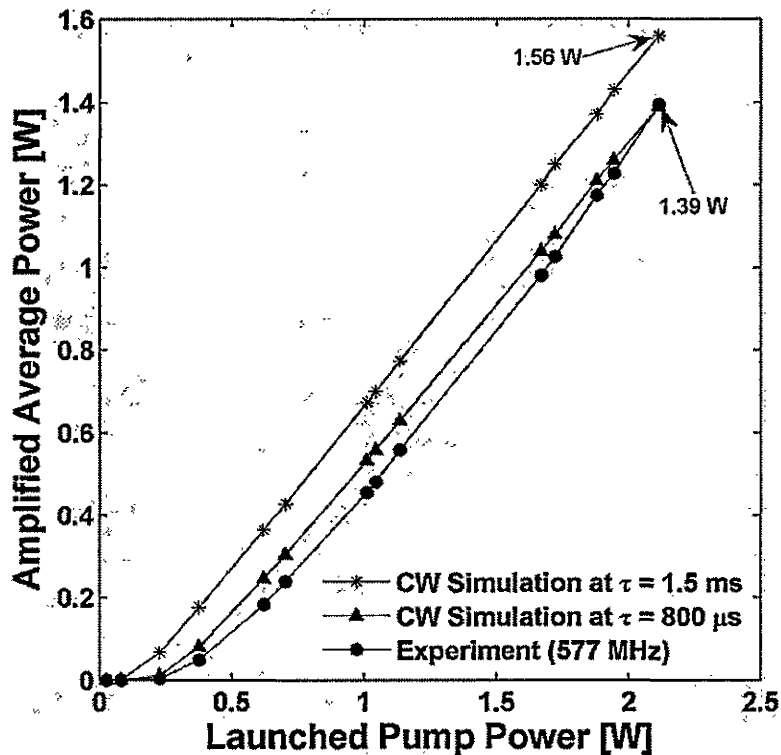


Figure 6-8 Output average powers for selected launched powers in the counter-propagating geometry. Experimental data (circles) are compared to simulation results (asterisks and triangles) at selected relaxation time constants. The lower time constant is adapted from

The cw simulations do not provide any details on the output pulse shape and phase information. However, there are some qualitative details from the cw model that can be useful.

In Figure 6-8, the slope efficiencies are similar. Performing a basic linear fit on the data, the slope efficiencies not including the weakest four pump powers are 80%, 77% and 81% from top to bottom respectively. Based on the selected initial conditions, one can always calculate approximate slope efficiency before starting the experiment. This way the MOPA system can be tailored for near-optimal output conditions. To investigate the predictability of the cw simulation for slope efficiencies, refer to Kelson

and Hardy's article [38]. The plot for a time constant at $800 \mu s$ is a last minute addition to the thesis and the results for the pulsed simulations that follow for modeling our laboratory experiment use the legacy time constant of 1.5 ms.

For 2.11 W of launched pump (last data point in Figure 6-8), the corresponding calculated power distributions for signal, pump, forward and backward ASE powers are provided in the Figures 6-9 and 6-10. The input signal is monochromatic at 1075 nm which is the center wavelength for one of 30 wavelength bins distributed over a selected region of 1000 - 1101.6 nm. The launched pump power is depleted by the time it reaches the left fiber facet. The excited level dopant concentration is therefore greater in the latter¹ part of the fiber (Figure 6-11) which at least partially explains why the signal and forward ASE powers get amplified mostly in that region.

Generation of backward ASE begins at the right half of the fiber and as it propagates to the left, it begins to rise significantly left of the 9 meter mark where signal and forward ASE powers no longer take up the majority of the stimulated emission energy. It is interesting to notice that backward propagating ASE remains pseudo-constant (with a slight dip at the end) for fiber length under 3 m. This semi-transparency was originally a concern pointed out by a colleague, Dr. Henry Tiedje during initial verification tests of the MCP algorithm.

¹ The latter part of the fiber is the right half side in the context of this simulation.

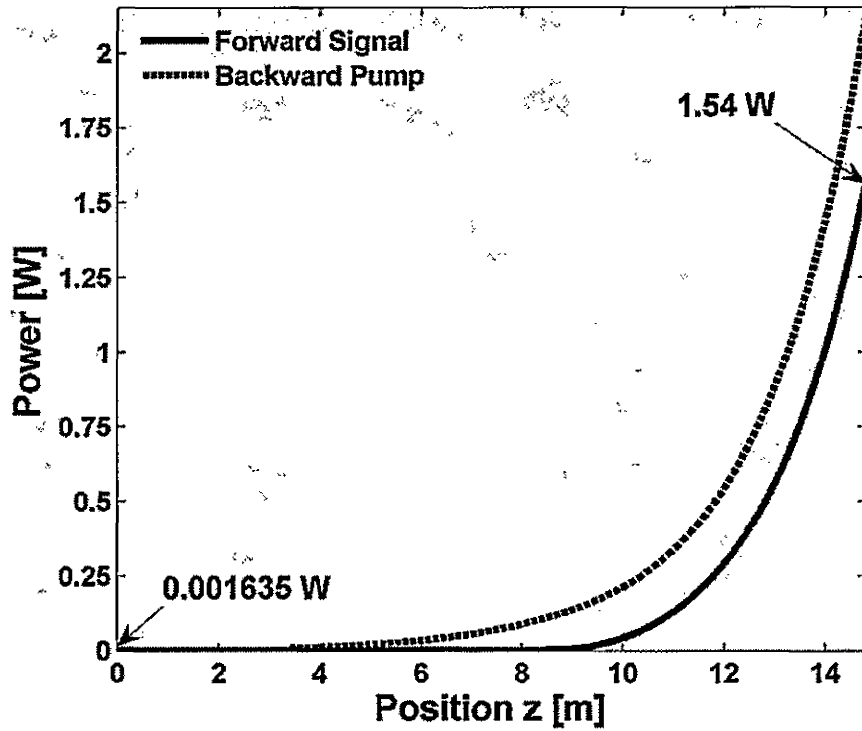


Figure 6-9 Power distribution down a 14.8 m fiber for the signal and pump for a cw simulation of the ultra-fast laser laboratory experiment with input pump power 2.11 W in the counter-propagation geometry.

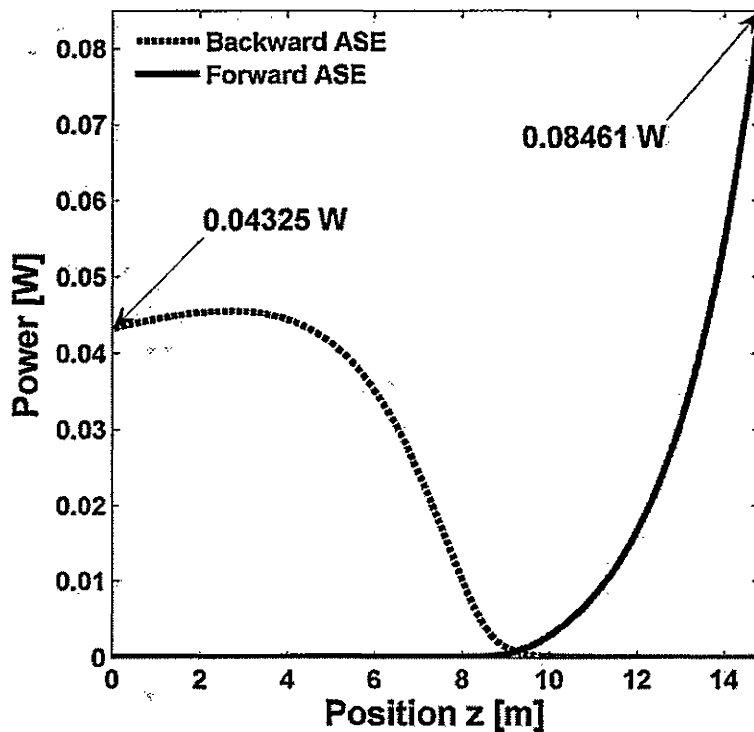


Figure 6-10 Magnified power distribution of forward and backward generated ASE from an MCP (cw) simulation.

With almost no pump power in this region, it would be expected that the backward ASE power would decrease dramatically due to absorption from high ground state energy population densities in this region. To explain the transparency phenomenon consider that the total number of de-excited dopants must equal the amount of those that are excited at any instant in time throughout this distance. Qualitatively, this can be expressed by Equation 6-8 assuming there are no degenerate states and that the gain $g(z)$ is set to zero at any instant in time for a particular z -position along the fiber. This approach is also taken by Pask to get the critical pump power necessary for transparent fiber operation [35].

$$g(z) = -(\sigma_a N_0 - \sigma_e N_1) = 0 \quad 6-8$$

Here $\sigma_e = 3.8 \times 10^{-25} \text{ m}^2$ and $\sigma_a = 3.9 \times 10^{-27} \text{ m}^2$ are the emission and absorption cross-sections at 1075 nm and $N_0 = 9.9 \times 10^{25} \text{ m}^{-3}$ and $N_1 = 8.6 \times 10^{23} \text{ m}^{-3}$ are the two metastable (Figure 6-10) converged averaged dopant energy population densities for the first 3 meters of the YDFA. Substitution into Equation 6-8 results in an overall dopant absorption of 0.05 m^{-1} or 217 dB/km. This loss parameter should be considered qualitative as it does not incorporate all the physical interactions of the simulation. However, it is clear that losses due to absorption are minimal for this length of fiber and one should not expect the backwards ASE to dip too quickly. For completeness, using the 217 dB/km figure, one may calculate the total drop from the highest power (at 3 meters) to left fiber facet to be approximately 7 mW, a relatively small power difference indeed.

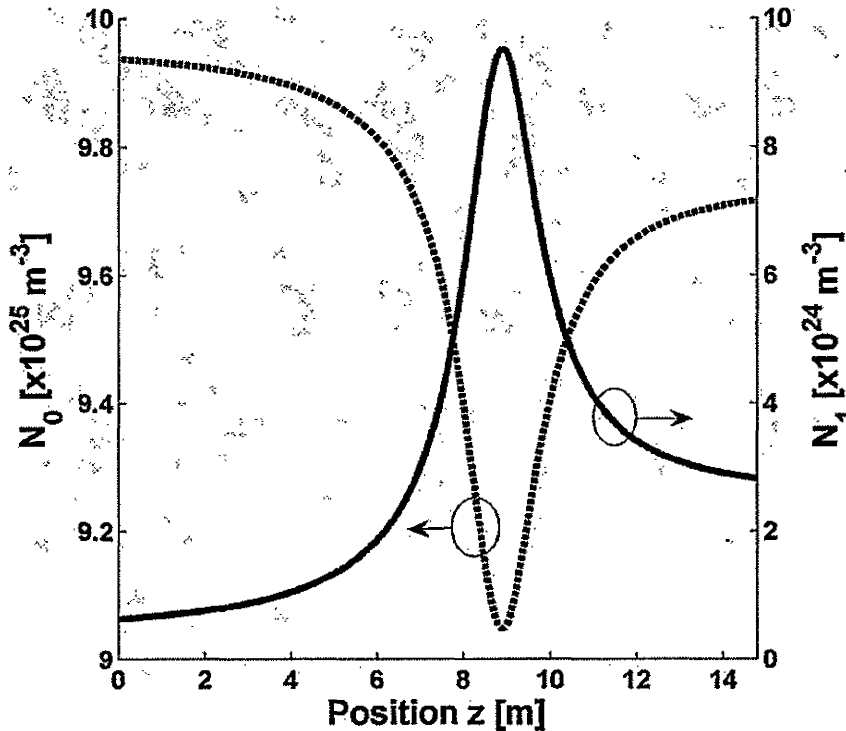


Figure 6-11 Excited level concentration is highest at 9 m down the 14.8 m fiber. For the YDFA, there are two metastable energy levels that interact with the input powers with N_0 and N_1 representing the ground and excited state dopant energy population densities in $[m^{-3}]$ respectively.

We were fortunate enough to have access to a cw simulator developed by Bertrand Morasse for his M. Sc. thesis at Laval University [36]. As with all cw simulators, the time-dependent differentials for the dopant population densities are set to zero. The transient dopant energy concentrations are then solved analytically and used as iteration expressions in the numerical simulation of power equations.

The aforementioned approach cannot support pulsed conditions. Nevertheless, it was very useful in verification of the MCP algorithm running in the cw regime. Before showing any output comparisons, it is useful to remark on some common operations that are programmed differently between our two simulators and how these differences can affect the results for identical initial conditions.

Morasse implemented the Runge-Kutta method [37] for solving the differential power propagation equations. Unfortunately, Runge-Kutta takes too long to execute and with the added overhead of solving for space *and* time dependent ordinary differential equations, the MCP algorithm would take orders of magnitude longer to compute for identical operating conditions. A simplified method of finite-difference has been implemented to improve the processing speed of the MCP algorithm. This method is also used by Wang [32] for the same purposes. As pointed out by Eichhorn [8], provided the differential step sizes are small enough the simplification to finite-difference is valid.

The MCP algorithm also approximates the fundamental mode-field distribution to a Gaussian function:

$$I_{s,j}(r, \phi) = \frac{2P_{s,j}}{\pi w_j^2} \exp\left(\frac{-2r^2}{w_j^2}\right) \quad 6-9$$

where $I_{s,j}$, $P_{s,j}$ and w_j are the intensity, power and radial-standard-deviation respectively of the mode signal at the j^{th} wavelength bin. In contrast, for the purposes of maximum accuracy, Morasse has set the mode-field distribution to the ideal theoretical LP_{01} function. This would entail additional computation of the Bessel and modified Hankel functions discussed earlier in chapter 2 resulting in further accuracy of the results.

In reality, the dopant concentration is distributed non-uniformly with respect to the radial direction inside the fiber core. For simplicity, the MCP algorithm implements a uniform dopant distribution from the fiber axis in the core to the inner-cladding interface. In contrast, Morasse incorporated a dopant distribution that confines a majority of the dopant ion concentration to the core axis. Therefore, the dopant densities become radially

dependent $N_0 \rightarrow W(r)N_0$ and $N_1 \rightarrow W(r)N_1$. The power propagation formalism for Ytterbium (Equations 3-17 to 3-20) is generalized accordingly:

$$\frac{\partial N_1}{\partial \tau} = \int_0^{2\pi a} \int_0^0 \left[\begin{array}{l} \frac{N_0}{hc} \sum_{j=0}^h \sigma_a(\lambda_j) \frac{\lambda_j}{\pi a^2} \left(\frac{2P_{s,j}}{\pi w_j^2} \exp\left(-\frac{2r^2}{w_j^2}\right) \right) \\ - \frac{N_1}{hc} \sum_{j=0}^h \sigma_e(\lambda_j) \frac{\lambda_j}{\pi a^2} \left(\frac{2P_{s,j}}{\pi w_j^2} \exp\left(-\frac{2r^2}{w_j^2}\right) \right) \\ + \frac{N_0}{hc} \sigma_a(\lambda_p) \lambda_p D \frac{P_p^+ + P_p^-}{\pi a^2} - \frac{N_1}{hc} \sigma_e(\lambda_p) \lambda_p D \frac{P_p^+ + P_p^-}{\pi a^2} \\ - R_{10} N_1 \end{array} \right] W(r) r dr d\phi \quad 6-10$$

$$\frac{\partial N_0}{\partial \tau} = -\frac{\partial N_1}{\partial \tau} \quad 6-11$$

$$\frac{\partial P_{s,j}}{\partial z} = \mp \alpha_{s,j} P_{s,j}$$

$$+ \int_0^{2\pi a} \int_0^0 \left[\begin{array}{l} \mp \sigma_a(\lambda_j) \left(\frac{2P_{s,j}}{\pi w_j^2} \exp\left(-\frac{2r^2}{w_j^2}\right) \right) N_0 \pm \sigma_e(\lambda_j) \Gamma_j \left(\frac{2P_{s,j}}{\pi w_j^2} \exp\left(-\frac{2r^2}{w_j^2}\right) \right) N_1 \\ \pm \sigma_e(\lambda_j) \left(\frac{2 \left(M_j \frac{2hc^2}{\lambda_j^3} d\lambda_s \right)}{\pi w_j^2} \exp\left(-\frac{2r^2}{w_j^2}\right) \right) N_1 \end{array} \right] W(r) r dr d\phi \quad 6-12$$

$$\frac{\partial P_p^\pm}{\partial z} = \mp \alpha_p P_p^\pm + \int_0^{2\pi a} \int_0^0 \left[\mp \sigma_a(\lambda_p) D P_p^\pm N_0 \pm \sigma_e(\lambda_p) D P_p^\pm N_1 \right] W(r) r dr d\phi \quad 6-13$$

In the above equations $P_{s,j}^+ + P_{s,j}^- \rightarrow P_{s,j}$ is the forward propagating signal. In the current MCP version, only a forward propagating signal has been programmed to propagate according to the positive convention illustrated earlier in Figure 3-2. Pump

powers can be launched from one or both fiber ends. Refer to [39] for more details on the dopant distribution function $W(r)$.

Morasse's cw simulation is completed when the dopant energy population densities (solved by setting the time-differential to zero) differ by 0.01% from their previous values set using the powers of the previous propagation iteration. The MCP simulator pursues the simulation until the outputs remain unchanged (or converge to within four or more decimal places) after increasing time and space resolutions by two. There are many forms of convergence that can be observed, such as the unchanging values of output powers or the dopant-population-densities. For convergence measurements, the latter is implemented in the MCP algorithm. The difference in convergence strategies can also be used to explain the minor differences in simulation outputs at long fiber lengths, cases for which high spatial resolution would need to be set.

We now proceed to the qualitative comparison of simulation outputs of the pulsed MCP algorithm (running in the cw regime) and Morasse's cw simulator. Note that it is hard to tell quantitatively how differences (where ever they occur) come about as the inner workings of Morasse's cw simulator are not known to us. The operating conditions are the same for both simulators and are provided in Table 6-2 below.

Many simulations were performed for several fiber lengths and the set of results illustrated in Figure 6-12 include the output signal and pump powers for those selected cuts. Each fiber length in the figure corresponds to the output powers from the right facet (due to the choice of co-propagating geometry) for an individual simulation.

The output signal for fiber lengths greater than 5 m varies between simulators, however it is clear that this variation is minimal (powers within 2% of one another).

Figure 6-13 provides the corresponding output ASE powers from both fiber facets.

Table 6-2 Parameters used for comparison of the MCP and Morasse's simulators operating in the cw regime. No Fresnel's losses have been taken into account here, as they have also been set to zero by Morasse in his simulation.

Operating Parameter	Value	Description
λ_s	1075.0 nm	cw Peak (Operating) wavelength
λ_p	976.0 nm	cw Pump Wavelength
P_{avg}	0.001 W	Average Seed Power
P_p	4.0 W	Average Pump Power
L	1,2,...,10 m	Fiber Length
n_{SiO_2}	1.45	Silica (Background) Index of Refraction
$NSTEPS$	501	Fiber discretization (length divided by $NSTEPS - 1$)
σ_a	Figure 3.6 [m ²]	Absorption Cross-Section
σ_e	Figure 3.6 [m ²]	Emission Cross-Section
a	3.0 μ m	Core Radius
A_p	1.35×10^{-8} m ²	Inner-Cladding area (for the pump overlap function)
NA	0.13	Core numerical aperture
N_0	1.0×10^{26} m ⁻³	Dopant Concentration
τ	0.8 ms	Radiative relaxation time constant
α_s, α_p	0.0046 m ⁻¹	Background Signal & Pump loss respectively

For both simulators, the mathematical modeling of ASE (noise power generation) is identical (Equation 6-12). Numerically, however, it is a different story since N_1 , the excited (or upper) energy dopant population density, is calculated in two different ways (discussed above in the differences between the two simulators) throughout the numerical process. Inconsistencies in the backward ASE powers (exiting the left facet) in Figure 6-13 are caused by these dissimilar calculations of the physical interactions of the Ytterbium upper energy population N_1 .

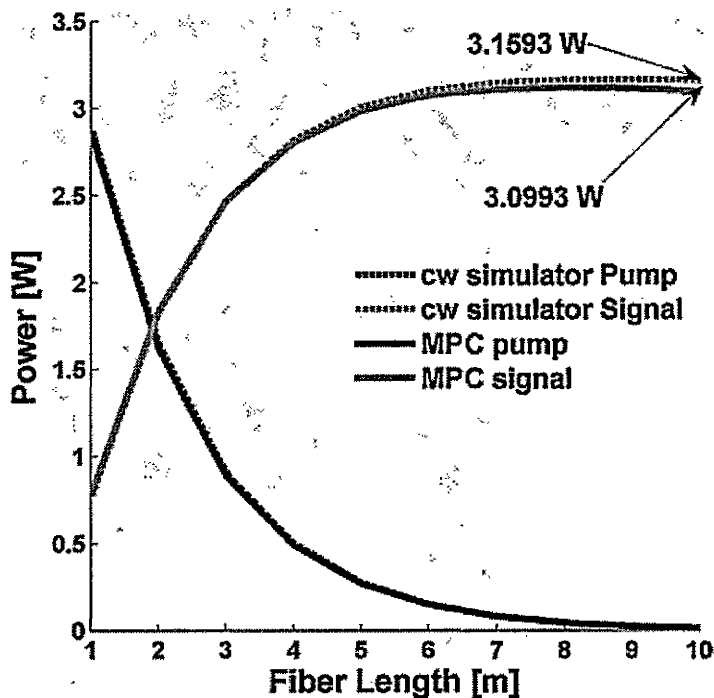


Figure 6-12 Output power versus fiber cut where each unit of fiber length (1, 2 ... 10 m) corresponds to a simulation for that length. The solid lines correspond to the MPC simulation outputs and Morasse's cw simulation is indicated by dashed lines.

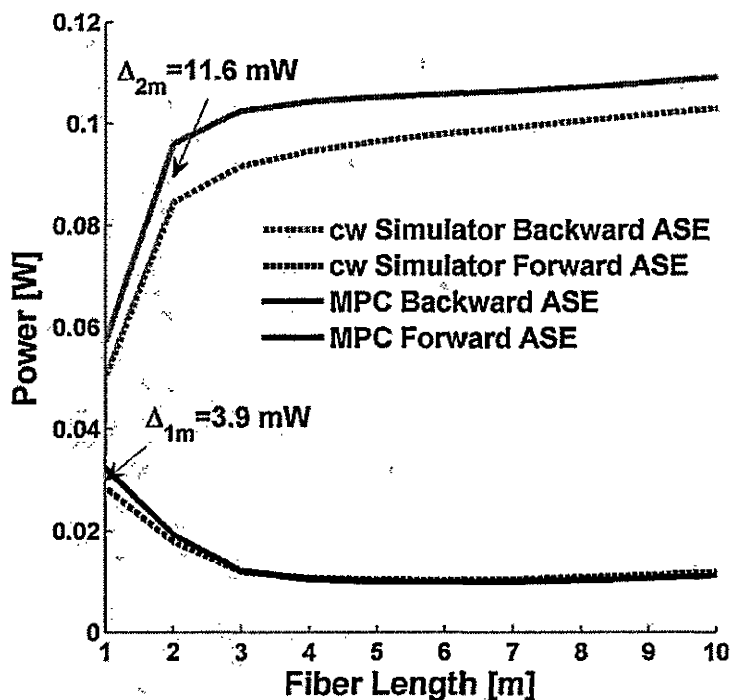


Figure 6-13 Forward and backward ASE outputs from two simulators. Backward ASE is output at the left fiber facet ($z=0$). Each data point corresponds to the total power for all 21 wavelength bins evenly ranging from 1000 nm to 1100 nm.

The two simulator outputs are compared for the 10 m fiber simulation in Figures 6-14 and 6-15 that illustrate the power distributions for signal, pump, forward and backward ASE.

The ASE power is distributed on a bandwidth of wavelengths including the operating wavelength $\lambda_s = 1075$ nm as shown in Figure 6-16. The amplification of this power is numerically conducted in the same way as for the signal and pump powers. It is clear that the ASE (Figure 6-15) is weaker than the signal power (Figure 6-14). Even though a component of the ASE power is at the signal wavelength, the ASE noise and/or total ASE power generated spontaneously at this wavelength is much lower than the signal seed power launched into the fiber. Therefore stimulated emission favors the amplification of the signal power at any point along the fiber. This is also evident from Figures 6-14 and 6-15 where one can observe that the signal power is amplified much more than the forward ASE.

Backward propagating ASE gets generated at all points along the fiber as well. As it propagates counter-directionally, significant amplification occurs for ASE at lengths to the left of (or below) 0.5 m. Excited level dopant concentration and hence amplification of ASE is minimal at longer distances down the fiber due to pump depletion as well as a dominant signal power in that region. When signal power is minimal (which is the case for lengths under 0.5 m) ASE takes advantage of the non-depleted excited dopant concentration which explains the exponential increase of the backward propagating ASE in Figure 6-15.

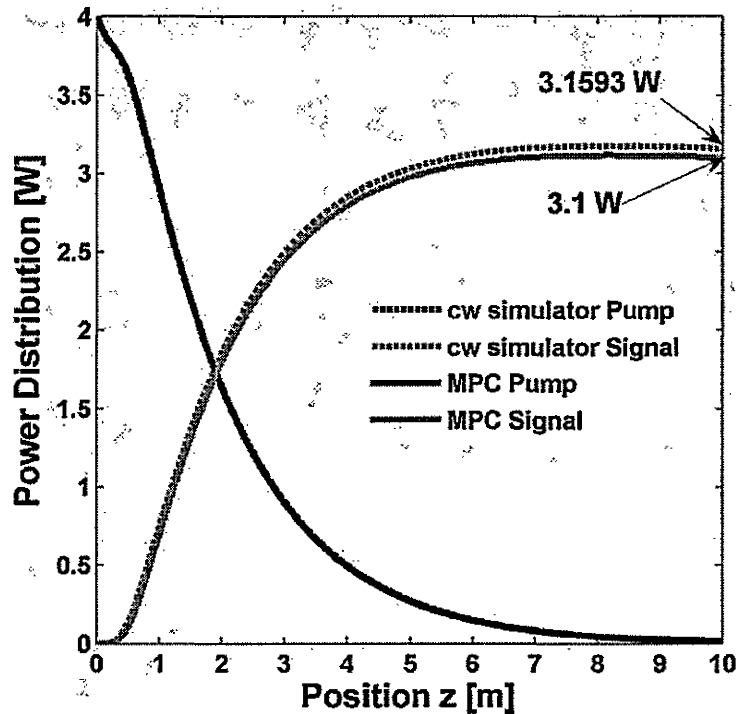


Figure 6-14 The distribution of power throughout a 10 m long fiber for the forward propagating signal and pump powers. The solid lines correspond to the MPC simulation outputs for identical operating conditions to that of Morasse's cw simulation indicated by dashed lines.

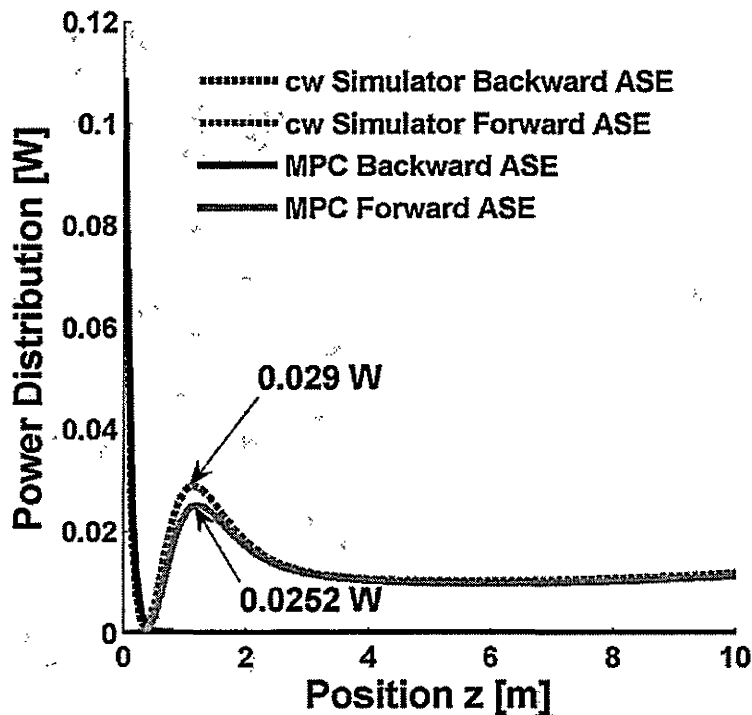


Figure 6-15 Power distribution throughout a 10 m long fiber for the forward and backward ASE powers. Each data point corresponds to a total averaged power for all 21 wavelength bins ranging from 1000 nm to 1100 nm.

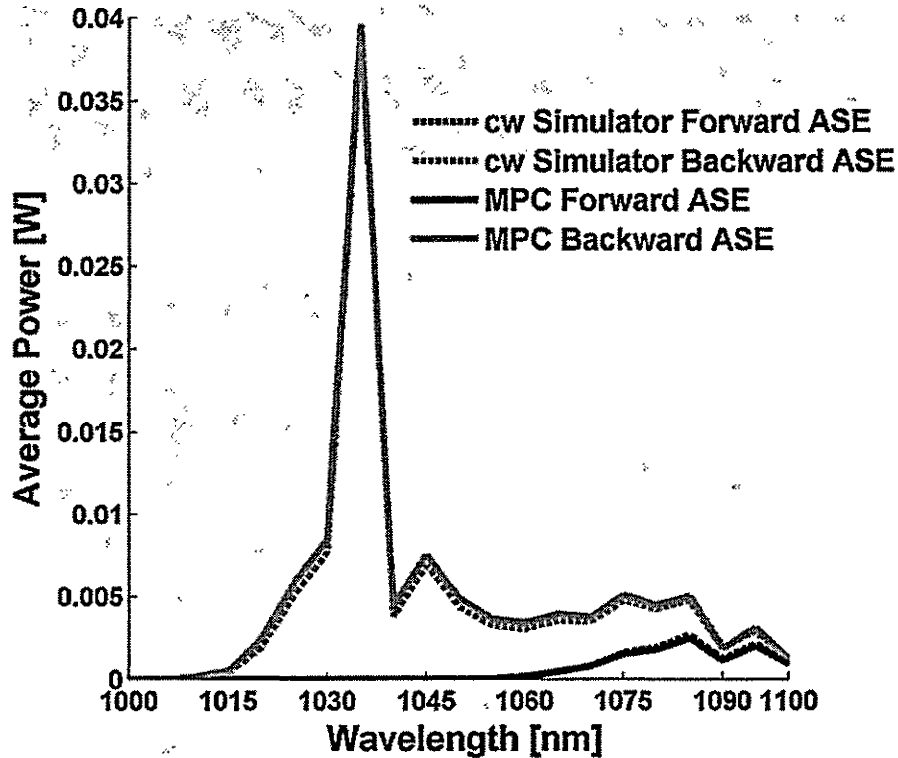


Figure 6-16 Output ASE powers versus wavelength for each of the 21 wavelength bins that are distributed evenly from 1000 nm to 1100 nm. The backward ASE powers are taken from the left facet of the fiber (Figure 3-2).

Most of the ASE power is generated at longer wavelengths than the pump wavelength at 976 nm as illustrated in Figure 6-16 above. In the Figure 6-17, the energy conservation issue is addressed for the signal, ASE and pump powers throughout the fiber amplifier.

The Ytterbium energy level structure has been discussed in Section 3.3.6. Assuming a three level laser scheme, the quantum efficiency [10] is defined as:

$$e_{\max} = \frac{\nu_s}{\nu_p} = \frac{\lambda_p}{\lambda_s} \quad 6-14$$

where ν_s and ν_p are the signal and pump frequencies respectively. According to this equation, the power conversion efficiency from the pump to the signal can be up to 90.8%. The remaining 9% is lost (in the ideal case) when the entire pump power goes

towards generation of signal power. According to Figure 6-17, about 25% has been lost in the MCP simulation. The remaining 15% is accounted for by intrinsic losses, a radiative relaxation rate R_{10} , and uncertainty in the emission and absorption cross-sections. Setting α_s , α_p and R_{10} to zero in the same simulation yields the dashed plot in Figure 6-17 below, which is still 130 mW short of the maximum amount of power that can be extracted after the ideal quantum efficiency is taken into account.

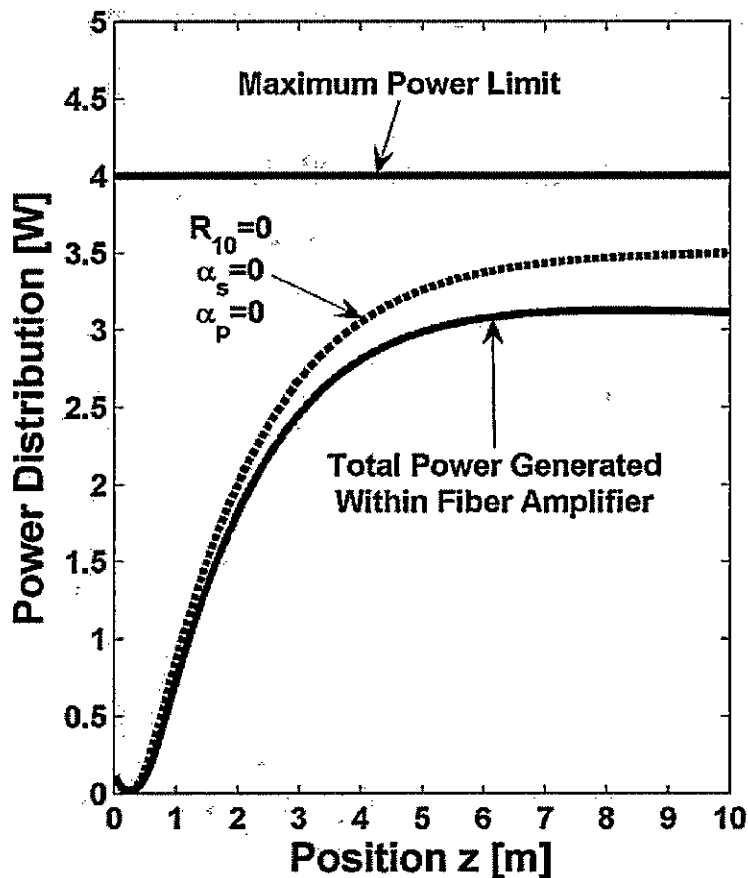


Figure 6-17 Total power distribution, generated within the fiber amplifier as a sum of signal, forward and backward ASE powers from Figures 6-14 and 6-15 throughout the fiber length. Also included is the limit for the total power which is equal to the total launched pump power of 4.0 W. The dashed curve shows the result for the condition $R_{10} = \alpha_s = \alpha_p = 0$.

An overall power conversion is modeled by the cross-sections for emission and absorption measured from a real experiment and which contribute to a quantum

efficiency that is most likely lower than the ideal one [10] discussed above. This can be considered to account for the remaining difference.

Several pulsed simulations were performed by the MCP simulator as per Morasse's request. These will be discussed in the following sections after pulsed simulation benchmarking.

6.4.3 Pulsed Simulation Results

A number of journal papers are available for simulation benchmarking of YDFAs as discussed in Chapter 1. Yet, Ytterbium is not the most exotic dopant atom used in fiber amplifiers. For example, the Thulium atom is much more complex with twice as many energy levels and additional light-matter interactions such as cross-relaxation and non-radiative relaxation with parameters available in the literature. It was beneficial to benchmark our simulator with relevant results from a Thulium doped fiber amplifier experiment, the most complicated system that could be found in the literature with enough information for the purposes of comparison. It was then expected that our simulator should work for simpler Ytterbium-doped systems. In addition, it is beneficial to have a simulator that is flexible when choosing from a variety of doped fiber amplifiers.

Eichhorn programmed a pulsed simulator that incorporates gain and ASE in order to model his Thulium-doped D-shaped double-clad fiber amplifier [8]. This fiber has a ZBLAN core background material and its spectroscopic data can be found in Walsh's article [40]. Two cross-relaxation parameters are taken into account and they seem to be the dominant cause of laser action in the fiber. All three propagation geometries (section 3.1.2) were simulated with the operating conditions of Table 6-3 to produce Figure 6-18.

Table 6-3 Parameters used for comparison of the MCP and Eichhorn's pulsed simulations in modeling pulsed operation of Tm:ZBLAN double clad fiber amplifiers with a D-shaped inner cladding. Note that the signal overlap function Γ_j from Equation 3-6 is generated dynamically on software initialization. Radiative and non-radiative time-constants are provided in Chapter 3.

Operating Parameter	Value	Description
PBC	2.5	Pulse Boundary Coefficient (Defined in section 3.2.2)
FWHM	30.0 ns	Full Width at Half Maximum
λ_s	1870.0 nm	Pulse Peak (Operating) wavelength
λ_p	800 nm	cw Pump Wavelength
$\sigma_{a,p}$	$1.96 \times 10^{-25} \text{ m}^2$	Absorption Cross-Section at the Pump Wavelength
$\sigma_{e,p}$	$4.83 \times 10^{-25} \text{ m}^2$	Emission Cross-Section at the Pump Wavelength
P_0	4.0 W	Seed (Gaussian) Pulse Peak Power
$P_{avg,ASE}$	0.5 mW	Seed Average ASE Power
P_p	3.0 W	Average Pump Power
L	1.0,1.2,1.5,1.7 2.0,2.2,2.5 m	Fiber Length
n_{ZBLAN}	1.49	ZBLAN (Background) Index of Refraction
$NSTEPS$	200	Fiber discretization (length divided by $NSTEPS - 1$)
ν_{rep}	60 kHz	Repetition Rate
σ_a	Figure 3.5 [m^2]	Absorption Cross-Section
σ_e	Figure 3.5 [m^2]	Emission Cross-Section
a	7.5 μm	Core Radius
A_p	$1.079 \times 10^{-8} \text{ m}^2$	D-Shaped Inner-Cladding area
D	0.016	Pump Overlap Function $\pi a^2 / A_p$
NA	0.12	Core numerical aperture
N_0	$4.69 \times 10^{26} \text{ m}^{-3}$	Dopant Concentration
k_{3011}	$7.86 \times 10^{-24} \text{ m}^3/\text{s}$	Cross-Relaxation
k_{1130}	$6.00 \times 10^{-25} \text{ m}^3/\text{s}$	Cross-Relaxation
M	12	Number of spatial modes
PA	12.0 degrees	Fiber facet polishing angle
α_s	0.0 m^{-1}	(Negligible) Background Signal loss
α_p	0.0 m^{-1}	(Negligible) Background Pump loss

Simulation results in Figure 6-18 are in excellent agreement to that found in Eichhorn's article [8]. At some distance down the fiber (provided it is long enough), the

ASE power begins to overtake the signal power as the dominant energy extractor of the doped fiber. It is important to design the fiber length such that the optimal signal power can be achieved, and from the figure, this length is 1.5 m. Notice that if the fiber length is too long, it can be detrimental to the required output signal power.

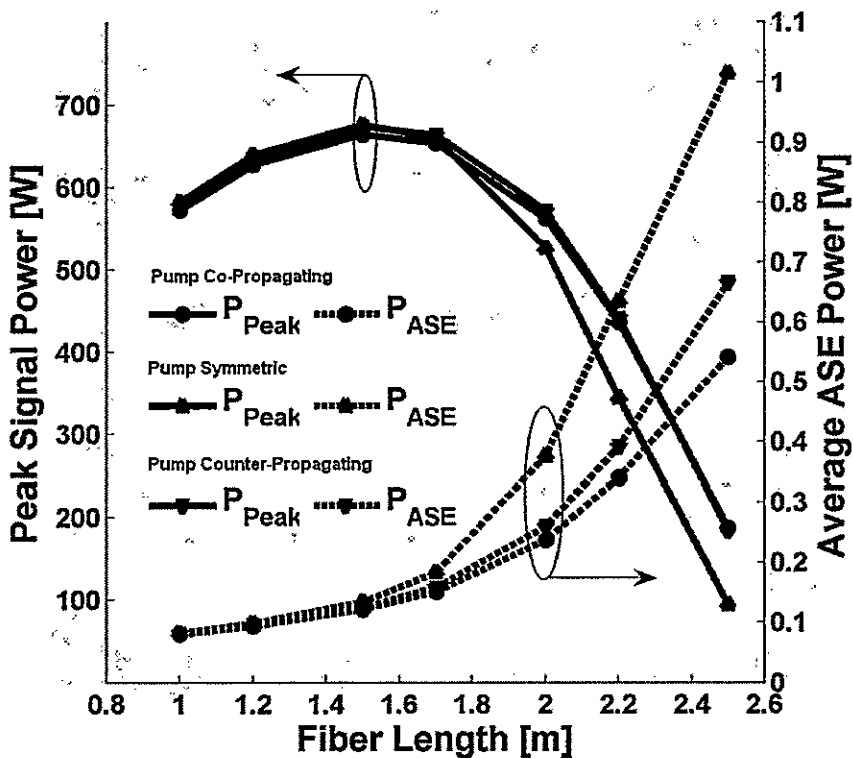


Figure 6-18 Output power simulation results for a Thulium doped D-shaped inner-clad fiber amplifier for three different propagating geometries. The input pump power is 3 W. For the symmetric propagation scheme, 1.5 W is launched at both facets. At 1.5 m, ASE becomes the dominant energy extractor. These results are in excellent agreement to Eichhorn's simulation results [8].

This benchmark is sufficient for the pulsed simulation verification of the MCP algorithm with only gain and ASE considered in the calculations.

At this point in the development process, the MCP simulator has come into use for external groups. A series of simulations were performed for Bertrand Morasse and his company CorActive based in the city of Montreal, Canada. One requirement was not met

however, which was the inclusion of SRS in the simulation (a future endeavor to be implemented into the simulations). Silica, which is the background material of the YDFA used by Morasse, has a very broad Raman gain spectrum. As a signal pulse propagates, its higher frequency photon components are downshifted to photons at a lower Stokes frequency. The strength of each frequency down conversion is a function of the Raman gain g_R in units of [m/W]. If the signal peak power is high enough, it may partially annihilate to create Stokes (and anti-Stokes) beams, a detrimental process for the signal quality as it adds noise power to the system for many wavelengths. SRS becomes a significant factor after the signal peak power exceeds a calculated peak power P_0^{th} which can be solved using Equation 5-8 with values from Table 6-4 below and assuming an effective core area of $\pi a^2 = 78.5 \mu\text{m}^2$. Refer to section 5.10 for more details. The following results will show simulations for signal powers above the SRS power threshold just introduced. Without SRS calculations included, a simulation of gain and ASE was sufficient for Morasse's qualitative purposes. In the near future, SRS capability is to be implemented into the simulation software to show how the results differ. The operating parameters for the simulations are provided in Table 6-4 followed with the simulation results illustrated in Figures 6-19 and 6-20 for a co-propagating geometry.

The output signal power increases as the pump power rises in an almost linear manner, yet the trend is non-linear at much higher pump powers. When gain saturation occurs (i.e. the output signal power is limited to some maximum value regardless of the pump intensity), the energy from the increased pump is primarily channeled into ASE power. Figure 6-20 illustrates this with an increasing trend in the output ASE powers with respect to launched pump power. The simulations were made for pump powers up to 50

W. This relationship is not limited to the YDFA and can be observed in other fiber amplifiers. For example, experiments with Thulium-doped fiber amplifiers have shown similar results [41]. It is this property between ASE and pump power which offers some metric in the validity of the simulation made.

Table 6-4 Parameters used for MCP pulsed simulation 20 kHz rep-rate for a co-propagating geometry. The signal overlap functions Γ_j from Equation 3-6 are generated on software initialization.

Operating Parameter	Value	Description
PBC	2.5	Pulse Boundary Coefficient (Defined in section 3.2.2)
FWHM	100.0 ns	Full Width at Half Maximum
λ_s	1064.0 nm	Pulse Peak (Operating) wavelength
λ_p	915 nm	cw Pump Wavelength
$\sigma_{a,p}$	$7.45 \times 10^{-25} \text{ m}^2$	Absorption Cross-Section at the Pump Wavelength
$\sigma_{e,p}$	$2.47 \times 10^{-26} \text{ m}^2$	Emission Cross-Section at the Pump Wavelength
P_0	75.0 W	Seed (Gaussian) Pulse Peak Power
P_p	3.0, 7.0 and 11.0 W	Average Pump Power
L	10.0 m	Fiber Length
n_{SiO_2}	1.45	Silica (Background) Index of Refraction
<i>NSTEPS</i>	501	Fiber discretization (length divided by <i>NSTEPS</i> - 1)
ν_{rep}	20 kHz	Repetition Rate
σ_a	Figure 3.6 [m^2]	Absorption Cross-Section
σ_e	Figure 3.6 [m^2]	Emission Cross-Section
a	5 μm	Core Radius
A_p	$1.33 \times 10^{-8} \text{ m}^2$	Hexagonal Inner-Cladding area
D	0.0059	Pump Overlap Function $\pi a^2 / A_p$
NA	0.12	Core numerical aperture
N_0	$1.0 \times 10^{26} \text{ m}^{-3}$	Dopant Concentration
τ	0.8 ms	Radiative relaxation time constant
M	1	Number of modes
PA	8.0 degrees	Fiber facet polishing angle
α_s	0.00023 m^{-1}	(Negligible) Background Signal loss
α_p	0.00023 m^{-1}	(Negligible) Background Pump loss

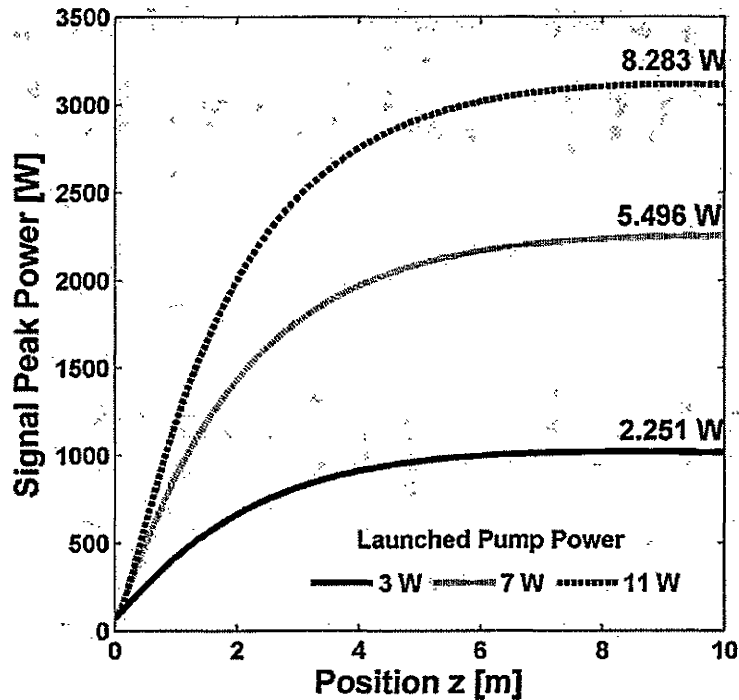


Figure 6-19 Pulsed simulation output signal peak power distributions for selected launched pump powers. Numerical analysis takes into account gain and ASE only. Also provided above each plot is the output average signal power.

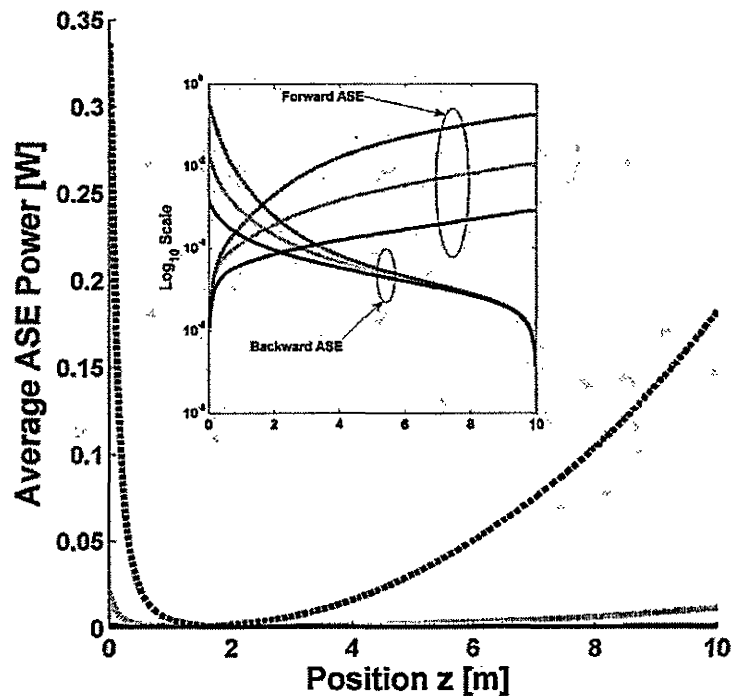


Figure 6-20 Pulsed simulation output average ASE power distributions for selected launched pump powers. The inset shows the same plot in logarithmic scale revealing the lowest power ASE generation at a 3W pump that is difficult to make out in the outer figure. Refer to the legend in Figure 6-19 for details on each line pattern.

The simulator can provide the user with a great deal of data such as, for example, the time-behavior of the output pulses as shown in Figure 6-21, for selected launched pump powers. The leading edge is more amplified than the trailing edge. It shows that the gain is directly dependent on time and space dependent dopant energy population densities.

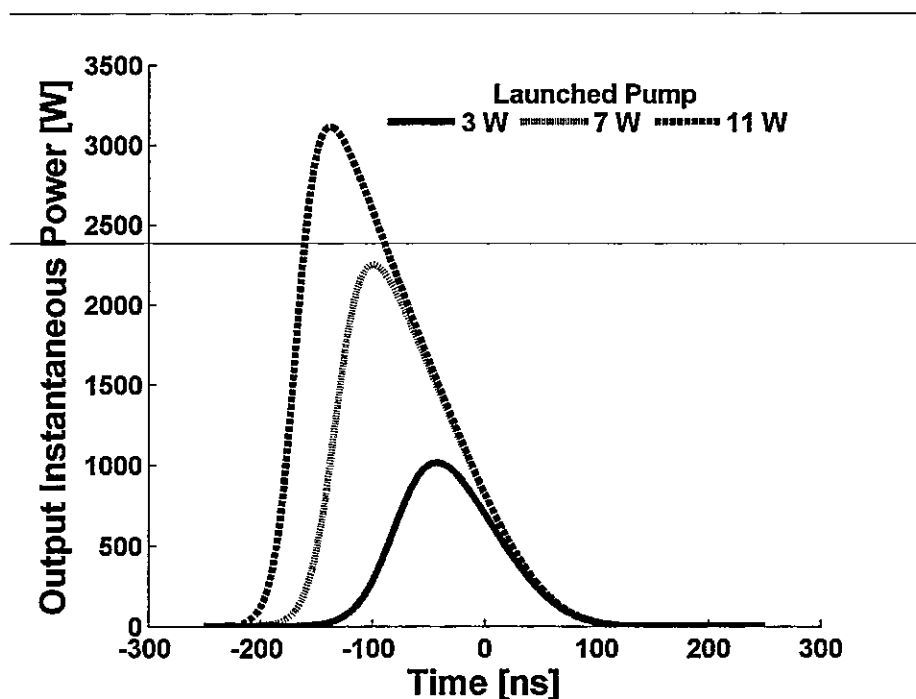


Figure 6-21 Output instantaneous pulse powers for three selected pump powers. Peak powers correspond to those at 10 m in Figure 6-19. Asymmetric distributions are caused by gain saturation within the fiber amplifier.

A series of other simulations were made for Morasse using the MCP simulator. In the most recent analysis, a new set of cross-sections were provided. During the development cycle, I coded a custom cross-section importer and so it was no problem to set up the new simulation. The emission and absorption cross-sections are illustrated in Figure 6-22.

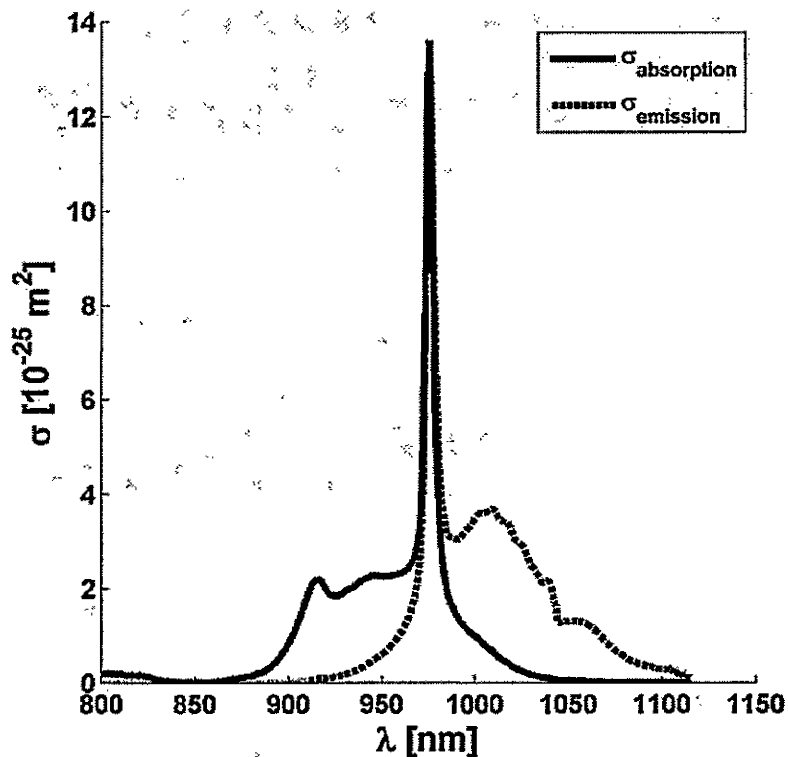


Figure 6-22 Absorption and emission cross-sections for a YDFA fabricated by CorActive Inc. Data points totaling 316 were provided by Morasse.

The role of the importer is to use the data set to generate the cross-section of absorption and emission for *any* wavelength. Even if this wavelength is not exactly one of the domain data points (but somewhere in between), the importer employs a cubic spline algorithm [37] to interpolate the necessary cross-sections for a set of wavelength bins. For the simulation, the peak wavelength was set to 1064.0 nm and 30 wavelength bins were requested within the wavelength boundaries of 1000 and 1100 nm such that one of the bin center wavelengths is 1064.0 nm. The importer returned a set of thirty wavelengths and their corresponding absorption and emission cross-sections as well as the width of the wavelength bins (Figure 6-23). The resulting wavelengths are designed so that they center 30 neighboring bins that exactly fit within the boundaries stated earlier.

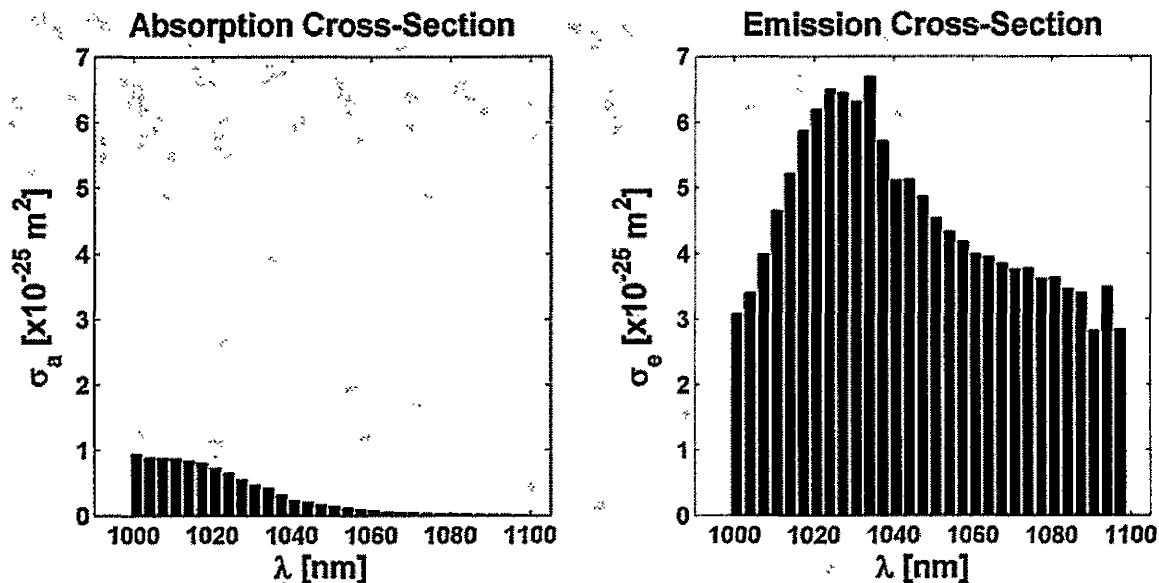


Figure 6-23 Absorption and emission cross-sections for 30 wavelength bins used in an MCP simulation. One wavelength bin is centered at 1064.0 nm and the bins are bounded by 1000 nm and 1100 nm as requested in the requirements specification.

For pulse repetition rates in the kHz regime, the MCP simulations modeling gain and ASE run up to a few minutes at most after which the system converges (i.e. output pulses remain unchanged with respect to power and dopant energy population concentrations). To verify Eichhorn's work, up to 500 consecutive nanosecond pulses (or 2 minutes of simulating) were needed before convergence occurred. Some fiber amplifier operating conditions can even have simulation convergence after a single pulse as shown in Figure 6-25 for a Ytterbium doped system. In general, the degree of resolution for nanosecond input pulses are high.

At MHz repetition rates, optical pulses are much more frequent. These pulses are typically ultra-short and in the laboratory experiment, have picosecond widths. To simulate such conditions, it is required that several hundred thousand pulses are needed to consecutively propagate down the fiber for numerical convergence. This numerical analysis was performed on a supercomputer and is discussed further in section 6.6.

For completeness, the MCP algorithm was verified with Wang's [32] article that models amplification of nanosecond pulses in Ytterbium-doped optical fiber for the case of a 20 W co-propagating pump at 915 nm. Table 6-5 provides the operating conditions used in the verification simulation. Note some comments in the third column that mention differences in the operating conditions used between this simulation and Wang's work.

In his article, Wang represents the electric field with respect to its energy. The total energy of a pulse $E_{PULSE}^{\pm}[\lambda]$ and its instantaneous power $P^{\pm}[\lambda, n]$ are related by the discretized equation:

$$E_{PULSE}[\lambda_k] = \sum_{n=0}^N P[\lambda_k, n] \Delta t \quad 6-15$$

The N power samples are defined on a finite range of time whose bounds are set to $\pm \text{PBC} \times \text{FWHM}$ (refer to section 2.2.2), and Δt is a time step for two neighboring pulse samples within this range. Numerically generating the Gaussian pulse with an input peak power of 47 W gives the required input pulse energy of $1 \mu\text{J}$. The total energy can also be related (approximately) to the peak power: $E_{PULSE} = P_{PEAK} \times \text{FWHM}$ which results in a value of 50 W. Since the quantitative and qualitative measurements are in good agreement, the peak power was set accordingly.

To reproduce the pulsed results, a simulation is completed for the pumping of the fiber, and with no input seed until the system is in steady state. A product of this operation is a set of dopant population energy densities converged to some nominal values. These are in turn used in the pulsed simulation as an alternative to the standard method of initializing the densities as discussed earlier in Section 3.9. The results of the steady state calculations utilizing the MCP algorithm are illustrated in Figure 6-24. To

achieve the 2 nm wavelength bin widths used by Wang for the simulation range 1020 nm to 1100 nm, 40 wavelength bins were selected.

Table 6-5 Parameters used for the MCP simulator for modeling a 10 kHz repetition rate pulsed operation in the co-propagating geometry for comparison to Wang's work [32].

Operating Parameter	Value	Description
PBC	2.5	Pulse Boundary Coefficient (Defined in section 3.2.2)
FWHM	20.0 ns	Full Width at Half Maximum
λ_s	1064.0 nm	Pulse Peak (Operating) wavelength
λ_p	915.0 nm	cw Pump Wavelength
$\sigma_{a,p}$	$7.45 \times 10^{-25} \text{ m}^2$	Absorption Cross-Section at the Pump Wavelength (<i>not</i> taken as $8.0 \times 10^{-25} \text{ m}^2$ from [32])
$\sigma_{e,p}$	$2.47 \times 10^{-26} \text{ m}^2$	Emission Cross-Section at the Pump Wavelength (<i>not</i> taken as $5.0 \times 10^{-26} \text{ m}^2$ from [32])
P_0	47 W	Seed (Gaussian) Pulse Peak Power
$P_{avg,ASE}$	0.0 mW	Seed Average ASE Power
P_p	20 W	Average Pump Power
L	10.0 m	Fiber Length
n_{SiO_2}	1.45	Silica (Background) Index of Refraction
$NSTEPS$	500	Fiber discretization (length divided by $NSTEPS - 1$)
ν_{rep}	10.0 kHz	Repetition Rate
σ_a	Figure 3.6 m^2	Absorption Cross-Section (<i>not</i> taken from [42])
σ_e	Figure 3.6 m^2	Emission Cross-Section (<i>not</i> taken from [42])
a	9.77 μm	Core Radius
A_p	$3.0 \times 10^{-8} \text{ m}^2$	Assuming Circular Shaped Inner-Cladding area
D	0.01	Pump Overlap Function
Γ	Equation 3-6	Signal Overlap Function (<i>not</i> taken as 0.85 from [32])
NA	0.046	Core numerical aperture
N_0	$6.0 \times 10^{25} \text{ m}^{-3}$	Dopant Concentration
τ	0.84 ms	Radiative relaxation time constant
M	1.0	Number of modes
α_s	0.003 m^{-1}	(Negligible) Background Signal loss
α_p	0.003 m^{-1}	(Negligible) Background Pump loss
No. pulses	1,2,3,...,10	Number of consecutive pulses
α_{RS}	0	Rayleigh Scattering Coefficient (<i>not</i> implemented)

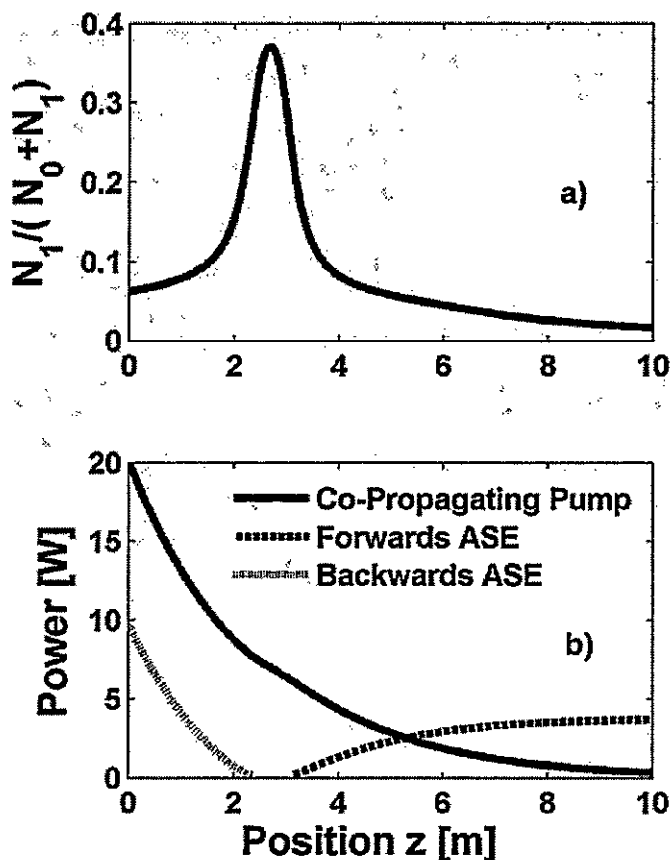


Figure 6-24 Steady-state MCP simulation results for a) the ratio of the excited to the total dopant energy population densities and b) the power distributions throughout the fiber. These results are based on operating conditions in Table 6-5 with zero input signals.

The steady state results are in good agreement with expected values. The maximum excited state to total concentration ratio of 0.37 units in Figure 6-24 a) is within an acceptable 10% to that reported by Wang. The difference is primarily due to the different cross-sections utilized in the simulations (refer to Table 6-5 for more details). With a slightly smaller excited state concentration distribution, the pulsed MCP results are expected to have slightly lower powers than expected. With this in mind, the pulsed results (Figures 6-25 and 6-26) are in very good agreement with Wang's simulations.

It is evident from this verification example that the outcome of the fiber amplification is not only dependent on the choice of dopant ions and pump power, but also the host material of the core. Cross-sections for Ytterbium fiber amplifiers with

different host materials can differ a great deal as illustrated by Zou's article [50]. Having a simulator to do modeling using all available cross-sections for a chosen dopant ion is most beneficial for experiments that require high power output.

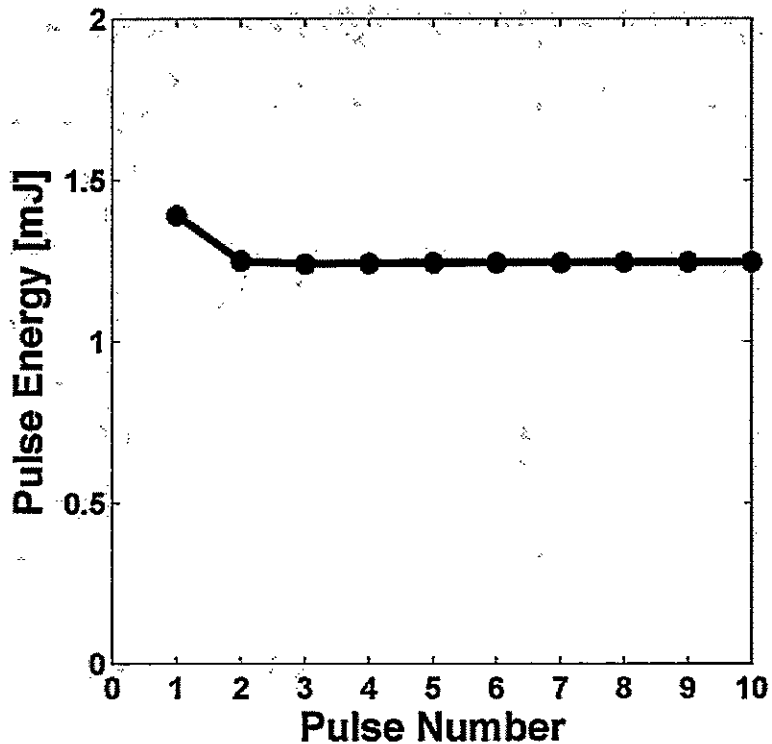


Figure 6-25 Output energies for the first 10 pulses. Convergence is clear after the second pulse propagates through the fiber.

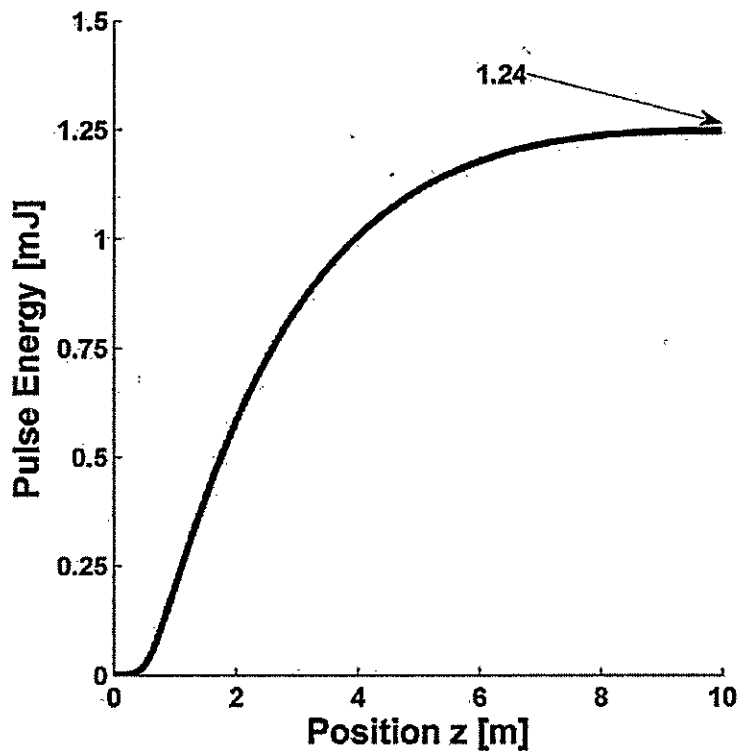


Figure 6-26 The pulse energy distribution of the output pulse after the simulation reaches convergence.

6.5 Verification of Power to Amplitude Algorithm

An experimental verification should be carried out for the power to amplitude algorithm (P2A discussed in Chapter 4) before proceeding to the final simulation of gain, ASE, GVD and SPM. It is this method that allows the algorithm to transfer from the power context (for gain and ASE calculations) to the amplitude context (for GVD, SPM and other passive calculations).

If the instantaneous input amplitude A_{in} is known (for a section of the fiber in question), and the gain constant has been calculated by means of the standard algorithm for simulation of gain and ASE (discussed in Section 3.9), then the output amplitude A_{out} from one neighboring junction to the next must theoretically satisfy $P_{out} = |A_{out}|^2$ (with all the phase information left intact), and this can be calculated, as proven mathematically in Chapter 4.

Errors in the algorithm due to incorrect mathematics and/or coding mistakes would be expected to accumulate throughout the numerical procedure as illustrated by the block diagram in Figure 6-27. Since the output pulse power from the exit fiber facet is known using the standard gain and ASE algorithm of section 3.9, one can compare such results to MCP simulations with identical operating conditions where both power and amplitude are propagated to the exit fiber facet (using the P2A to do so). An example of such a comparison is given in Figure 6-29 (with GVD and SPM turned off).

To make the comparison more rigorous, a nonlinear phase (Equation 6-16) has been added to the input Gaussian pulse. The nonlinear chirp (derivative of this phase) is illustrated in Figure 6-28.

$$\phi(\tau) = \left(\frac{18.1}{2T_0^2}\right)\tau^2 + \left(\frac{0.9}{2T_0^3}\right)\tau^3 + (-8.4)\exp\left(\frac{-\tau^2}{T_0^2}\right) \quad 6-16$$

Adding any kind of phase should not affect the absolute square of the amplitude (or in other words, the power). Even though adding chirp will provide some additional phase and therefore non-zero imaginary amplitude, this should not affect the absolute square of the amplitude function (i.e. $(r \exp(i\theta)) \times (r \exp(-i\theta)) = r^2 \forall \theta$). As the field propagates and gets amplified, the real and (non-zero) imaginary components get amplified according the P2A algorithm.

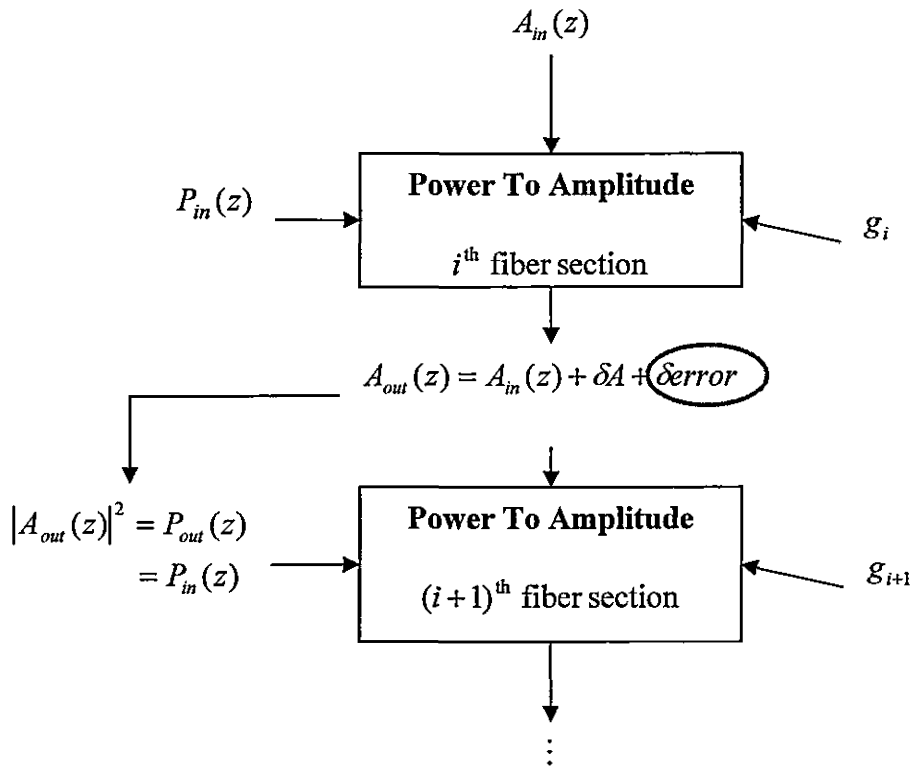


Figure 6-27 Error propagation occurs when an inaccurate output amplitude calculated from a previous fiber step is taken as the input amplitude to the next step. In the figure, $\delta error$ is sent as components of two inputs to the next P2A block. Refer to Chapter 4 for details on the algorithm.

The output absolute-square of the amplitude remained unchanged when comparing with an identical MCP simulation without any input chirp - verifying this fact.

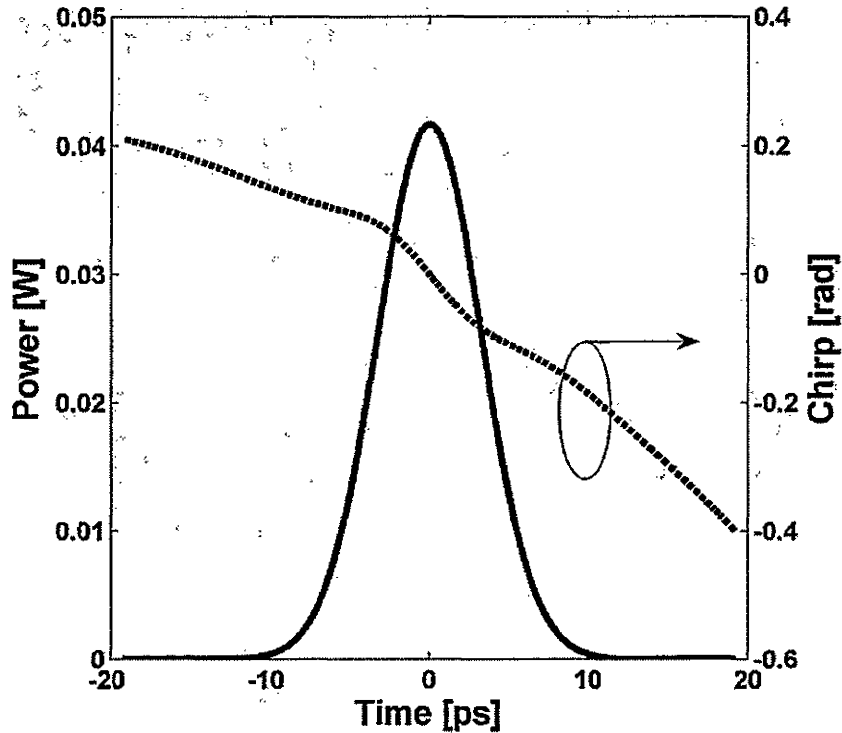


Figure 6-28 Input pulse power (solid line, left scale) and its nonlinear chirp (dashed line, right scale) used in the verification of the P2A algorithm.

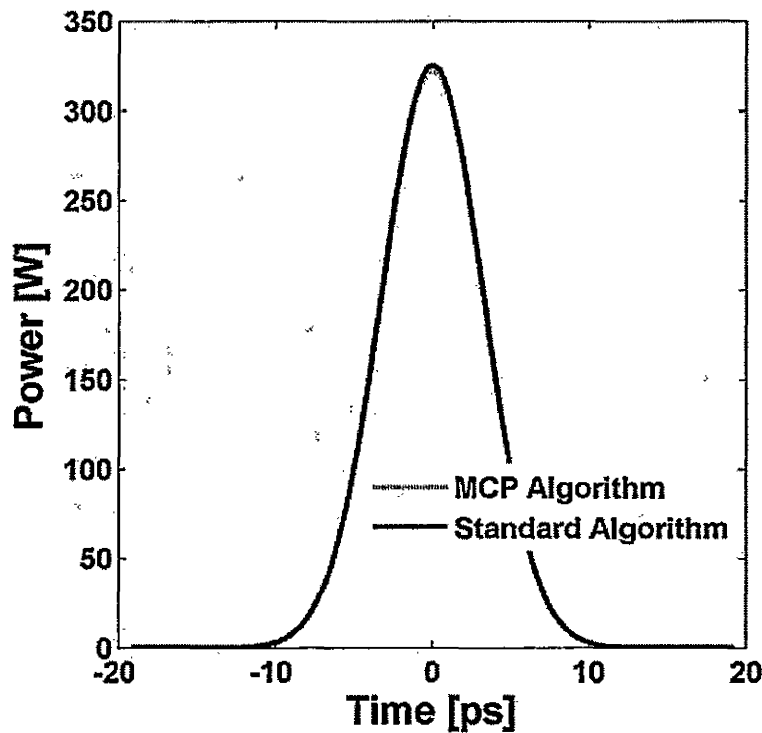


Figure 6-29 Output pulse power results for gain and ASE calculations comparing the MCP simulator where P2A is utilized to the standard power propagation algorithm (which does not use P2A).

From the figure above, the pulse power outputs from the standard gain and ASE algorithm and MCP simulations are virtually identical. The maximum error found at the peak of the power distribution was within 0.9%. This small error is mainly due to some assumptions made in the P2A as discussed in Section 4.2. This makes available the capability of analyzing the amplitude instead of the power function. It is reasonable to assume that the P2A algorithm is running as designed.

6.6 Pulsed Simulation Results Accounting gain, ASE, GVD and SPM

The algorithm that incorporates gain, ASE, GVD and SPM is very computationally intensive for the experimental laboratory conditions. Spatial and temporal resolutions must be as high as possible for convergence to occur. During the development process, it was decided that the simulator would run gain and ASE (i.e. active) calculations until the dopant energy density populations would converge to some nominal values. Then a further simulation would be made with both active and passive components turned on, starting at the set of dopant energy population densities extracted from the converged active simulation. The convergence of a simulation is measured by comparing the dopant population densities after each pulse has been transmitted through the fiber amplifier. Usually a converged result would mean a change of less than 1% from pulse to pulse.

The two-step approach is taken due to the high computational requirements of the passive calculations that as a result take orders of magnitude longer to compute per pulse compared to the active simulations alone. With hundreds of thousands of pulses to simulate, it is simply not realistic to run both components at all times.

For the active calculations, not only is the resolution in time very high, but also, the spatial resolution is increased to $NSTEPS = 500$ (where earlier Tm:ZBLAN pulsed simulation benchmarks had the same time resolutions but a lower number of spatial steps). Moreover, it turns out that an increase in time resolution increases central processing unit (CPU) usage while an increase in spatial resolution requires an increase in memory. So much memory was required that it was no longer viable to execute these simulations on a desktop computer.

6.6.1 Active Simulations on SHARCNET

A version of the MCP simulator was programmed for a UNIX operating environment in order to be used on the SHARCNET supercomputing facility. For the simulations, a cluster with 4 x Opteron 2.40 GHz CPU and 32 GB memory was accessible. This system was sufficient for our purposes. The new software has the capability to execute the power propagation calculations simultaneously via threading technology available in C++. It turns out that numerical calculations can be performed for: 1) forward and backward signal, 2) ASE and 3) pump powers simultaneously as they are mutually exclusive calculations once the dopant energy population densities are set at the beginning of a time-step. This decreased the processing time some more.

The simulation conditions for the laboratory are provided in Table 6-6. After 22 days of simulation of gain and ASE on SHARCNET, the output pulses begin to converge with peak powers at 325 W as shown in Figure 6-30. A measurement for the output average power was taken by Andrew Budz as 1.39 W.

Table 6-6 Parameters used for the MCP simulator in modeling 577 MHz pulsed operation in the counter-propagating geometry.

Operating Parameter	Value	Description
PBC	2.5	Pulse Boundary Coefficient (Defined in section 3.2.2)
FWHM	7.7 ps	Full Width at Half Maximum
λ_s	1075.0 nm	Pulse Peak (Operating) wavelength
λ_p	975.0 nm	cw Pump Wavelength
$\sigma_{a,p}$	$2.64 \times 10^{-24} \text{ m}^2$	Absorption Cross-Section at the Pump Wavelength
$\sigma_{e,p}$	$2.38 \times 10^{-24} \text{ m}^2$	Emission Cross-Section at the Pump Wavelength
P_0	0.043 W	Seed (Gaussian) Pulse Peak Power
$P_{avg,ASE}$	0.0 mW	Seed Average ASE Power
P_p	2.11 W	Average Pump Power
L	14.8 m	Fiber Length
n_{SiO_2}	1.45	Silica (Background) Index of Refraction
$NSTEPS$	500	Fiber discretization (length divided by $NSTEPS - 1$)
ν_{rep}	577.0 MHz	Repetition Rate
σ_a	Figure 3.6 [m^2]	Absorption Cross-Section
σ_e	Figure 3.6 [m^2]	Emission Cross-Section
a	3.0 μm	Core Radius
A_p	$1.46 \times 10^{-8} \text{ m}^2$	Hexagonal-Shaped Inner-Cladding area
D	0.0019	Pump Overlap Function $\pi a^2 / A_p$
NA	0.13	Core numerical aperture
N_0	$1.0 \times 10^{26} \text{ m}^{-3}$	Dopant Concentration
τ	1.5 ms	Radiative relaxation time constant
M	1.0	Number of spatial modes
PA	8.0 degrees	Fiber facet polishing angle
α_s	$2.30 \times 10^{-4} \text{ m}^{-1}$	(Negligible) Background Signal loss
α_p	$2.30 \times 10^{-4} \text{ m}^{-1}$	(Negligible) Background Pump loss
A_{eff}	$39.12 \times 10^{-12} \text{ m}^2$	Effective Area (πw_s^2)
β_2	$15.0 \times 10^{-27} \text{ s}^2/\text{m}$	GVD parameter
n_2	$2.2 \times 10^{-20} \text{ m}^2/\text{W}$	SPM parameter
No. pulses	260,000	Number of consecutive pulses

One can perform a rough calculation for the pulse peak power according to the following equation:

$$\frac{P_{AVG}}{\nu_{rep}} = P_{PEAK} \times FWHM \quad 6-17$$

Taking $FWHM = 7.7\text{ps}$, $P_{AVG} = 1.39$ and $\nu_{rep} = 577\text{MHz}$ we get $P_{PEAK} = 310.6\text{W}$. This differs by approximately 15.0W ($\sim 5\%$) from simulation results for a number of reasons. First, Equation 6-17 is not accurate as it assumes square pulses. Secondly, the pulse width must necessarily equal some effective width that is not the FWHM or the RMS full-width. Finally, the simulation has not included any passive effects such as GVD or SPM, which contribute significant changes to the output pulse-widths.

These results are already substantial as they verify that the standard method of gain and ASE can also be used to simulate ultra-short picosecond pulses as all related articles found discuss the simulation in the nanosecond regime.

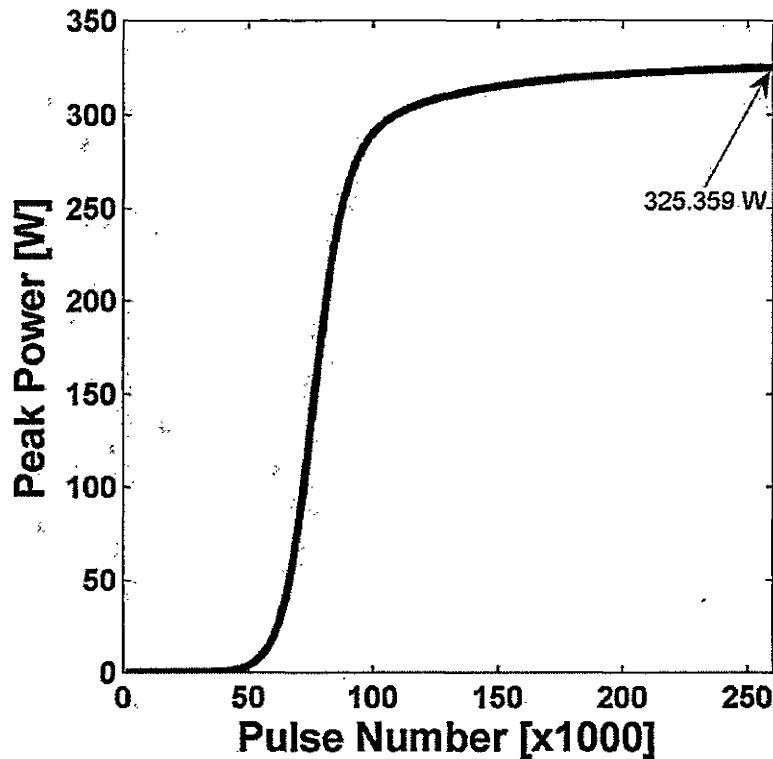


Figure 6-30 Peak powers for the first 260000 pulses of a gain and ASE (active) simulation run on SHARCNET for the operating conditions provided in Table 6-6. The 'S' curve indicates that the simulation is converging with peak powers approaching to about 325 W. This simulation took approximately 22 days to process on the SHARCNET supercomputer.

In the following subsections, passive effects will be considered in the simulations. If one is concerned only with powers, and the pulse bandwidth is moderate such that the emission and absorption cross-sections remain almost uniform for the majority of the wavelengths within the bandwidth of the pulse, then the standard gain and ASE simulation is sufficient.

6.6.2 Active and Passive Simulation of Unchirped Input Gaussian Pulses

As mentioned in the previous section, 260000 pulses were propagated in an active-only simulation. The converged dopant population densities for all 499 sections of the fiber were taken as the initial dopant population densities in the following experiments. Also, note that all the simulation operating conditions in Table 6-6 are applied here as well.

Hitherto, it is difficult to ascertain the correctness of the simulation results discussed as no benchmark-worthy articles have been found relating to the modeling of this nature. However, there are certainly some results that will indicate the software is *not* running properly. For example, in Section 5-3, pulse aliasing was discussed for simulations that incorporate gain and GVD. For the first (or 260001st) pulse to be amplified, GVD requires that the amplitude for all the time steps – future and past, are provided. Before the amplitude is sent for GVD computations, it gets amplified. The gain used for all future time steps (or those time steps after the current time) are taken from the previous pulse (from the active-only simulation) as discussed in Section 5-3. This is done because there is no way of predicting what those values will become. These “future” gain values are not necessarily seamless from those values generated (for the current pulse) from the first time step $\tau = 0$ up to the current time step (inclusive). Hence,

a discontinuous gain can occur at *any* time leading to significant aliasing after GVD processing.

Fortunately, such strange results have not been observed, and the results appear to converge after a number of pulses for the active and passive simulation. With GVD and SPM included in the simulation, the results are not significantly different from SHARCNET results discussed in the previous section.

In the following, the input Gaussian is not given an input chirp. Those results are presented in the following section. With that in mind, Figure 6-31 illustrates the output pulse time and wavelength domain pulse powers for $N = 2048$ and $N = 512$ time samples with $PBC = 2.5$ and $PBC = 20.0$ respectively:

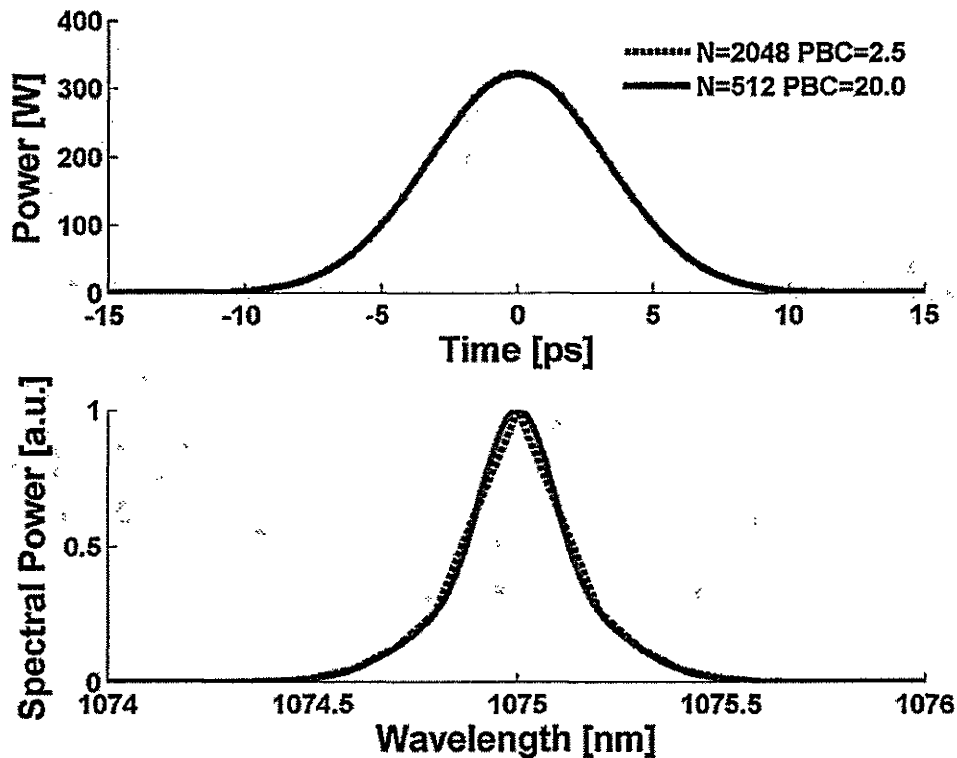


Figure 6-31 Output power and normalized power spectrum for two different time (N & PBC) resolutions. The output power spectrum for $N=512$ is much more resolved than the one for $N=2048$. Simulation operating times were 18.5 minutes for $N=2048$ and 1.0 minute for $N=512$.

Two different operating pairs of pulse time resolution (N) and pulse boundary coefficients (PBC) were simulated to see whether or not the outputs do in fact converge to the same results when resolution is increased in the wavelength domain and decreased the time domain. From the time-frequency uncertainty principle, decreasing the time domain resolution will increase the frequency domain resolution. It is clear from Figure 6-31 that the overall results are the same. However the energy is resolved less in the wavelength domain for $N=2048$ and in the time domain for $N=512$ respectively.

The purpose of this exercise was to implement a simulation using the original SHARCNET dopant energy population density results but with higher resolution in the wavelength domain, a necessary step for accurate GVD calculations. Both peak powers result in a power of 321.7 W. It is slightly lower than the active-only output (SHARCNET) power of 325.4 W and this clearly shows that the GVD and SPM do not corrupt the calculations when converting from the active-only SHARCNET simulation to an active/passive simulation.

Two conclusions were made from this exercise. First, the conversion from active to active/passive simulations is seamless (after comparing instantaneous output powers) provided that the active-only simulation is converged. Secondly, a resolution swap between time and frequency domains can be made without any significant change in results provided that the new resolutions do not contradict the Nyquist sampling rate.

Earlier, it was mentioned that the pulses “appear” to converge to some static results. Carrying on the simulation to 50 more pulses showed a very small increase in pulse powers with the final pulse having a peak power difference of 1% from the first output pulse of the series. It would be a good idea to simulate several hundred more

pulses at the minimum, to make sure that the results remain converged. However, due to the high computational requirements of this process and the limited research time available, this was left for the simulation in the next section where the input pulse is given an initial chirp, a realistic and necessary addition to the modeling procedure.

6.6.3 Active and Passive Simulation of Chirped Input Gaussian Pulses

Up to this point, the unchirped and simulated input spectrum has differed significantly from that which was measured by my colleague Andrew Budz (Figure 6-32 solid-line). This is due primarily to the disregard of the input chirp. The experimental measurement was made for nonlinearly chirped input pulses and the residual chirp is due to the mode-locking process of the oscillator. The input chirp may have a big part in the amplification process, and should be considered in the simulation for reasonable comparisons to the experimental results. Lacking this input spectral information, the propagating pulses would not follow the same GVD and SPM processes in addition to gain and ASE as do the real-life laboratory seed pulses in highly dispersive conditions.

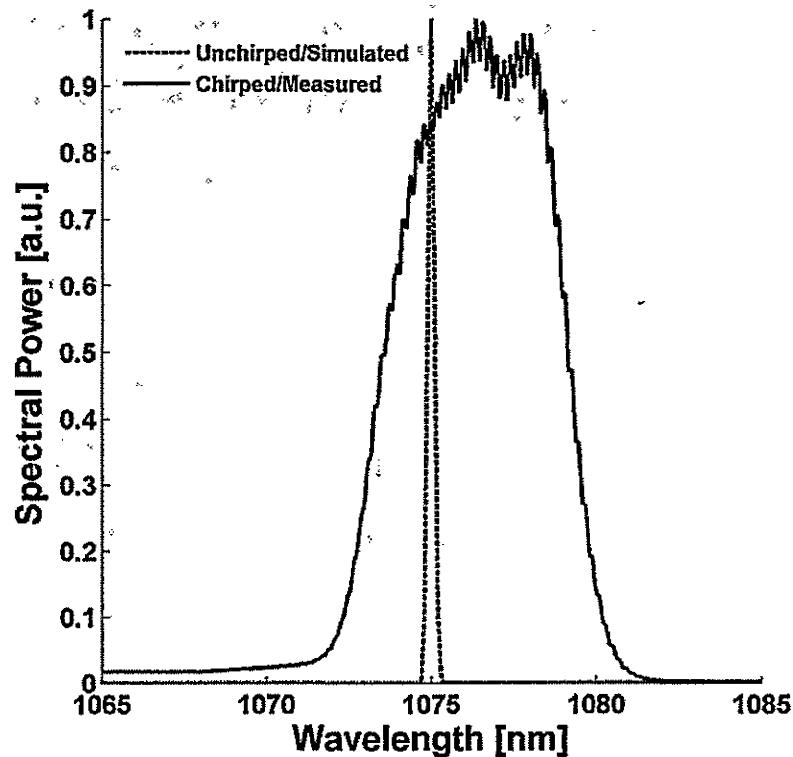


Figure 6-32 Input seed spectra for an unchirped simulated pulse (dashed line) and the chirped measured pulse (solid line) by Andrew Budz.

For any realistic results, the design of the input chirp must be taken in the simulation. It is certain, given that the diode seed laser is operating in a passively mode-locked regime, that the pulse is positively chirped as discussed earlier in Section 5.1. Higher order and nonlinear chirps have also been considered in the modeling.

To begin, one will notice from Figure 6-32 above that the peak wavelengths do not coincide with one another, and are separated by approximately 1.4 nm in wavelength. Therefore, the first component of the custom chirp is a constant frequency shift $\Delta\omega$ rad. This frequency shift is directly proportional to the wavelength shift $\Delta\lambda$ and is solved to be $\Delta\omega = 2.282 \times 10^{12}$ rad.

After some trial and error, the customized input chirp on the seed Gaussian pulses is given by the derivative of Equation 6-18. Note that this is a rough approximation. The

generation of an accurate chirp function is left as future work for an asymmetric Gaussian seed instead of a purely Gaussian one. The diode output pulses are asymmetric due to the nature of the gain and saturable absorption mechanisms when operating in the passive regime (refer to Section 5.2 for more details). The custom phase whose derivative is the custom chirp is defined up to third order followed by a nonlinear (exponential) component:

$$\phi(\tau) = -\Delta\omega_0\tau + \left(\frac{-C}{2T_0^2}\right)\tau^2 + \left(\frac{G}{2T_0^3}\right)\tau^3 + F \exp\left(\frac{-\tau^2}{T_0^2}\right) \quad 6-18$$

Setting $C=18.4$ (positive linear chirp), $F=-2.4$, and $G=-1.0$ produces an acceptable approximation as illustrated in Figure 6-33.

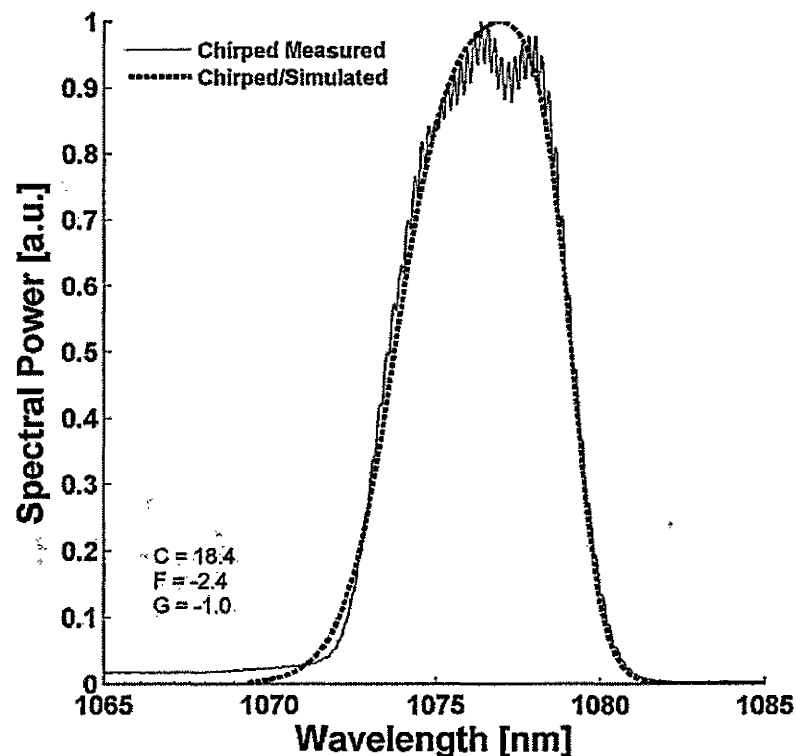


Figure 6-33 Theoretical chirped input seed spectrum (dashed line) utilizing the chirp function from Equation 6-19 has the same approximate distribution as that measured by Andrew Budz (solid line) from experiment.

The measured output spectrum of the fiber amplified pulse was also provided by Andrew Budz and is used to compare to simulation results. The chirp design is not a unique solution. It is quite arbitrary as long as a decent spectral agreement can be obtained with a predominantly linear blue-chirp that is observed experimentally.

Input seed measurements including the spectra illustrated in the above figure are for a 4.2 ps pulse calculated from an autocorrelation trace and assuming a sech^2 power distribution. The experimental conditions do not exactly match those prescribed in Table 6-6 for the operating conditions of this simulation. In particular, the simulated seed pulse width is 7.7 ps, which has been kept for legacy reasons¹. Since temporal pulse widths can range from 2 to 8 ps [56] for the diode laser oscillator source, one may expect that the spectrum of the input seed does not differ much (at least qualitatively) for seed pulse widths between 4.2 and 7.7 ps.

The simulated (complex valued) spectrum for the seed pulse must be defined as close as possible to the laboratory measurements. For the chirped input pulse, the seed and amplified pulse spectra (measured and simulated) are illustrated in Figure 6-34 (left plot).

After amplification, both measured and simulated spectra increase in linewidth, with a change of 0.7 nm and 0.5 nm respectively. The differences probably arise from an incomplete input chirp design. In addition, the simulated seed envelope is wider (by 3.5 ps), leading to a slightly different frequency domain linewidth, and hence to similar

¹ Simulation for 7.7 ps pulses took almost a month to compute, and this FWHM decision was made based on the experimental data available at the time. Unfortunately, there was not enough time remaining to make another gain and ASE computation for a 4.2 ps pulse train with all other operating conditions unchanged.

differences in requirements on the input chirp in order to achieve the same linewidth as that spectrum measured for a 4.2 ps pulse. Also, by using a longer pulse in simulation, the peak intensities are no longer equal. Therefore there will be less SPM occurring in the simulator. However, given the input intensities are fairly modest and the pulses are highly chirped, SPM should not be a very dominant effect in both the experiment and the simulation.

In section 6.6.2, a drop of just under 4 W in signal peak power occurred when calculations were switched from an active-only simulation to the active and passive simulation. In that case, no input chirp was considered and the results (at least in the time-domain) were in good agreement with measurements. The same switch after including input chirp with all other variables set identically resulted in a larger peak power drop. When adding the input chirp whose phase is defined by Equation 6-18 onto the 7.7 ps seed, the amplified output peak power drops by about 65 W (~20%) as shown in Figure 6-35 with peak powers converging to approximately 272 W corresponding to an average power of 1.59 W. The average power is 12% higher than the measured average power of 1.39 W. In section 6.4.2, it was pointed out that a last minute change in the relaxation time constant from 1.5 ms to 800 μ s explained this higher average power in the cw regime. One could expect that with a more refined value of τ , the discrepancy between the pulsed results and the pulsed simulations would be smaller, as is indicated by the cw simulations shown in Figure 6-8. Taking Fresnel's losses into account corresponds to an expected average power of 1.53 W (instead of 1.59 W). This value is closer to the experimental measurement than the result of a cw regime simulation described in Section 6.4.2 above for a relaxation time constant of 1.5 ms.

The amplified output spectrum of the simulated pulse seems to fit the measured spectrum well as shown in Figure 6-34. The only uncertainty in results arises with the amplified peak power. Earlier, it was mentioned that 7.7 ps pulses were set for legacy reasons. At the time, it was assumed that due to some qualitative calculations that 7.7 ps would be a common (or average) width for the seed pulses. It had already taken 22 days for an active-only simulation to process 260000 pulses. Unfortunately there was not enough time for the same simulation of 4.2 ps pulses. The input chirp design for such a simulation keeping the formalism of Equation 6-18 may still be valid; however it is left for future work.

As long as the input chirp is predicted properly, it is possible to hypothesize that the simulator, capable of modeling active and passive effects simultaneously, can be used for complex amplification of ultra-short optical pulses in a YDFA.

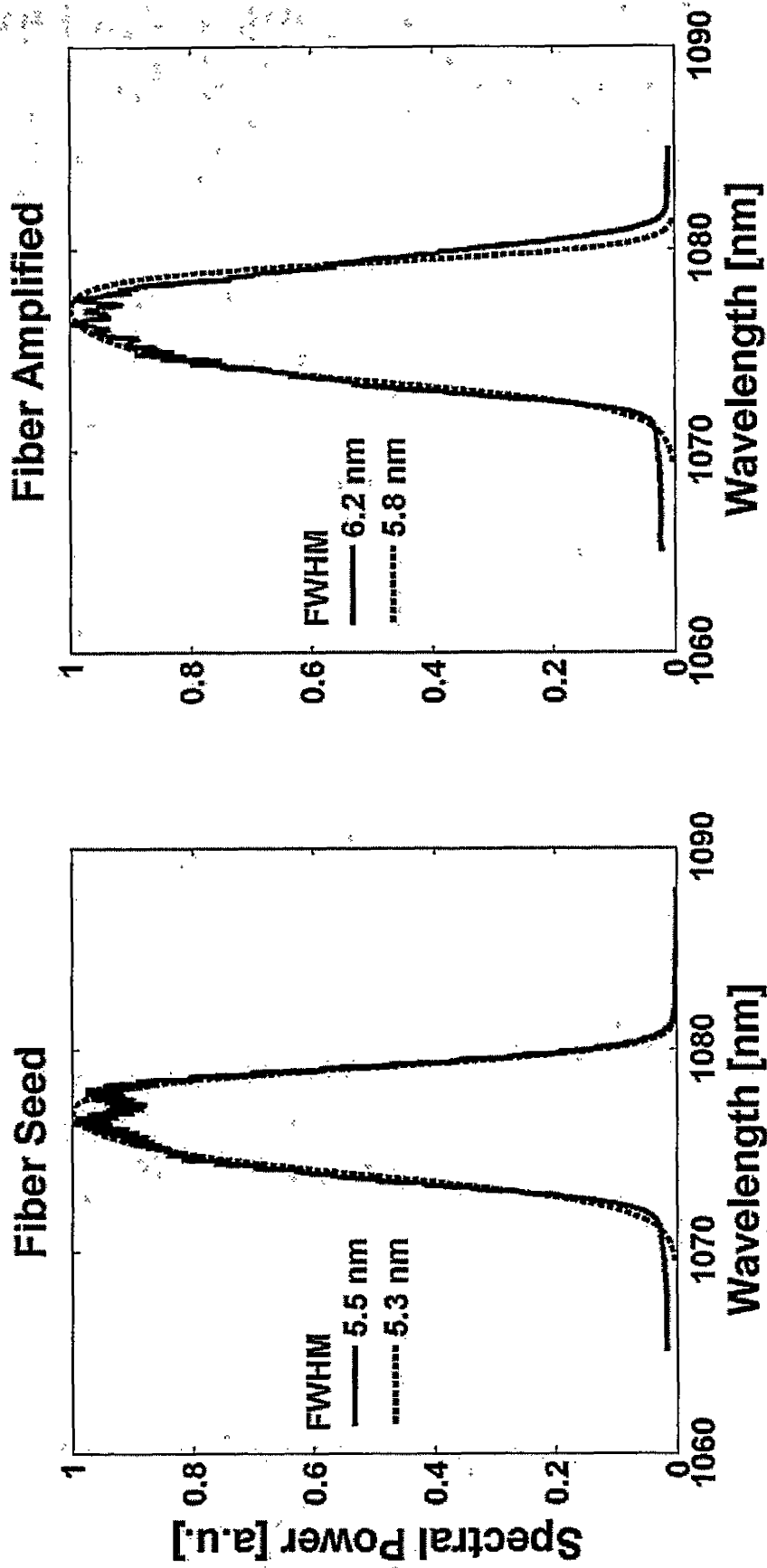


Figure 6-34 Pre and Post amplification pulse spectra normalized to unity. The left graph is compared the power spectrum of the input seed (measured and simulated) to that of the output amplified pulse in graph to the right. An increase in both cases for the linewidth FWHM is observed.

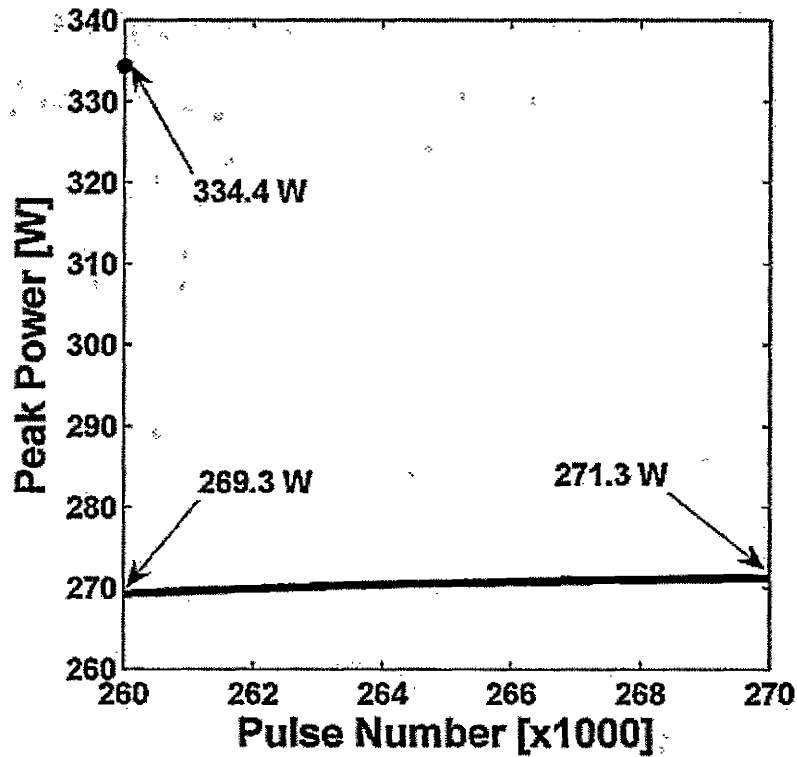


Figure 6-35 Active and passive simulation of 10000 pulses after active-only simulation of 260000 pulses. The first data point is the last peak power from the previous 260000 pulses from an active-only simulation described in Section 6.6.1. These are output powers before Fresnel's losses are taken into account.

7 Future Work

There is still much to do in this work with applications that can branch in numerous directions. Many short topics have been discussed with an emphasis on future implementations. However, there are two main subjects that interest me the most. These are multiple signal amplification for difference frequency generation (DFG) experiments, and the prediction of parabolic pulse generation. All other topics shall be implemented in a predefined order of importance based on need for the proper modeling of these two topics.

DFG generation in a nonlinear crystal after amplification is a desired experiment in the ultra-fast laser lab for the diode laser project. An experimental setup is currently being built that incorporates two tunable diode laser seed sources similar to the MOPA setup illustrated in Figure 1-1. Since the experimental diode lasers are tunable from 1030 to 1090 nm, the DFG experiment can be used to achieve output pulse-trains at peak wavelengths in the mid to far infrared. The simulator is currently being re-written and redesigned so that an arbitrary number of signals (cw or pulsed) can be launched into either of the fiber facets.

Propagation of input parabolic pulses has been investigated using the split-step Fourier method [65]. In that analysis, the positive gain could only be set to a constant value throughout space and time (just like background absorption) due to the limitations

of the SSFM. With our numerical tool that facilitates a dynamic gain throughout the fiber for all of time simulations combining gain, ASE, GVD and SPM will be compared to previous works for benchmarking of simplified experimental cases. Further research will go into the prediction of operating conditions necessary for parabolic pulse amplification to produce transform limited fiber amplified pulse trains for a selection of widely used fiber amplifiers.

It is expected that this technology will be useful in the design phase of all fiber amplification experiments and product lines. With the increased complexity of present day optical circuits, optimization can save much time in the research and development phases and lead to exciting innovations.

References

- [1] R.W. Boyd, "Nonlinear Optics", Academic Press, 2003
- [2] N. Moloney, "Nonlinear Optics", Addison Wesley, 1992
- [3] G.P. Agrawal, "Nonlinear Fiber Optics", 2nd Edition, Academic Press, 1995
- [4] D.J. Griffiths, "Introduction To Quantum Mechanics", Prentice Hall, 2005
- [5] J.C. Palais, "Fiber Optic Communications", Prentice Hall, 2005
- [6] G.R. Fowles, "Introduction to Modern Optics", Dover, 1975
- [7] S. Haykin, "Signals and Systems", John Wiley & Sons Canada, Ltd., 2003
- [8] M. Eichhorn, "Numerical Modeling of Tm-Doped Double-Clad Fluoride Fiber Amplifiers", *IEEE J. Quantum Electron.* Vol. **41**, No. 12, pp. 1574-1581, (2005)
- [9] M.J. Brennan, *et al.*, "Ultrashort Optical Pulse Generation with a Mode-Locked Long-Wavelength (1075-1085 nm) InGaAs-GaAs Semiconductor Laser", *IEEE Photon. Technol. Lett.* Vol. **16**, No. 8, pp. 1798-1800, (2004)
- [10] P.W. Milonni and J.H. Eberly, "Lasers", John Wiley & Sons, Inc., 1988
- [11] C.H. Henry, "Theory of Spontaneous Emission Noise in Open Resonators and its Application to Lasers and Optical Amplifiers", *J. Lightwave Technol.* Vol. **LT-4**, No. 3, pp. 288-297, (1986)
- [12] A. Hardy and R. Oron, "Signal Amplification in Strongly Pumped Fiber Amplifiers", *IEEE J. Quantum Electron.* Vol. **33**, No. 3, pp. 307-313, (1997)

- [13] P.R. Morkel and R.I. Laming, "Theoretical modeling of erbium-doped fiber amplifiers with excited-state absorption", *Opt. Lett.*, Vol. 14, No. 19, pp.1062-1064, (1989)
- [14] P. Dupriez *et al.*, "High Average Power, High Repetition Rate, Picosecond Pulsed Fiber Master Oscillator Power Amplifier Source Seeded by a Gain-Switched Laser Diode at 1060 nm, *IEEE Phot. Tech. Lett.*, Vol. 18, No. 9, pp.1013-1015, (2006)
- [15] R. Eisberg and R. Resnick, "Quantum Physics Of Atoms, Molecules, Solids, Nuclei, And Particles", John Wiley & Sons, Inc., (1985)
- [16] D.A. Neamen, "Semiconductor Physics And Devices", McGraw-Hill, 2003
- [17] C.R. Giles and E. Desurvire, "Modeling Erbium-Doped Fiber Amplifiers", *J. Lightwave Technol.*, Vol. 9, No. 2, pp.271-283, (1991)
- [18] S.D. Jackson and T.A. King, "Theoretical Modeling of Tm-Doped Silica Fiber Lasers", *J. Lightwave Technol.*, Vol. 17, No. 5, pp.948-956, (1999)
- [19] D. Gloge, "Weakly Guiding Fibers", *Appl. Opt.*, Vol. 10, No. 10, pp. 2252-2258, (1971)
- [20] G. Xia, *et al.*, "Light propagation in the multi-mode double-clad erbium: ytterbium co-doped fiber: theory and experiment", *Opt. and Laser Technol.*, Vol. 36, pp.273-277, (2004)
- [21] A. Liu and K. Ueda, "The absorption characteristics of circular, offset, and rectangular double-clad fibers", *Opt. Commun.*, Vol. 132, pp.511-518, (1996)
- [22] K. Yelen *et al.*, "Experimentally Verified Modeling of Erbium-Ytterbium Co-Doped DFB Fiber Lasers", *J. Lightwave Technol.*, Vol. 23, No. 3, pp.1380-1392, (2005)

- [23] R.H. Stolen and C. Lin, "Self-Phase Modulation in Silica Optical Fibers", *Phys. Rev. A*, Vol. 17, pp.1448-1453, (1978)
- [24] F. Brunet *et al.*, "A simple Model Describing Both Self-Mode Locking and Sustained Self-Pulsing in Ytterbium-Doped Ring Fiber Lasers", *J. Lightwave Technol.*, Vol. 23, No. 6, pp.2131-2138, (2005)
- [25] X. Liu and B. Lee, "A Fast Method for the Nonlinear Schrödinger Equation", *IEEE Photon. Technol. Lett.*, Vol. 15, No. 11, pp. 1549-1559 (2003)
- [26] G. Bosco *et al.*, "Suppression of Spurious Tones Induced by the Split-Step Method in Fiber Systems Simulation", *IEEE Photon. Technol. Lett.*, Vol. 12, No. 5, pp.489-491 (2000)
- [27] O. V. Sinkin *et al.*, "Optimization of the split-step Fourier method in modeling optical-fiber communications systems", *J. Lightwave Technol.*, Vol. 21, No. 1, pp.61-68, (2003)
- [28] P. Dumais, *et al.*, "Enhanced self-phase modulation in tapered fibers", *Opt. Lett.*, Vol. 18, No. 23, pp.1996-1998, (1993)
- [29] Q. Cao and S. Chi, "Approximate Analytical Description for Fundamental-Mode Fields of Graded-Index Fibers: Beyond the Gaussian Approximation", *J. Lightwave Technol.*, Vol. 18, No. 1, pp.54-59, (2001)
- [30] S.C. Pinault and M.J. Potasek, "Frequency broadening by self-phase modulation in optical fibers", *J. Opt. Soc. Am. B*, Vol. 2, No. 8, pp.1318-1319, (1985)
- [31] C.R. Giles *et al.*, "Transient gain and cross talk in erbium-doped fiber amplifiers", *Opt. Lett.*, Vol. 14, pp.880-882, (1989)

- [32] Y. Wang and H. Po, "Dynamic Characteristics of Double-Clad Fiber Amplifiers for High-Power Pulse Amplification", *J. Lightwave Technol.*, Vol. **21**, No. 10, pp.2262-2270, (2003)
- [33] A. J. Budz and H.K. Haugen, "Wavelength and Repetition-Rate Tunable Mode-Locked Semiconductor-Seed-Source for Yb-Fiber-Amplifier Systems", Submitted to IEEE PTL, (2007)
- [34] J. Limpert *et al.*, "High-average-power femtosecond fiber chirped-pulse amplification system", *Opt. Lett.*, Vol. **28**, No. 20, pp.1984-1986, (2003)
- [35] H.M. Pask *et al.*, "Ytterbium-Doped Silica Fiber Lasers: Versatile Sources for the 1-1.2 μm Region", *IEEE J. Selected Topics Quant. Electron.*, Vol. **1**, No. 1, pp.2-13, (1995)
- [36] B. Morasse, "Amplificateur Á Fibre Double Gaine Codopée Á L'Erbium Et L'Ytterbium: Modélisation et vérification expérimentale", *Thesis M. Sc.*, University of Laval, (2005)
- [37] C. F. Van Loan, "Introduction to Scientific Computing", Prentice Hall, 2000
- [38] I. Kelson and A. Hardy, "Strongly pumped fiber lasers", *IEEE J. Quantum Electron.* Vol. **34**, No. 9, pp.1570-1577, (1998)
- [39] A. Ankiewicz and F. F. Rühl, "Effect of dopant distribution on optimization of Pr-doped fibre amplifiers", *Opt. and Quantum. Electron.* Vol. **26**, pp. 987-993 (1994)
- [40] B.M. Walsh and N.P. Barnes, "Comparison of Tm:ZBLAN and Tm:silica fiber lasers; Spectroscopy and tunable pulsed laser operation around 1.9 μm ", *Appl. Phys. B*, Vol. **78**, pp.325-333, (2004)

- [41] M. Eichhorn, "High-gain Tm-doped fluoride fiber amplifier", *Opt. Lett.*, Vol. **30**, No. 5, pp.456-458, (2005)
- [42] R. Paschotta *et al.*, "Ytterbium-Doped Fiber Amplifiers", *IEEE J. Quant. Electron.* Vol. **33**, No. 7, pp.1049-1056, (1997)
- [43] L. Cohen, "Time-Frequency Analysis", Prentice Hall Signal Processing Series, 1994
- [44] S. Carroll, "Spacetime and Geometry", Addison Wesley, 2004
- [45] R. Paschotta *et al.*, "Lifetime quenching in Yb-doped fibres", *Opt. Commun.*, Vol. **136**, pp.375-378, (1997)
- [46] Z. Burshtein *et al.*, "Impurity Local Phonon Nonradiative Quenching of Yb³⁺ Fluorescence in Ytterbium-Doped Silicate Glasses", *IEEE J. Quant. Electron.* Vol. **36**, No. 8, pp.1000-1007, (2000)
- [47] M.E. Fermann *et al.*, "Generation and propagation of high-power parabolic pulses in optical fibers", CLEO 2000 Technical Digest, Tops Vol. **39**, IEEE Cat. No. 00CH37088, pp.21-22, (2000)
- [48] R.L. Fork *et al.*, "Negative dispersion using pairs of prisms", *Opt. Lett.*, Vol. **9**, No. 5, pp.150-152, (1984)
- [49] B.C. Stuart *et al.*, "Chirped-Pulse Amplification in Ti:Sapphire Beyond 1 μm ", *IEEE J. Quant. Electron.* Vol. **31**, No. 3, pp.528-538, (1995)
- [50] X. Zou and H. Toratani, "Evaluation of spectroscopic properties of Yb³⁺-doped glasses", *Phys. Rev. B*, Vol. **52**, No. 22, pp.889-897, (1995-II)
- [51] A. Yariv, "Quantum Electronics", John Wiley & Sons Inc., 1989

- [52] M. Schell *et al.*, "Chirp of passively and actively mode-locked semiconductor lasers", *Appl. Phys. Lett.*, Vol. 67, No. 13, pp.1797-1799, (1995)
- [53] B. Yellampalle *et al.*, "Unambiguous chirp characterization using modified-spectrum auto-interferometric correlation and pulse spectrum", *Opt. Express*, Vol. 14, No. 14, pp.8890-8899, (2006)
- [54] B. Adhimalam *et al.*, "Wavelength-Tunable Short-Pulse Diode-Laser Fiber-Amplifier System Around 1.06 μm ", *IEEE Photon. Technol. Lett.*, Vol. 18, No. 7, pp.838-840, (2000)
- [55] P. Dennery and A. Krzywicki, "Mathematics For Physicists", Dover Publications, Inc., 1995
- [56] A. J. Budz *et al.*, "Ultrashort Pulses From a Mode-Locked Diode-Oscillator Yb-Fiber-Amplifier System", *IEEE Photon. Technol. Lett.*, Vol. 19, No. 2, pp.94-96, (2007)
- [57] G. Chang *et al.*, "Power scalable compact THz system based on an ultrafast Yb-doped fiber amplifier", *Opt. Express*, Vol. 14, No. 17, pp.7909-7913, (2006)
- [58] J. Ahn *et al.*, "Terahertz waveform synthesis via optical rectification of shaped ultrafast laser pulses", *Opt. Express*, Vol. 11, No. 20, pp.2486-2496, (2003)
- [59] R.J. Mears *et al.*, "Low-noise Erbium-doped fibre amplifier at 1.54 μm ", *Electron. Lett.*, Vol. 23, pp.1026-1028, (1987)
- [60] S.V. Chernikov *et al.*, "1083 nm ytterbium doped fibre amplifier for optical pumping of helium", *Electron. Lett.*, Vol. 33, pp.787-789, (1997)
- [61] A. Selfert *et al.*, "Narrow-linewidth, multi-Watt Yb-doped fiber amplifier at 1014.8nm", *Appl. Opt.*, Vol. 45, No. 30, pp. 7908-7911, (2006)

- [62] A.S. Kurkov *et al.*, "Multimode fiber lasers based on Bragg gratings and double-clad Yb-doped fibers", *Laser Phys. Lett.*, Vol. 1, No. 9, pp.473-375, (2004)
- [63] P. Dupriez, *et al.*, "High-power, high repetition rate picosecond and femtosecond sources based on Yb-doped fiber amplification of VECSELS", *Opt. Express*, Vol. 14, No. 21, pp.9611-9616, (2006)
- [64] M. E. Fermann, *et al.*, "Self-similar propagation and amplification of parabolic pulses in optical fibers", *Phys. Rev. Lett.*, Vol. 84, pp.6010, (2000).
- [65] C. Finot, *et al.*, "Parabolic pulse evolution in normally dispersive fiber amplifiers preceding the similariton formation regime", *Opt. Express*, Vol. 14, No. 8, pp.3161-3170, (2006)
- [66] M.J. Potasek and G.P.Agrawal, "Self-amplitude-modulation of optical pulses in nonlinear dispersive fibers", *Phys. Rev. A*, Vol. 36, No. 8, pp. 3862-3868, (1987)
- [67] Y. Wang, "Dynamics of Stimulated Raman Scattering in Double-Clad Fiber Pulse Amplifiers", *IEEE J. Quant. Electron.* Vol. 41, No. 6, pp.779-788, (2005)
- [68] N. G. Usechak *et al.*, "Tunable, high-repetition-rate, harmonically mode-locked ytterbium fiber laser", *Opt. Lett.* Vol. 29, No. 12, pp.1360-1362, (2004)
- [69] S. Sanders *et al.*, "Passive mode locking of a two-section multiple quantum well laser at harmonics of the cavity round-trip frequency", *Appl. Phys. Lett.*, Vol. 58, No. 7, pp.681-683, (1990)
- [70] J. Limpert *et al.*, "SPM-induced spectral compression of picosecond pulses in a single-mode Yb-doped fiber amplifier", *Appl. Phys. B*, Vol. 75, pp.191-195, (2002)
- [71] S. Grot *et al.*, "High power Yb³⁺-doped double clad fibre amplification at 1127 nm: 977 against 920 nm pumping comparison", *Electron. Lett.*, Vol. 39, No. 21, (2003)

- [72] D. J. Derickson *et al.*, "Short Pulse Generation Using Multisegment Mode-Locked Semiconductor Lasers", *IEEE J. Quant. Electron.*, Vol. **28**, No. 10, pp.2186-2202, (1992)
- [73] C. Barnard *et al.*, "Analytical Model for Rare-Earth-Doped Fiber Amplifiers and Lasers", *IEEE J. Quant. Electron.*, Vol. **30**, No. 8, pp.1817-1830, (1994)
- [74] Y. Wang, "Optimization of Pulse Amplification in Ytterbium-Doped Double-Clad Fiber Amplifiers", *J. Lightwave Technol.*, Vol. **23**, No. 6, pp.2139-2147, (2005)
- [75] H. Coïc, "Analytic modeling of high-gain ytterbium-doped fibre amplifiers", *J. Opt. A: Pure Appl. Opt.*, Vol. **4**, pp.120-129, (2002)
- [76] G. P. Agrawal, "Optical pulse propagation in doped fiber amplifiers", *Phys. Rev. A.*, Vol. **44**, No. 11, pp.7493-7501, (1991)
- [77] H. Amman *et al.*, "Theoretical investigation of short pulse amplification near 1.3 μm in a high gain Pr^{3+} -doped fluoride fiber", *Opt. Commun.*, Vol. **115**, pp.347-353, (1995)
- [78] R. Trebino *et al.*, "Measuring ultrafast laser pulses in the time-frequency domain using frequency-resolved optical gating", *Rev. Sci. Instrum.*, Vol. **68**, pp.3277, (1997)
- [79] C. Kittel, "Introduction to Solid State Physics", John Wiley & Sons, Inc., (2005)
- [80] R. I. Laming, "Pump excited-state absorption in erbium-doped fibers", *Opt. Lett.*, Vol. **13**, No. 12, pp.1084-1086, (1988)
- [81] C. Xiao-Bo and S. Zeng-Fu, "Excited-State Upconversion of $\text{Pr}(0.5)\text{Yb}(1.5):\text{ZBLAN}$ under Two-Colour Excitation", *Chin. Phys. Lett.*, Vol. **22**, No. 4, pp. 963-966, (2005)

- [82] F. L. Pedrotti and L. S. Pedrotti, "Introduction To Optics", Prentice Hall, Inc., (1987)
- [83] K. Kim *et al.*, "1.4 kW high peak power generation from an all semiconductor mode-locked master oscillator power amplifier system based on eXtreme Chirped Pulse Amplification (X-CPA)", *Opt. Express*, Vol. **13**, No. 12, pp.4600-4606, (2005)
- [84] P. Liu, *et al.*, "Picosecond Pulse Generation from InGaAsP Lasers at 1.25 and 1.3 μm by Electrical Pulse Pumping", *IEEE J. Quant. Electron.*, Vol. **QE-17**, No. 5, pp.671-674, (1981)
- [85] M.E. Fermann, *et al.*, "Ultrawide tunable Er soliton fiber laser amplified in Yb-doped fiber", *Opt. Lett.*, Vol. **24**, No. 20, pp.1428-1430, (1999)
- [86] G. Keiser, "Optical Fiber Communications", McGraw-Hill Companies, Inc., (2000)

Appendix A. Calculation of FWHM and RMS

Physicists use the root-mean-square (RMS) notation to measure the $1/e$ half-width of the pulse regardless of its shape. This type of measurement is very useful because the calculation is numerically straightforward to achieve:

$$\sigma = \sqrt{\langle \tau^2 \rangle - \langle \tau \rangle^2} \quad \text{A - 1}$$

$$\langle \tau^p \rangle = \frac{\int_{-\infty}^{\infty} \tau^p |A(z, \tau)|^2 d\tau}{\int_{-\infty}^{\infty} |A(z, \tau)|^2 d\tau} \quad \text{A - 2}$$

Clearly, the RMS width σ is a function of the energy of the signal. It is completely independent of the instantaneous pulse power distribution. Also, when calculating the RMS width of special functions such as a Gaussian or hyperbolic secant squared (sech^2), one can convert from RMS to the full-width at half max (FWHM) for those pulses. Engineers use FWHM to characterize the pulse in question. It is however not as useful because its value only makes sense if a bell-shaped pulse is being measured. If the pulse shape is arbitrary such as that illustrated in Figure A-1, the FWHM doesn't make as much sense as the RMS width - a factor of the energy of the signal.

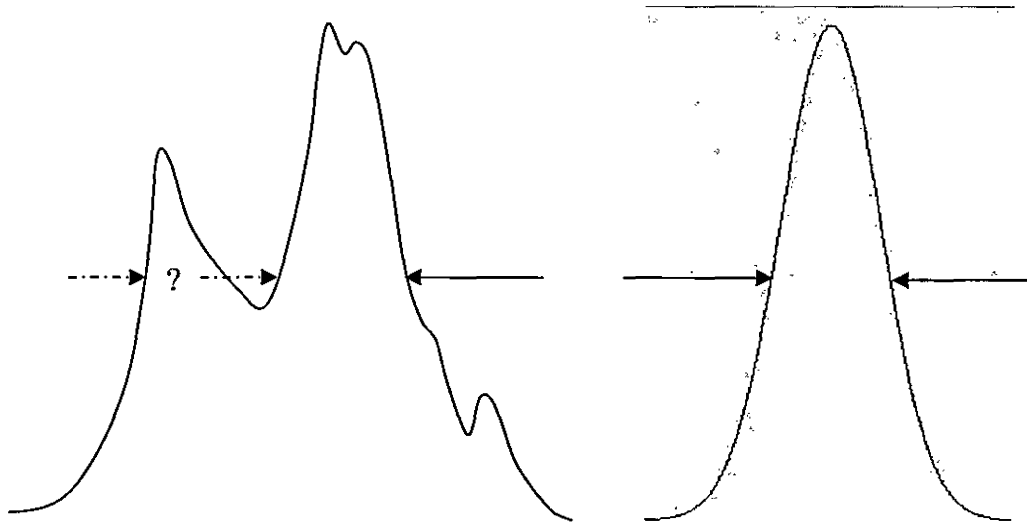


Figure A - 1 Calculation of FWHM for an arbitrary pulse (left) compared to a bell-shaped pulse (right). For arbitrary pulses, the definition of FWHM is not as descriptive as the RMS.

The calculation of RMS is straight forward by replacing the continuous integrals in equation A-1 and A-2 to discretized summations. The two width formats for a pure Gaussian have an analytical relationship, and this will now be proven. Note that the RMS width is measured for the power, *not* for the amplitude.

The pulse power P is defined according to some amplitude A that is a purely Gaussian distributed function.

$$P(\tau) = |A(\tau)|^2 = \left[A_0 \exp\left(-\frac{\tau^2}{2T_0^2}\right) \right]^2 = P_0 \exp\left(-\frac{\tau^2}{T_0^2}\right)$$

We seek the time at which the power is lowered to an intensity of P_0/e :

$$\exp\left(-\frac{\sigma^2}{T_0^2}\right) = \frac{1}{e} \rightarrow \sigma = T_0$$

Next we perform the same calculations for an intensity of $P_0/2$:

$$\exp\left(-\frac{\left(\frac{\tau_{FWHM}}{2}\right)^2}{T_0^2}\right) = \frac{1}{2} \rightarrow \tau_{FWHM} = 1.6651 \times T_0$$

Remember that the RMS is a measure of half-width, while the FWHM is measured for the full width of the pulse. Their relationship is given by the following:

$$\tau_{FWHM} = 1.6651 \times \sigma$$

A - 3

Appendix B. SSFM Dispersion Operator

The FFT is an algorithmically optimized discrete Fourier transform (DFT). And therefore, whatever properties the DFT has, so will the FFT. In particular, the following differentiation property [7] is used in the SSFM algorithm:

$$\frac{\partial^n}{\partial \tau^n} f(\tau) \xrightarrow{\text{FFT}} (iK)^n F[K] \quad \text{B - 1}$$

Here $n = 1, 2, \dots$ and $f(\tau)$ can represent any function. The partial differentiation is used because in our case, the operation is made on the amplitude function $A(z, \tau)$ which is a function of two variables. Recall the dispersion operation on the amplitude function from Equation 3-18:

$$\exp\left(\frac{\hbar}{2} \hat{D}\right) A(z, \tau) \quad \text{B - 2}$$

The exponential function can therefore be Taylor expanded and go through FFT as follows:

$$\begin{aligned} \exp\left(-ia \frac{\partial^2}{\partial \tau^2}\right) f(\tau) &= \left[1 + (-ia) \frac{\partial^2}{\partial \tau^2} + \frac{(-ia)^2}{2!} \left[\frac{\partial^2}{\partial \tau^2} \right]^2 + \dots \right] f(\tau) \\ &\xrightarrow{\text{FFT}} \left[1 + (-ia)[iK]^2 + \frac{(-ia)^2}{2!} [iK]^4 + \dots \right] F[K] \\ &= \exp(iaK^2) F[K] \end{aligned}$$

And therefore, the dispersion operation can be done as follows in the frequency domain

where $a = \frac{\beta_0''}{2} \frac{dz}{2}$:

$$\begin{aligned} \exp\left(\frac{\hbar}{2} \hat{D}\right) A(z, \tau) &= \exp\left(-ia \frac{\partial^2}{\partial \tau^2}\right) A(z, \tau) \\ &= \text{IFFT}\left(\exp(iaK^2) \text{FFT}(A(z, \tau))\right) \end{aligned} \quad \text{B-3}$$

In the above equation, the inverse fast Fourier transform (*IFFT*) is used to transform the easier calculation in the frequency domain back to the time domain. The final result in Equation B-3 above is then operated further as discussed for the SSFM algorithm in chapter 2.

Appendix C. Generalized Overlap Functions

The following is an analytical derivation of the power-dependent overlap integrals used in the power propagation and rate equations under the condition of simulation convergence or steady state. Unless stated otherwise, the approach as well as some notation for the following generalized derivation of the overlap functions is adapted from Giles and Desurvire [17]. The overlap equation of the optical mode in the k^{th} wavelength bin and the dopant concentration in the first and second energy level is defined formally:

$$\Gamma_{k,1} = \frac{1}{\bar{n}_1} \int_0^{2\pi b} \int_0^b i_k(r, \phi) n_1(r, \phi, z) r dr d\phi \quad \text{C - 1}$$

$$\Gamma_{k,2} = \frac{1}{\bar{n}_2} \int_0^{2\pi b} \int_0^b i_k(r, \phi) n_2(r, \phi, z) r dr d\phi \quad \text{C - 2}$$

For simplicity, the optical mode distribution is approximated to a Gaussian function:

$i_k(r, \phi) = (1/\pi w_k^2) \exp(-r^2/w_k^2)$, b is the effective core radius such that the effective area

$A_{\text{eff}} = \pi b^2 [m^2]$. The dopant population density in the energy level i and its average

n_i and \bar{n}_i , respectively, are related by the following equation:

$$\bar{n}_i = \frac{\int_0^b \int_0^{2\pi} n_i(r, \phi, z) r dr d\phi}{\pi b^2} \quad \text{C - 3}$$

For a YDFA, there are two energy levels to consider, and to find the steady state of the energy population densities $[1/m^3]$, one can start by setting the differentiation in the rate equation for the upper energy level to zero which results in a useful expression for n_2 :

$$\begin{aligned} \frac{dn_2}{dt} &= \sum_k \frac{P_k i_k \sigma_{a,k}}{h\nu_k} n_1(r, \phi, z) - \sum_k \frac{P_k i_k \sigma_{e,k}}{h\nu_k} n_2(r, \phi, z) - \frac{n_2(r, \phi, z)}{\tau} \\ &= 0 \text{ in steady state} \end{aligned}$$

$$\therefore n_2(r, \phi, z) = n_2 = n_1 \frac{\sum_k \frac{\tau \sigma_{a,k}}{h\nu_k} P_k i_k}{1 + \sum_k \tau \frac{(\sigma_{a,k} + \sigma_{e,k})}{h\nu_k} P_k i_k} \quad \text{C - 4}$$

The total power in the k^{th} wavelength bin distributed radially by the function i_k is defined as $P(r, \phi, z, \lambda_k) = P_k(z) i_k(r, \phi) = (P_k / \pi w_k^2) \exp(-r^2 / w_k^2)$ (with a similar approach taken by Eichhorn [8]). $\sigma_{a,k}$ and $\sigma_{e,k}$ are the absorption and emission cross-sections respectively and conservation of dopant energy density is maintained by $n_t = n_1 + n_2$ which can then be used with Equation F-4 to derive:

$$n_1 = n_t \left(\frac{1 + \sum_k \tau \frac{\sigma_{e,k} P_k i_k}{h\nu_k}}{1 + \sum_k \tau \frac{(\sigma_{a,k} + \sigma_{e,k}) P_k i_k}{h\nu_k}} \right) \quad \text{C-5}$$

First, some encompassing variables are introduced for ease of calculation:

$$P_{ke} = \tau \frac{\sigma_{e,k} P_k}{h\nu_k \pi w_k^2} \quad P_{ka} = \tau \frac{\sigma_{a,k} P_k}{h\nu_k \pi w_k^2}$$

$$\beta_k = P_{ke} \quad \alpha_k = P_{ke} + P_{ka}$$

$$\delta_k = P_{ka}$$

$$\therefore \bar{n}_1 = \frac{\int_0^{2\pi} \int_0^b n_t \left(\frac{1 + \sum_k \beta_k e^{(-r^2/w_k^2)}}{1 + \sum_k \alpha_k e^{(-r^2/w_k^2)}} \right) r dr d\phi}{\pi b^2} \quad \text{and} \quad \bar{n}_2 = \frac{\int_0^{2\pi} \int_0^b n_t \left(\frac{\sum_k \delta_k e^{(-r^2/w_k^2)}}{1 + \sum_k \alpha_k e^{(-r^2/w_k^2)}} \right) r dr d\phi}{\pi b^2}$$

The expressions calculate the average due to optical beams from all wavelength bins. An assumption is made by Giles and Desurvire [17] that the dynamic effects on the energy population densities by individual monochromatic components of the pulse (i.e. each optical beam) are mutually exclusive. Whether or not this assumption is a valid one must be left to experimental verification. The calculation for the average dopant population density in the first and second energy levels results in:

\bar{n}_1	\bar{n}_2
$\frac{\int_0^{2\pi} \int_0^b n_i \left(\frac{1}{1 + \alpha e^{(-r^2/w^2)}} + \frac{\beta e^{(-r^2/w^2)}}{1 + \alpha e^{(-r^2/w^2)}} \right) r dr d\phi}{\pi b^2}$ $= \frac{2n_i w^2}{b^2} \left\{ \int_0^{b^2/w^2} \frac{0.5}{1 + \alpha e^{-x}} dx + \int_0^{b/w} \frac{\beta u e^{-u^2}}{1 + \alpha e^{-u^2}} du \right\}$ $= \frac{n_i w^2}{b^2} \left\{ \frac{b^2}{w^2} + \ln \left(\frac{\alpha e^{-b^2/w^2} + 1}{\alpha + 1} \right) \right\}$ $\left\{ -\frac{\beta}{\alpha} \ln \left(\frac{\alpha e^{-b^2/w^2} + 1}{\alpha + 1} \right) \right\}$	$\frac{\int_0^{2\pi} \int_0^b n_i \frac{\delta e^{(-r^2/w^2)}}{1 + \alpha e^{(-r^2/w^2)}} r dr d\phi}{\pi b^2}$ $= \frac{2n_i w^2 \delta}{b^2} \int_0^{b/w} \frac{u e^{-u^2}}{1 + \alpha e^{-u^2}} du$ $= \frac{n_i w^2}{b^2} \left(-\frac{\delta}{\alpha} \right) \ln \left(\frac{\alpha e^{-b^2/w^2} + 1}{\alpha + 1} \right)$

$$\bar{n}_1 = n_i \left[1 + \left(1 - \frac{\beta}{\alpha} \right) \frac{w^2}{b^2} \ln \left(\frac{\alpha e^{-b^2/w^2} + 1}{\alpha + 1} \right) \right] \quad \text{C-6}$$

$$\bar{n}_2 = n_i \left[-\frac{\delta}{\alpha} \frac{w^2}{b^2} \ln \left(\frac{\alpha e^{-b^2/w^2} + 1}{\alpha + 1} \right) \right] \quad \text{C-7}$$

Next, the overlap function defined in Equation F-1 must be solved analytically. Substituting the approximated value of n_i where $i \in 1, 2$, the calculations are solved as follows:

$\Gamma_{k,1}$	$\Gamma_{k,2}$
$\frac{n_t}{\bar{n}_1} \int_0^b \int_0^{2\pi} \frac{e^{-r^2/w^2}}{\pi w^2} \left(\frac{1}{1 + \alpha e^{(-r^2/w^2)}} + \frac{\beta e^{(-r^2/w^2)}}{1 + \alpha e^{(-r^2/w^2)}} \right) r dr d\phi$ $= \frac{2n_t}{\bar{n}_1} \left\{ \int_0^{b/w} \frac{ue^{-u^2}}{1 + \alpha e^{(-u^2)}} du + \frac{\beta}{\alpha^2} \int_0^{b/w} \frac{u}{1 + \alpha e^{(-u^2)}} - u(1 - \alpha e^{(-u^2)}) du \right\}$ $= \frac{2n_t}{\bar{n}_1} \left\{ \left[\left(\frac{-1}{2\alpha} \right) \ln(1 + \alpha e^{-u^2}) \right]_0^{b/w} + \frac{\beta}{2\alpha^2} [x + \ln(1 + \alpha e^{-x})]_0^{b^2/w^2} - \frac{\beta}{\alpha^2} \left(\left[\frac{u^2}{2} \right]_0^{b/w} + \frac{\alpha}{2} [e^{-x}]_0^{b^2/w^2} \right) \right\}$	$\frac{n_t}{\bar{n}_2} \int_0^b \int_0^{2\pi} \frac{e^{-r^2/w^2}}{\pi w^2} \left(\frac{\delta e^{(-r^2/w^2)}}{1 + \alpha e^{(-r^2/w^2)}} \right) r dr d\phi$ $= \frac{2\delta n_t}{\bar{n}_2} \int_0^{b/w} \frac{ue^{-2u^2}}{1 + \alpha e^{-u^2}} du$ $= \frac{2\delta n_t}{\alpha^2 \bar{n}_2} \int_0^{b/w} \frac{u}{1 + \alpha e^{(-u^2)}} - u(1 - \alpha e^{(-u^2)}) du$ $= \frac{2n_t}{\bar{n}_2} \left[\frac{\delta}{2\alpha^2} [x + \ln(1 + \alpha e^{-x})]_0^{b^2/w^2} - \frac{\delta}{\alpha^2} \left(\left[\frac{u^2}{2} \right]_0^{b/w} + \frac{\alpha}{2} [e^{-x}]_0^{b^2/w^2} \right) \right]$

$$\Gamma_{k,1} = \frac{\left\{ \left(\frac{\beta}{\alpha} - 1 \right) \ln \left(\frac{\alpha e^{-b^2/w^2} + 1}{\alpha + 1} \right) + \beta (1 - e^{-b^2/w^2}) \right\}}{\alpha \left[1 + \left(1 - \frac{\beta}{\alpha} \right) \frac{w^2}{b^2} \ln \left(\frac{\alpha e^{-b^2/w^2} + 1}{\alpha + 1} \right) \right]} \quad \text{C-8}$$

$$\Gamma_{k,2} = \frac{\left\{ -\ln \left(\frac{\alpha e^{-b^2/w^2} + 1}{\alpha + 1} \right) + \alpha [e^{-b^2/w^2} - 1] \right\}}{\alpha \left[\frac{w^2}{b^2} \ln \left(\frac{\alpha e^{-b^2/w^2} + 1}{\alpha + 1} \right) \right]} \quad \text{C-9}$$

If we set $\beta = 0$ in Equation F-8 or in other words set the emission cross-section $\sigma_{e,k}$ to zero, then the resulting simplification is identical to the result by Giles and Desurvire [17]:

$$\Gamma_{k,1} = \frac{-\ln\left(\frac{1 + \alpha e^{-b^2/w^2}}{1 + \alpha}\right)}{\alpha \left\{ 1 + \frac{w^2}{b^2} \ln\left(\frac{\alpha e^{-b^2/w^2} + 1}{\alpha + 1}\right) \right\}} \quad \text{C - 10}$$

Finally, by setting $\alpha = \beta = 0$, the first energy level overlap function becomes the *total* overlap function:

$$\begin{aligned} \lim_{\alpha \rightarrow 0} \Gamma_{k,1} &= \Gamma_k \\ &= 1 - e^{-b^2/w^2} \end{aligned} \quad \text{C - 11}$$

This result is very similar to the overlap equation used by Eichhorn [8], where the difference arises in the total overlap function result due to a choice of slightly different Gaussian distribution approximations. Two possible total overlap functions are provided in Table F-1.

Table C - 1 Two valid modal distributions for the approximation of interaction of light and matter in the fiber.

Author	Eichhorn [8]	Giles and Desurvire [17]
Distribution Approximation $i_k(r, \phi)$	$(2/\pi w_k^2) \exp(-2r^2/w_k^2)$	$(1/\pi w_k^2) \exp(-r^2/w_k^2)$
Total Overlap Function Γ_k	$1 - e^{-2b^2/w^2}$	$1 - e^{-b^2/w^2}$

The validity of a distribution is dependent on how close one wants to approximate the Bessel modal distributions discussed in chapter 2. Also, it must satisfy Equation 3-3 which has been re-written below in the mathematical context of this appendix:

$$\begin{aligned} P_k(z) &= \int_0^{2\pi\infty} \int_0^\infty I_k(r, \phi, z) r dr d\phi \\ &= \int_0^{2\pi\infty} \int_0^\infty P_k(z) i_k(r, \phi) r dr d\phi \end{aligned}$$

C - 12

Both distributions provided in Table F-1 satisfy Equation F-10 and the total overlap functions (also provided in the table) are typically used instead of the frequency and energy population level dependent versions (equations C-1 and C-2) to save computation time.

Appendix D. Simulation Input Tables

Table 6-2 Parameters used for comparison of the MCP and Morasse's simulators operating in the cw regime. No Fresnel's losses have been taken into account here, as they have also been set to zero by Morasse in his simulation.

Operating Parameter	Value	Description
λ_s	1075.0 nm	cw Peak (Operating) wavelength
λ_p	976.0 nm	cw Pump Wavelength
P_{avg}	0.001 W	Average Seed Power
P_p	4.0 W	Average Pump Power
L	1,2,...,10 m	Fiber Length
n_{SiO_2}	1.45	Silica (Background) Index of Refraction
$NSTEPS$	501	Fiber discretization (length divided by $NSTEPS - 1$)
σ_a	Figure 3.6 [m ²]	Absorption Cross-Section
σ_e	Figure 3.6 [m ²]	Emission Cross-Section
a	3.0 μ m	Core Radius
A_p	1.35×10^{-8} m ²	Inner-Cladding area (for the pump overlap function)
NA	0.13	Core numerical aperture
N_0	1.0×10^{26} m ⁻³	Dopant Concentration
τ	0.8 ms	Radiative relaxation time constant
α_s, α_p	0.0046 m ⁻¹	Background Signal & Pump loss respectively

Table 6-3 Parameters used for comparison of the MCP and Eichhorn's pulsed simulations in modeling pulsed operation of Tm:ZBLAN double clad fiber amplifiers with a D-shaped inner cladding. Note that the signal overlap function Γ_j from Equation 3-6 is generated dynamically on software initialization. Radiative and non-radiative time-constants are provided in Chapter 3.

Operating Parameter	Value	Description
PBC	2.5	Pulse Boundary Coefficient (Defined in section 3.2.2)
FWHM	30.0 ns	Full Width at Half Maximum
λ_s	1870 nm	Pulse Peak (Operating) wavelength
λ_p	800 nm	cw Pump Wavelength
$\sigma_{a,p}$	$1.96 \times 10^{-25} \text{ m}^2$	Absorption Cross-Section at the Pump Wavelength
$\sigma_{e,p}$	$4.83 \times 10^{-25} \text{ m}^2$	Emission Cross-Section at the Pump Wavelength
P_0	4.0 W	Seed (Gaussian) Pulse Peak Power
$P_{avg,ASE}$	0.5 mW	Seed Average ASE Power
P_p	3.0 W	Average Pump Power
L	1.0,1.2,1.5,1.7 2.0,2.2,2.5 m	Fiber Length
n_{ZBLAN}	1.49	ZBLAN (Background) Index of Refraction
$NSTEPS$	200	Fiber discretization (length divided by $NSTEPS - 1$)
ν_{rep}	60 kHz	Repetition Rate
σ_a	Figure 3.5 [m^2]	Absorption Cross-Section
σ_e	Figure 3.5 [m^2]	Emission Cross-Section
a	7.5 μm	Core Radius
A_p	$1.079 \times 10^{-8} \text{ m}^2$	D-Shaped Inner-Cladding area
D	0.016	Pump Overlap Function $\pi a^2 / A_p$
NA	0.12	Core numerical aperture
N_0	$4.69 \times 10^{26} \text{ m}^{-3}$	Dopant Concentration
k_{3011}	$7.86 \times 10^{-24} \text{ m}^3/\text{s}$	Cross-Relaxation
k_{1130}	$6.00 \times 10^{-25} \text{ m}^3/\text{s}$	Cross-Relaxation
M	12	Number of spatial modes
PA	12.0 degrees	Fiber facet polishing angle
α_s	0.0 m^{-1}	(Negligible) Background Signal loss
α_p	0.0 m^{-1}	(Negligible) Background Pump loss

Table 6-4 Parameters used for MCP pulsed simulation 20 kHz rep-rate for a co-propagating geometry. The signal overlap functions Γ_j from Equation 3-6 are generated on software initialization.

Operating Parameter	Value	Description
PBC	2.5	Pulse Boundary Coefficient (Defined in section 3.2.2)
FWHM	100.0 ns	Full Width at Half Maximum
λ_s	1064.0 nm	Pulse Peak (Operating) wavelength
λ_p	915 nm	cw Pump Wavelength
$\sigma_{a,p}$	$7.45 \times 10^{-25} \text{ m}^2$	Absorption Cross-Section at the Pump Wavelength
$\sigma_{e,p}$	$2.47 \times 10^{-26} \text{ m}^2$	Emission Cross-Section at the Pump Wavelength
P_0	75.0 W	Seed (Gaussian) Pulse Peak Power
P_p	3.0, 7.0 and 11.0 W	Average Pump Power
L	10.0 m	Fiber Length
n_{SiO_2}	1.45	Silica (Background) Index of Refraction
<i>NSTEPS</i>	501	Fiber discretization (length divided by <i>NSTEPS</i> - 1)
ν_{rep}	20 kHz	Repetition Rate
σ_a	Figure 3.6 [m^2]	Absorption Cross-Section
σ_e	Figure 3.6 [m^2]	Emission Cross-Section
a	5 μm	Core Radius
A_p	$1.33 \times 10^{-8} \text{ m}^2$	Hexagonal Inner-Cladding area
D	0.0059	Pump Overlap Function $\pi a^2 / A_p$
<i>NA</i>	0.12	Core numerical aperture
N_0	$1.0 \times 10^{26} \text{ m}^{-3}$	Dopant Concentration
τ	0.8 ms	Radiative relaxation time constant
M	1	Number of modes
<i>PA</i>	8.0 degrees	Fiber facet polishing angle
α_s	0.00023 m^{-1}	(Negligible) Background Signal loss
α_p	0.00023 m^{-1}	(Negligible) Background Pump loss

Table 6-5 Parameters used for the MCP simulator for modeling a 10 kHz repetition rate pulsed operation in the co-propagating geometry for comparison to Wang's work [32]

Operating Parameter	Value	Description
PBC	2.5	Pulse Boundary Coefficient (Defined in section 3.2.2)
FWHM	20.0 ns	Full Width at Half Maximum
λ_s	1064.0 nm	Pulse Peak (Operating) wavelength
λ_p	915.0 nm	cw Pump Wavelength
$\sigma_{a,p}$	$7.45 \times 10^{-25} \text{ m}^2$	Absorption Cross-Section at the Pump Wavelength (<i>not taken as $8.0 \times 10^{-25} \text{ m}^2$ from [32]</i>)
$\sigma_{e,p}$	$2.47 \times 10^{-26} \text{ m}^2$	Emission Cross-Section at the Pump Wavelength (<i>not taken as $5.0 \times 10^{-26} \text{ m}^2$ from [32]</i>)
P_0	47 W	Seed (Gaussian) Pulse Peak Power
$P_{avg,ASE}$	0.0 mW	Seed Average ASE Power
P_p	20 W	Average Pump Power
L	10.0 m	Fiber Length
n_{SiO_2}	1.45	Silica (Background) Index of Refraction
N_{STEPS}	500	Fiber discretization (length divided by $N_{STEPS} - 1$)
ν_{rep}	10.0 kHz	Repetition Rate
σ_a	Figure 3.5 [m^2]	Absorption Cross-Section (<i>not taken from [42]</i>)
σ_e	Figure 3.5 [m^2]	Emission Cross-Section (<i>not taken from [42]</i>)
a	9.77 μm	Core Radius
A_p	$3.0 \times 10^{-8} \text{ m}^2$	Assuming Circular Shaped Inner-Cladding area
D	0.01	Pump Overlap Function
Γ	Equation 3-6	Signal Overlap Function (<i>not taken as 0.85 from [32]</i>)
NA	0.046	Core numerical aperture
N_0	$6.0 \times 10^{25} \text{ m}^{-3}$	Dopant Concentration
τ	0.84 ms	Radiative relaxation time constant
M	1.0	Number of modes
α_s	0.003 m^{-1}	(Negligible) Background Signal loss
α_p	0.003 m^{-1}	(Negligible) Background Pump loss
No. pulses	1,2,3,...,10	Number of consecutive pulses
α_{RS}	0	Rayleigh Scattering Coefficient (<i>not implemented</i>)

4146 48

R



Table 6-6 Parameters used for the MCP simulator in modeling 577 MHz pulsed operation in the counter-propagating geometry.

Operating Parameter	Value	Description
PBC	2.5	Pulse Boundary Coefficient (Defined in section 3.2.2)
FWHM	7.7 ps	Full Width at Half Maximum
λ_s	1075.0 nm	Pulse Peak (Operating) wavelength
λ_p	975.0 nm	cw Pump Wavelength
$\sigma_{a,p}$	$2.64 \times 10^{-24} \text{ m}^2$	Absorption Cross-Section at the Pump Wavelength
$\sigma_{e,p}$	$2.38 \times 10^{-24} \text{ m}^2$	Emission Cross-Section at the Pump Wavelength
P_0	0.043 W	Seed (Gaussian) Pulse Peak Power
$P_{avg,ASE}$	0.0 mW	Seed Average ASE Power
P_p	2.11 W	Average Pump Power
L	14.8 m	Fiber Length
n_{SiO_2}	1.45	Silica (Background) Index of Refraction
<i>NSTEPS</i>	500	Fiber discretization (length divided by <i>NSTEPS</i> - 1)
ν_{rep}	577.0 MHz	Repetition Rate
σ_a	Figure 3.5 [m^2]	Absorption Cross-Section
σ_e	Figure 3.5 [m^2]	Emission Cross-Section
a	3.0 μm	Core Radius
A_p	$1.46 \times 10^{-8} \text{ m}^2$	Hexagonal-Shaped Inner-Cladding area
D	0.0019	Pump Overlap Function $\pi a^2 / A_p$
NA	0.13	Core numerical aperture
N_0	$1.0 \times 10^{26} \text{ m}^{-3}$	Dopant Concentration
τ	1.5 ms	Radiative relaxation time constant
M	1.0	Number of spatial modes
PA	8.0 degrees	Fiber facet polishing angle
α_s	$2.30 \times 10^{-4} \text{ m}^{-1}$	(Negligible) Background Signal loss
α_p	$2.30 \times 10^{-4} \text{ m}^{-1}$	(Negligible) Background Pump loss
A_{eff}	$39.12 \times 10^{-12} \text{ m}^2$	Effective Area (πw_s^2)
β_2	$15.0 \times 10^{-27} \text{ s}^2/\text{m}$	GVD parameter
n_2	$2.2 \times 10^{-20} \text{ m}^2/\text{W}$	SPM parameter
No. pulses	260,000	Number of consecutive pulses